Mirror pulses and position reconstruction in segmented HPGe detectors

Diplomarbeit der Fakultät für Physik
der
Ludwig-Maximilians-Universität München

vorgelegt von
Sabine Hemmer,
geboren am 27. Dezember 1984 in München

München, den 17. September 2010

Erstgutachter: Prof. Dr. Christian Kiesling
Zweitgutachterin: Prof. Dr. Dorothee Schaile

Nur wenige wissen, wie viel man wissen muss,
um zu wissen, wie wenig man weiß.

Werner Heisenberg

Abstract

Segmented germanium detectors are developed for applications in various fields of physics research. In experiments designed to search for neutrinoless double beta decay, like the GERDA experiment, they can be used to reduce the background level. In this context, position reconstruction of energy depositions can help to identify background sources.
A phenomenon intrinsic to segmented detectors are mirror pulses. Their characteristics depend on the position of the energy deposition. Simulated mirror pulses were used to define parameters that quantify this dependence for single energy depositions. A method to reconstruct the radial and azimuthal position of single energy depositions was developed. The resolution achieved was $\mathcal{O}$(mm).
Data was recorded with an 18–fold segmented high-purity n-type germanium detector. The detector was characterized. Double escape peak events from the 2.6 MeV line of ^{208}Tl were used to verify the simulation of the mirror pulses and to test the method to reconstruct the position of single energy depositions. This was done by comparing distributions of the mirror charge parameters and the reconstructed positions for simulation and data.

Zusammenfassung

Die Entwicklung von segmentierten Germaniumdetektoren ist für verschiedene Forschungsbereiche der Physik von Interesse. In Experimenten mit denen nach neutrinolosem Doppelbetazerfall gesucht wird, wie dem GERDA-Experiment, können sie zur Senkung des Untergrundniveaus eingesetzt werden. Die Positionsrekonstruktion von Energiedepositionen kann zusätzlich dabei helfen, Untergrundquellen zu identifizieren.
Ein Phänomen, das bei segmentierten Detektoren auftritt, sind Spiegelpulse. Ihre Eigenschaften hängen vom Ort der Energiedeposition ab. Simulierte Spiegelpulse wurden untersucht, um Parameter zu definieren, die diese Abhängigkeiten quantifizieren. Anschliessend wurde eine Methode entwickelt, mit deren Hilfe der Ort von einzelnen Energiedepositionen rekonstruiert werden kann. Die Auflösung der Rekonstruktion war $\mathcal{O}$(mm).
Mit einem 18–fach segmentierten hochreinen n-Typ Germaniumdetektor wurden Daten genommen. Der Detektor wurde charakterisiert. Anhand von Double-Escape-Peak Ereignissen aus der 2.6 MeV-Linie von ^{208}Tl wurde die Simulation der Spiegelpulse verifiziert und die Positionsrekonstruktionsmethode für einzelne Energiedepositionen an Daten getestet. Dazu wurden die Verteilungen der Parameter, die die Spiegelpulse beschreiben, und die der rekonstruierten Positionen für die Simulation und die Daten verglichen.

Contents

Chapter 1

Introduction

The subject of this thesis is the investigation of so called mirror charges, a phenomenon intrinsic to segmented germanium detectors, which are developed for a variety of applications in particle and nuclear physics [1, 2]. The context of this thesis is neutrino physics. In the introduction, the framework in which the work is to be seen is presented.

1.1 Neutrino nature and oscillations

The neutrino was postulated in 1930 by Pauli to conserve energy and momentum in nuclear beta decay. Since then it was assumed to be a charge- and massless Dirac particle. Already in 1938, it was pointed out that the neutrino could also be a Majorana particle, i.e. its own anti-particle. Due to it only weakly interacting, the neutrino was not observed directly until 1956. In the late 1960s, the *solar neutrino problem* was discovered, i.e. a deficit in the flux of electron neutrinos, ν_e, coming from the sun. This was later explained by neutrino oscillations, in which ν_e change their flavor to become muon neutrinos, ν_μ. Observations of the flux of atmospheric neutrinos suggest oscillations from ν_μ to tau neutrinos, ν_τ. Oscillations require that at least two types of neutrinos have finite masses. The flavor eigenstates, ν_α, $\alpha = e, \mu, \tau$, can then be described as combinations of mass eigenstates, ν_i, with

$$|\nu_\alpha\rangle = \sum_i U^*_{\alpha i} |\nu_i\rangle, \tag{1.1}$$

where U is a unitary matrix referred to as the Pontecorvo-Maki-Nakagawa-Sakata, *PMNS*, matrix. The time evolution of a neutrino created in the flavor eigenstate $|\nu_\alpha\rangle$ is calculated from the mass eigenstates it is composed of. A neutrino created in the state $|\nu_\alpha\rangle$ becomes a superposition of all flavors after having travelled a distance L:

$$|\nu_\alpha(L)\rangle = \sum_i U^*_{\alpha i} e^{-i(m_i^2/2E)L} |\nu_i\rangle, \tag{1.2}$$

where m_i is the mass of the i-th mass eigenstate and E is the average energy of all mass eigenstates. Inverting Equation (1.1) and inserting it into Equation (1.2) gives

$$|\nu_\alpha(L)\rangle = \sum_\beta \left[\sum_i U^*_{\alpha i} e^{-i(m_i^2/2E)L} U_{\beta i} \right] |\nu_\beta\rangle.$$

The probability to find the neutrino in a flavor state $|\nu_\beta\rangle$ after it traveled the distance L is [3]

$$|\langle \nu_\beta | \nu_\alpha(L)\rangle|^2 = \sum_i |U_{\beta i} U^*_{\alpha i}|^2 + 2Re \sum_{j>i} U_{\beta i} U^*_{\beta j} U^*_{\alpha i} U_{\alpha j} e^{(-i\Delta m^2_{ij}/2E)L}. \tag{1.3}$$

As can be seen in Equation 1.3, only differences in m_i^2, $\Delta m^2_{ij} = m_i^2 - m_j^2$, can be inferred from oscillation measurements. Therefore, the absolute neutrino mass scale is still unknown, eventhough the Δm^2_{ij} are quite well known [4]. Also the question if the neutrino is a Dirac or a Majorana particle has not been answered. The answer to this question could lead to more insight regarding the origin of the matter-antimatter asymmetry in the universe.

1.2 Neutrino mass scale

Three approaches to determine the neutrino mass scale are followed. A detailed review on the experimental status can be found in [5] and references therein.

An indirect determination is based on cosmology. The best limit comes from the density of large-scale structures. The large-scale structures existing today have evolved from small initial density fluctuations. Relativistic neutrinos have escaped from areas with high density, washing out the structures. The extent of this effect is determined by the neutrino masses. The results are model dependent, but an upper limit of the order of 1 eV was established for the sum of the neutrino masses, $\sum_{i=1}^{3} m_i \lessapprox 1\,\text{eV}$.

Direct mass measurements are possible in decays where one of the decay products is a neutrino. The effective electron neutrino mass can thus be deduced from beta-decay experiments by measuring the shape of the electron energy spectrum around the endpoint energy. The shape of the spectrum in this region depends on the mass of ν_e, $m_{\nu_e} = \sqrt{\sum_i |U_{ei}|^2 m_i^2}$, where the sum runs over all mass eigenstates and U_{ei} are the elements of the PMNS matrix. The best limit comes from the measurement of the endpoint energy in tritium decays. The Mainz experiment gives $m_{\nu_e} < 2.3\,\text{eV}$ (95% CL) [6] and the Troitsk experiment gives $m_{\nu_e} < 2.1\,\text{eV}$ (95% CL) [7].

The third class of experiments are those searching for *neutrinoless double beta decay*, $0\nu\beta\beta$. They are sensitive to the effective Majorana neutrino mass, m_M. The observation of $0\nu\beta\beta$ would be the proof that the neutrino has at least a Majorana component with a non-zero mass [8].

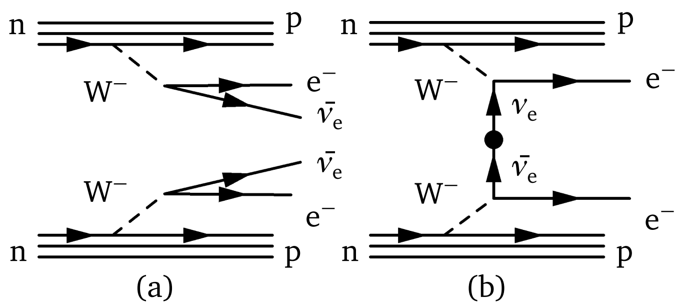

Figure 1.1: Feynman diagram of double beta decay (a) with and (b) without two anti-neutrinos being emitted.

1.3 Neutrinoless double-beta decay

Even-even nuclei are more bound than odd-odd nuclei due to the pairing interaction. Therefore, nuclei exist that cannot decay via single β-decay. They can, however, undergo double beta decay with emission of two electrons. If neutrinos are Dirac particles, two anti-neutrinos have to be emitted, resulting in neutrino-accompanied double beta decay, $2\nu\beta\beta$:

$$2\nu\beta\beta : (Z,A) \rightarrow (Z+2,A) + 2e^- + 2\bar{\nu}_e,$$

where Z is the atomic charge and A the mass number.

If neutrinos are Majorana particles, the anti-neutrino emitted in one beta decay can be absorbed in the other, leading to a decay without anti-neutrinos, $0\nu\beta\beta$.

$$0\nu\beta\beta : (Z,A) \rightarrow (Z+2,A) + 2e^-.$$

Since this process requires a helicity-flip, the neutrino has to be massive. The Feynman diagrams of both double beta decay processes are shown in Fig. 1.1.

From the half-life of $0\nu\beta\beta$, m_M can be deduced.

Several experiments have set limits on m_M. The CUORICINO collaboration [9] gave an upper limit between 0.19 and 0.68 eV (90% CL), depending on the nuclear model used in the analysis. This was achieved with 40.7 kg of TeO_2 bolometers, searching for $0\nu\beta\beta$ of ^{130}Te.

The IGEX collaboration [10] found an upper limit between 0.33 and 1.35 eV (90% CL) by emplyoing germanium detectors to search for $0\nu\beta\beta$ of ^{76}Ge. Another experiment searching for $0\nu\beta\beta$ of ^{76}Ge was the Heidelberg-Moscow, HdM, experiment [11]. The upper limit determined by this collaboration is between 0.32 and 1 eV (90% CL). A part of the HdM collaboration claims that $m_M = 0.2 \sim 0.6$ eV [12].

1.4 Experimental requirements to find $0\nu\beta\beta$

If it exists, $0\nu\beta\beta$ is an extremely rare process. If the number of signal events, N_s, is smaller than the standard fluctuation expected for the number of background events,

N_b, no signal can be extracted and only a limit on the half-life of $0\nu\beta\beta$ can be deduced. If $N_s > \sqrt{N_b}$, the sensitivity of an experiment scales as

$$\kappa \cdot \varepsilon \cdot \ln(2) \cdot \frac{N_A M t}{M_A \sqrt{N_b}} = \kappa \cdot \varepsilon \cdot \ln(2) \cdot \frac{N_A}{M_A} \sqrt{\frac{M t}{b \Delta E}},$$

where M_A and κ are the atomic mass and the abundance of the isotope under study, ε is the signal efficiency, N_A is Avogadro's number, M is the total source material mass in grams, ΔE is the energy region of interest, ROI, around the Q-value, which scales with the resolution of the detector, and b is the *background index*, $b = N_b/(M \cdot t \cdot \Delta E)$, given in counts/(kg · keV · y). If $N_b = 0$, the sensitivity scales linearly with the measuring time, t.

The sensitivity is good, if the following is true:

- ε is large;
- a good energy resolution allows for a small ΔE;
- b is small;
- t is long;
- $M \cdot \kappa$ is large.

1.5 Search for $0\nu\beta\beta$ of ^{76}Ge

Germanium detectors are an attractive option to search for $0\nu\beta\beta$. They have been used for decades to analyze nuclear decays via the detection of photons. The isotope ^{76}Ge is a candidate to decay via $0\nu\beta\beta$. Germanium detectors thus are source and detector, offering high ε.

The energy resolution is typically better than 0.3% around the Q-value of ^{76}Ge, which is 2039 keV, allowing for small ΔE and a good separation between the $0\nu\beta\beta$ signal and the $2\nu\beta\beta$ background.

The Q-value of ^{76}Ge is lower than several gamma lines from natural radioactivity that thus contribute to the background in the ROI. However, the good resolution and therefore small ΔE compensate for this.

In addition, germanium is produced extremely pure, allowing large detector volumes and a low intrinsic background rate. The largest germanium detectors have a cylindrical shape with heights and diameters of up to 10 cm, minimizing the surface-to-volume ratio.

Unfortunately, the κ of ^{76}Ge is only 7.8%. Since N_s scales with $\kappa \cdot M$ and N_b with M, the detector material has to be enriched, which adds extra costs.

1.6 GERDA

The GERmaniumDetectorArray, GERDA [2], is an experiment designed for the search of $0\nu\beta\beta$ of ^{76}Ge and is currently in the commissioning phase. The general idea is to operate germanium detectors directly submerged in cryoliquid to remove material from their surrounding. In the ROI, b is to be reduced by up to a factor 100 compared to previous $0\nu\beta\beta$ experiments such as IGEX and HdM. GERDA will be operated in two phases. In the first phase, enriched germanium detectors from the IGEX and HdM experiments are reused and b in the ROI targeted is of the order of 10^{-2} counts/(keV · kg · y). In this phase, it will be possible to test the claim made by a part of the HdM collaboration. In the second phase, additional detectors will be deployed and an improved b of 10^{-3} counts/(keV · kg · y) in the ROI will allow measurements of the Majorana neutrino mass down to a limit of $m_M \leq 0.09 - 0.29$ eV (90% CL), depending on the matrix element used.

The sensitivity of the GERDA experiment will be limited by b. The background is mainly produced by the radioactivity of the experiment environment, comprising the materials used to build the experiment. Another contribution comes from cosmic radiation. To avoid the latter, the experiment is located in the Gran Sasso underground laboratory, where the rock above the laboratory provides in average 3400 m of water equivalent shielding. In addition, an active shield tags remaining cosmic muons.

The environmental background component is reduced by a passive shield: The germanium detectors are submerged in a stainless-steel cryostat with a diameter of 4.2 m, filled with 70 m^3 of liquid argon. The cryostat is surrounded by a water tank with a diameter of 10 m and a height of 9 m, containing 590 m^3 of ultra-pure water. The water serves as shielding for photons and neutrons from outside the watertank.

All materials used to build the experiment were screened to guarantee their radio-purity. Bare germanium detectors are operated directly submerged in ultra-pure liquid argon, which serves also as cooling medium. The materials of the support structure are copper and teflon. Both materials can be produced with high radio purity.

On top of the water tank, a class 10 000 clean room is located, where the detectors are stored in a dedicated storage system. The handling of the detectors takes place in class 100 flow-boxes. The detector strings are inserted into the cryoliquid through a lock system. The detector array consists of up to 16 detector strings.

An engineer's view of the GERDA experiment is shown in Fig. 1.2.

1.7 Background rejection

The background rate in the ROI is crucial for the success of GERDA. The careful construction of GERDA, as described in the previous section, results in a low level of radioactivity. However, this is not enough to reach a small enough b. For this reason, several techniques have been developed to reject remaining background events.

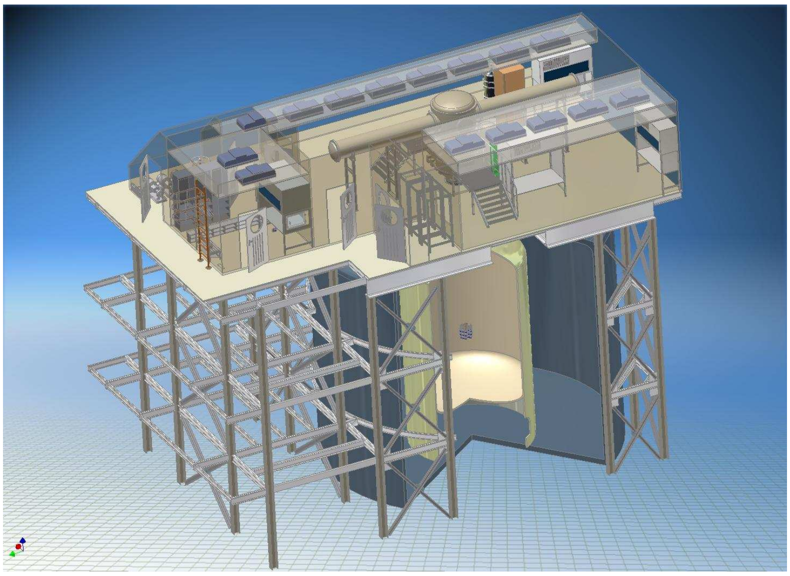

Figure 1.2: Engineer's view of the GERDA experiment. Inside the cryostat, the detector array is visible. The cryostat is surrounded by the water tank. On top of the water tank, the clean room with the lock system can be seen.

Background events do not perfectly imitate $0\nu\beta\beta$ events. Most $0\nu\beta\beta$ events will deposit their energy very locally, within a sphere with a radius of $\lessapprox 1$ mm, in so-called single-site events. Most background events are due to photons with an energy above 2 MeV, which predominantly Compton-scatter. The resulting events have multiple energy deposits, separated by typically centimeters, and are therefore called multi-site events.

These event topologies can be distinguished by carefully analyzing the pulses generated by the detectors in response to the energy depositions [13, 14, 15]. Such pulse shape analyses require that the detectors are very well understood. In addition, the power and efficiency of such analyses need to be tested on control samples. Real data samples can never be purely single-site or multi-site and are usually not distributed uniformly throughout the detector. This limits their usefulness as control samples. Therefore, also simulated pulses should be used.

Furthermore, segmented detectors can be used to separate signal from background events [16, 17, 18]. If the detector is segmented on the centimeter-level, Compton-scatterd photons are likely to deposit energy in two or more segments. Events in which energy is deposited in several segments are therefore probable to be background events. Hence, cylindrical germanium detectors that are segmented 6–fold in azimuth and 3–fold in height [19] are candidate detectors for the second phase of the GERDA experiment.

1.8 Position reconstruction using mirror pulses

Segmented detectors provide additional options for pulse shape analysis compared to unsegmented detectors. Each segment is read out separately. When energy is deposited in one segment, the produced charge carriers induce mirror charges on the electrodes of the neighboring segments. These appear as mirror pulses. They show distinct characteristics that depend on the position of the energy deposition within the hit segment.

In this thesis, a method to reconstruct the position of single energy depositions using mirror pulses is presented. The method was developed using simulated pulses generated with a recently designed pulse shape simulation program [20]. It simulates the time dependent response of all the segments of a segmented germanium detector. It was first validated with data from the segment in which energy was deposited. This thesis contains a validation of the simulated mirror pulses by comparing their shapes and amplitudes to observed mirror pulses. In addition, the method developed to reconstruct positions using simulated pulses was tested using observed pulses.

In $0\nu\beta\beta$ experiments employing germanium detectors, signal events are expected to be distributed uniformly throughout the detector, since the detector itself serves as the source. Background events, originating predominantly outside, are likely to have an inhomogeneous distribution. The events are expected to cluster in characteristic ways, revealing their origin. Position reconstruction thus provides the possibility to locate background sources and can be used as a tool to further decrease the background level in $0\nu\beta\beta$ experiments.

1.9 Thesis structure

The thesis is structured as follows:

Chapter 2 presents the basic principles of semiconductor detectors, paying particular attention to the properties of germanium crystals and segmented germanium detectors.

Chapter 3 introduces the pulse shape simulation package.

Chapter 4 demonstrates the dependence of shapes and amplitudes of simulated mirror pulses on the position of single energy depositions. Parameters quantifying these relations are introduced. A method to reconstruct the position of single energy depositions is presented and validated using simulated pulses.

Chapter 5 discusses options to obtain suitable test data sets. The experimental setup chosen and the data taking process are presented.

Chapter 6 presents the simulations of the measurements from Chapter 5.

Chapter 7 verifies the mirror pulse simulation by comparing simulated pulses to data. The method to reconstruct the position of the energy deposition is tested on observed pulses.

Chapter 2

Germanium detectors

Germanium detectors are used to detect particles via their interactions in matter. These interactions are discussed for photons, electrons and positrons. An overview of the working principle of semiconductor detectors in general and the main characteristics of germanium detectors in particular is given. The concept of segmented germanium detectors is presented as well as the signal formation process and the phenomenon of mirror charges. An example for an 18–fold segmented n-type germanium detector is introduced. A detailed review of germanium detectors can be found in [21] and references therein.

2.1 Interaction of photons, electrons and positrons with matter

2.1.1 Photons

Radioactive isotopes emit photons in the range from several keV to a few MeV. In this energy range three processes dominate the interaction of photons with matter. Their cross sections depend on the atomic number of the material and on the photon energy, E_γ:

- In the **photoelectric absorption** process, the photon transfers its entire energy to an atomic shell electron which is ejected from the shell. The kinetic energy, E_{e^-}, of this *photo-electron* is

  $$E_{e^-} = E_\gamma - E_b,$$

  where E_b is the binding energy of the electron. The remaining vacancy in the shell is filled by electrons from the outer shells and due to the differences in the binding energies characteristic x-rays or Auger electrons are emitted.

- **Compton scattering** is the elastic scattering of a photon off a quasi-free electron, transferring only a part of its energy, ΔE_γ, to the electron. The value of ΔE_γ depends on the scattering angle, Θ. It is largest for $\Theta = 180^\circ$.

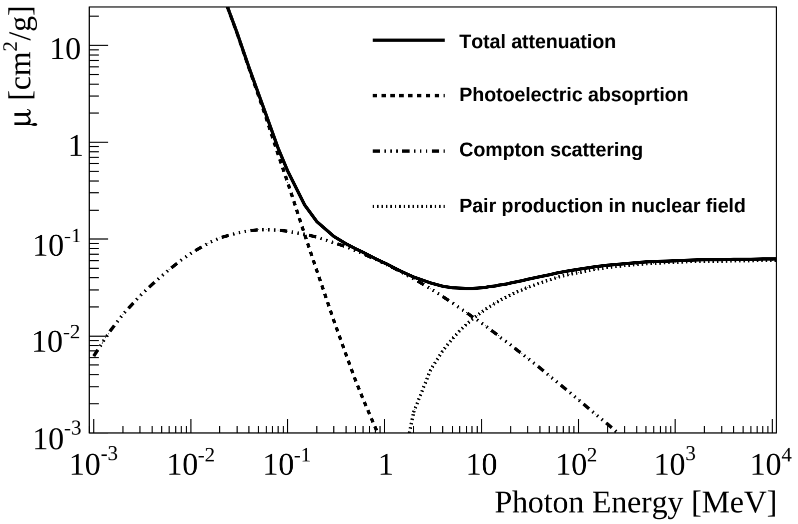

Figure 2.1: Mass attenuation coefficient μ in germanium as a function of the photon energy [22].

- If the energy of the incident photon exceeds twice the rest mass of the electron, m_e, the photon can create an electron-positron pair in a **pair production** process when in the vicinity of a nucleus. In this process, E_γ is converted to the electron and positron kinetic energies, E_{e^-} and E_{e^+}, and to their rest masses.

The mass attenuation coefficient for photons, $\mu = \frac{N_A}{A} \cdot (\sigma_{\text{photo}} + \sigma_{\text{Compton}} + \sigma_{\text{pair}})$, where N_A is Avogadro's number, A the mass number and σ_{photo}, σ_{Compton} and σ_{pair} are the cross sections for the respective processes, is shown for germanium in Fig. 2.1. The photoelectric absorption is the dominant process for photon energies up to $\approx$ 200 keV. For energies between 200 keV and about 8 MeV, Compton scattering has the highest cross section. The photon scatters several times until it is finally absorbed in a photoelectric process. The mean free path of a 1 MeV photon is about three centimeters in germanium.

For higher energies, the pair production process gains more and more importance until its cross section dominates above an energy of around 8 MeV in germanium. At 2.6 MeV, the energy of the most dominant ^{208}Tl line, its contribution to the total cross section is of $\approx$ 9%.

In each of the processes mentioned, energy is transferred to at least one electron, in case of pair production also to a positron.

2.1.2 Electrons and positrons

There are two main processes that lead to the loss of energy of electrons and positrons traversing matter. High energetic electrons and positrons lose energy mainly radiatively through the *bremsstrahlung* process. Ionization, described by the Bethe-Bloch formula [23], is the dominating effect for electrons and positrons with lower energies. In germanium, the ratio of both losses is equal for a particle energy of $\approx 18\,\mathrm{MeV}$ [24].

The energy loss mechanisms for electrons and positrons in matter are identical. The behaviour of the two particles differs, however, at the end of the track, where positrons annihilate with electrons into two photons with an energy of 511 keV each.

The range of electrons and positrons in matter depends on their energy and the material. The average range for a 1 MeV electron in germanium is about one millimeter [25].

2.2 Semiconductor detectors

The characteristics of a solid, and thus also of a semiconductor, are determined by the structure of the crystal lattice which causes allowed energy bands for the electrons with forbidden states between these bands. For a semiconductor, the gap between the valence and the conduction band, the *bandgap*, is of the order of 1 eV. Electrons can be lifted to the conduction band by thermal excitation or ionizing radiation, leaving a positively charged hole in the valence band. These electrons as well as the holes are called *charge carriers*, as they can move freely throughout the crystal. A fraction of the energy, however, goes into the excitation of phonons. Therefore, the *pair energy*, E_{pair}, the energy needed to create one electron-hole pair, is higher than the bandgap energy. In germanium at 80 K it is 2.95 eV, while the bandgap energy is only 0.7 eV.

Semiconductor materials like germanium and silicon are tetravalent. They form covalent bonds with their four nearest neighboring atoms. In *n*-type material, pentavalent impurities like boron are present. Their fifth valence electrons are only weakly bound, occupying the *donor level* slightly under the conduction band. These electrons are easily thermally excited to the conduction band, creating an abundance of negative charge carriers. In contrast, *p*-type material is doped with trivalent impurities. They are missing one covalent bond, which leads to the formation of the *acceptor level*, which is a little bit above the valence band. When electrons are lifted to these states, they leave holes in the valence band and the net amount of charge carriers remains positive.

A semiconductor detector consists of a *p*-*n*-junction. Close to the junction, the charge carriers diffuse into the volume where their concentration is lower. The electrons from the *n*-region migrate to the *p*-region and recombine with the holes, resulting in a positive space charge in the *n*-material and a negative space charge in the *p*-material from the remaining ions. This *depletion zone* is non-conducting. Any charge carrier created in this volume will be driven out by the electric field resulting from the space charges. If an external potential is applied by connecting the anode to the *n*-side and the cathode to the *p*-side (*reverse biasing*), the depletion zone is enlarged. By applying a bias voltage equal to or higher than the *full depletion voltage*, the depletion zone extends over the entire detector volume.

Semiconductor detectors are fabricated from p-type or n-type material called the *bulk*. The basic geometries used are planar and cylindrical. In the case of a planar detector, the two flat surfaces have to form the electrodes defining the potential. For cylindrical detectors, one electrode can be formed by the outer surface. In the *true coaxial* configuration, the core of the cylinder is removed, so that the inner cylindrical surface can provide the second electrode.
There are two types of electrodes, p^+ and n^+, where the "+" indicates that the net impurity density is much higher than in the bulk material. A p^+-electrode is produced by boron implantation. Its thickness is of the order of a few tenths of a micrometer. To fabricate an n^+-electrode, lithium atoms are diffused into the material. This results in a layer with a thickness of several hundred micrometers. The electrodes are metallized with aluminum, allowing the homogeneous application of an external voltage. In n-type bulk material, the p-n-junction is located on the side of the p^+-electrode. When the full depletion voltage is applied, the depletion zone extends over the entire bulk to the n^+-electrode. In p-type detectors, the opposite is the case. As the electrodes are conducting, they are not part of the depletion zone. They are thus not sensitive and form a dead volume.

2.3 Germanium detector properties

2.3.1 Operating voltage

Germanium detectors are generally operated with a fully depleted volume. The depleted volume increases with the operating voltage between anode and cathode. Its depth, d, is given by [21]

$$d = \left(\frac{2\epsilon_R \epsilon_0 V_0}{e\rho_{\text{imp}}} \right)^{1/2}$$

with V_0 being the applied reverse bias voltage, ρ_{imp} the net impurity concentration in the bulk material, e the elementary charge, $\epsilon_R = 16$ the dielectric constant of germanium, and ϵ_0 the vaccum permittivity. V_0 cannot be arbitrarily large, because on the one hand, diodes have a finite break-through voltage and on the other hand, cabling and read-out become technically challenging. Therefore, very pure material is needed for large devices with depletion depths of the order of centimeters. Techniques have been developed to produce High-Purity Germanium (HPGe) with an active impurity concentration below 10^{10} atoms/cm^3.

The largest germanium detectors have a cylindrical shape. The full depletion voltage, V_{depl}, of a true coaxial detector can be calculated as [21]

$$V_{\text{depl}} = \frac{-e \cdot \rho_{\text{imp}}}{2\varepsilon_R \varepsilon_0} \cdot \left[r_i^2 \ln(r_o/r_i) - \frac{1}{2}(r_o^2 - r_i^2) \right], \tag{2.1}$$

where r_i and r_o are the inner and outer radius, respectively. Devices with diameters and heights of up to ten centimeters and full depletion voltages of a few kilovolt are produced.

2.3.2 Operating temperature

Germanium has a very small E_{pair} of only 2.95 eV. At room temperature, a significant fraction of electrons is easily excited to the conduction band, causing a high conductivity of the detector. Applying a bias voltage would lead to a large current through the detector, making its operation as radiation detector impossible. Therefore, the detector has to be cooled. Conventionally, this is done by keeping it in thermal contact with liquid nitrogen through a cooling finger, which establishes a working temperature around 77 K. It has also been shown that the detectors can be directly submerged into the cryoliquid without loss of functionality [26].

2.3.3 Energy resolution

The energy resolution of germanium detectors, measured in terms of the full width at half maximum, FWHM, of the peak under study, is influenced by three effects.

The first one is the statistical fluctuation in the number of charge carriers created by an incident charged particle of a certain energy, E. This contribution scales with $\sqrt{E}$. It is called the *Fano term*.

The second factor that determines the energy resolution is the charge collection efficiency. It scales with E.

The last component adding to the broadening of the FWHM is the energy-independent noise contribution from the read-out electronics.

In optimized systems, total energy resolutions of about 2 keV at 1.3 MeV are obtained.

2.3.4 Segmented germanium detectors

Segmented germanium detector technology is developing rapidly as segmented detectors combine the advantage of a large-volume detector with the possibility of spatial resolution needed in nuclear gamma-ray tracking experiments like AGATA [27] and GRETA [28]. Segmented detectors can also be used for event topology reconstruction in *neutrinoless double beta-decay* ($0\nu\beta\beta$) experiments like GERDA.

The segmentation technique depends on the type of the germanium detector used. For a *p*-type detector, the outer surface is milled. The depths and widths of these grooves are of the order of a millimeter, as the lithium-drifted *n*-layer has to be penetrated and distortions of the electric field inside the detector are expected. For an *n*-type detector, photo-lithographic methods are used to create segments on the outer surface and the electric field remains quite homogeneous. Examples can be seen in Fig. 2.2.

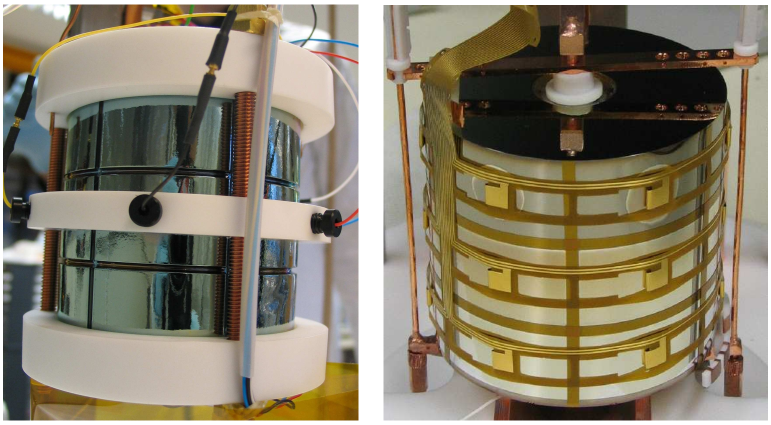

(a) (b)

Figure 2.2: (a) A segmented p-type detector. The mills separating the segments can be seen. (b) A segmented n-type detector with a readout cable made out of kapton. The segment boundaries are masked with kapton.

2.4 Signal formation

2.4.1 Charge carrier drift

Photons, electrons and positrons interact inside a semiconductor detector as described in Section 2.1, transfering energy to secondary electrons. These secondary electrons subsequently excite electrons from the valence to the conduction band, hence create electron-hole pairs. The average number of charge carriers produced is proportional to the deposited energy, because E_{pair} is independent of the type of the incident particle and of its energy.

Since a semiconductor detector is operated in reverse bias mode, the electric field in its bulk causes the drift of the electrons and holes in opposite directions towards the electrodes. To first order, the drift direction of the electrons (holes) is anti-parallel (parallel) to the electric field lines. The drift velocities grow with rising electric field strength up to a saturation field strength, E_{sat}, which is of the order of 10^2 V/ mm for electrons and about a factor three to five larger for holes. Above E_{sat}, the drift velocities remain constant, being of the order of 0.1 mm/ ns.

2.4.2 Real pulses and mirror pulses

The moving charge carriers induce charges in the electrodes of the detector. The time development of the induced charges for one electrode, $Q(t)$, follows the Shockley-Ramo Theorem [29] and can be calculated from a so-called *weighting potential*.

The induced charges are recorded over a time period $t_1 - t_0$, using charge-sensitive preamplifiers. The *pulse* at time t_1, $P(t_1)$, is proportional to the induced charges in the respective electrode integrated over the time period,

$$P(t_1) \sim \int_{t_0}^{t_1} Q(t)\,dt.$$

In a segmented detector, charges are induced on several electrodes. For every electrode, two cases can be distinguished:

1. Charge carriers reach this electrode (charge-collecting electrode).
   The pulse increases with time and a charge integral unequal to zero remains when all charge carriers have been collected by electrodes. This type of pulse is referred to as a *real pulse*.

2. No charge carriers reach this electrode.
   The pulse is a transient pulse and goes back to zero when all charge carriers have been collected by electrodes. These pulses are called *mirror pulses*.

The time development of the functional form of the integrated charges on the electrodes is referred to as the *pulse shape*.

2.5 The 18–fold segmented n-type HPGe test detector

All of the measurements described in the following were carried out with an 18–fold segmented *n*-type HPGe detector. The detector is called *Siegfried III, SIII*. It is a true coaxial cylindrical detector with a height of 70 mm and a diameter of 75 mm with a 10 mm bore hole in the center. The outer surface is 6–fold segmented in the azimuthal angle, ϕ, and 3–fold segmented in the height, z. These 18 p^+-electrodes are referred to as the *segments*, while the n^+-electrode provided by the inner surface is referred to as the *core*.

The segmentation scheme and the detector coordinate system are given in Fig. 2.3(a). The segments were read out using a Kapton flexible printed-circuit board with snap-contacts [19], depicted in Fig. 2.3(b). A picture of the detector can be seen in Fig. 2.2(b).

The depletion voltage, V_{depl}, can be determined from the dependence of the core capacitance on the applied bias voltage. This dependence was measured by Canberra France in Lingolsheim as shown in Fig. 2.4.

The capacitance decreases with increasing bias voltage until about +2500 V. At higher bias voltages, it stays constant. From this measurement, $V_{\mathrm{depl}} = +2500\,\mathrm{V}$ was estimated. The operating voltage was set to $+3000V$. It was applied to the core of SIII. The segments were connected to preamplifiers which fixed their potential to ground.

The values for the impurity density, ρ_{imp}, provided by the manufacturer were $\rho_{\mathrm{imp}} = 0.61 \cdot 10^{10}\,\mathrm{cm}^{-3}$ at the bottom and $\rho_{\mathrm{imp}} = 1.35 \cdot 10^{10}\,\mathrm{cm}^{-3}$ at the top of SIII.

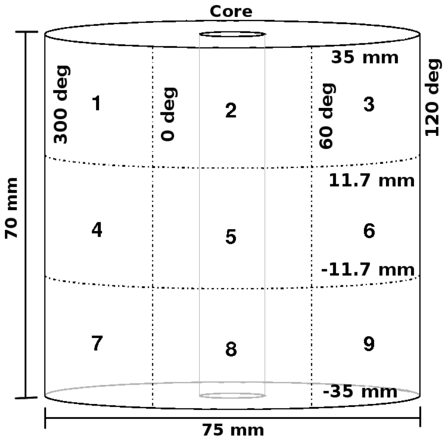

(a)

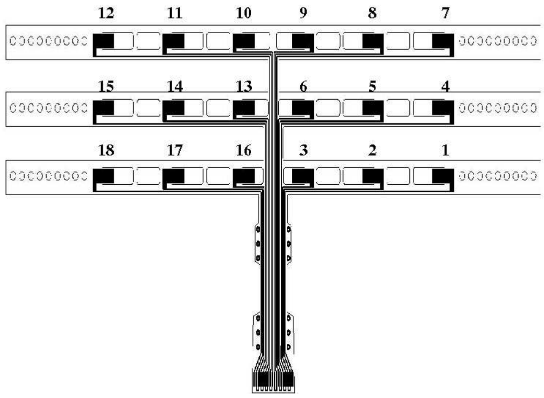

(b)

Figure 2.3: (a) Segmentation scheme of SIII and (b) readout cable scheme

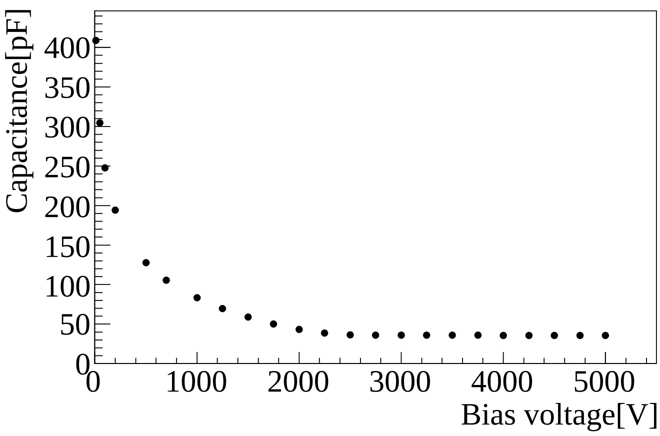

Figure 2.4: Dependence of the core capacitance on the applied bias voltage as measured by Canberra France.

Chapter 3

Pulse shape simulation

The program package [20] simulating the time development of the induced charges in the electrodes, the pulse shapes, of a germanium detector is presented. It includes the computation of the electric field and of the weighting potentials. The program takes into account the active bulk-impurity density of the detector, the crystal structure and the effects from the read-out chain.

3.1 The simulation procedure

The procedure to simulate pulse shapes consists of two components:

1. Calculation of the static properties of the detector, i.e. calculation of the electric field and the weighting potentials. This is done once at the beginning.

2. Event by event simulation, taking into account the event topology:

   - The interactions of particles with a germanium detector are simulated using the GEANT4 [30]-based Monte Carlo framework MaGe [31]. This results in a list of all interactions, the so-called *hits*, for which location and energy deposited are available.
   - The hits are grouped together in clusters if their distance is smaller than a certain value. The default value is one millimeter. The position of the cluster is the barycenter of the energies of the original hits and the energy is the sum of the energies of the original hits. For each cluster, only one electron-hole pair starting at the barycenter is simulated.
   - The drift of the charge carriers is calculated in time-steps. The velocity at each time-step is calculated using the electric field and taking into account the effects of the crystal structure.
   - The charges induced in each of the electrodes for the positions of the charge carriers after each time-step are calculated from the weighting potentials. This gives the pulse shapes for each electrode.

- Experimental effects such as decay time, limited bandwidth, and noise are folded into the pulse shapes.

3.2 Electric field and weighting potentials

The electric field can be calculated solving Poisson's equation

$$\triangle \Phi = -\rho/(\epsilon_0 \epsilon_R) \ ,$$

where Φ is the electric potential, linked to the electric field, $\mathbf{E}$, via $\mathbf{E} = -\nabla\Phi$, ρ is the space charge density, ϵ_0 is the vacuum permittivity and $\epsilon_R = 16$ is the dielectric constant of germanium. For a cylindrical segmented detector it is convenient to express Poisson's equation in cylindrical coordinates, r, ϕ, z. It becomes

$$\frac{1}{r}\frac{\partial \Phi}{\partial r} + \frac{\partial^2 \Phi}{\partial r^2} + \frac{1}{r^2}\frac{\partial^2 \Phi}{\partial \phi^2} + \frac{\partial^2 \Phi}{\partial z^2} = -\frac{1}{\epsilon_0 \epsilon_R}\rho(r, \phi, z) \ .$$

The boundary conditions for the electric potential are $\Phi \equiv 0$ on the outer mantle of the detector and $\Phi \equiv V_0$ on the inner mantle, where V_0 is the operating voltage. The lithium drifted zone around the inner mantle is taken into account in the geometry of the simulation. On the end surfaces of the cylindrical detector, the potential floats. The space charge density, $\rho(r, \phi, z)$, is determined by the active impurity density, $\rho_{\text{imp}}(r, \phi, z)$, which defines the strength of the electric field inside the detector.

In Fig. 3.1, the radial dependence of the electric field is depicted for varying homogeneous impurity densities, ρ. In all cases, an operating voltage of +3000 V is assumed.

The time development of the induced charge for one electrode, $Q(t)$, follows the Shockley-Ramo Theorem [29]. For a moving point charge q that can be found at position $\boldsymbol{r}(t)$ at time t it is

$$Q(t) = -q \cdot \Phi_\omega(\boldsymbol{r}(t)), \tag{3.1}$$

where Φ_ω is the weighting potential. Φ_ω is determined by solving the Laplace equation

$$\triangle \Phi = 0 \ .$$

The Laplace equation expressed in cylindrical coordinates becomes

$$\frac{1}{r}\frac{\partial \Phi_\omega}{\partial r} + \frac{\partial^2 \Phi_\omega}{\partial r^2} + \frac{1}{r^2}\frac{\partial^2 \Phi_\omega}{\partial \phi^2} + \frac{\partial^2 \Phi_\omega}{\partial z^2} = 0 \ .$$

The boundary conditions for Φ_ω are $\Phi_\omega \equiv 1$ on the electrode of interest and $\Phi_\omega \equiv 0$ on all other boundaries.

Poisson's equation as well as Laplace's equation are solved numerically on a grid, employing a method called Successive Over-Relaxation (SOR) and the results for each

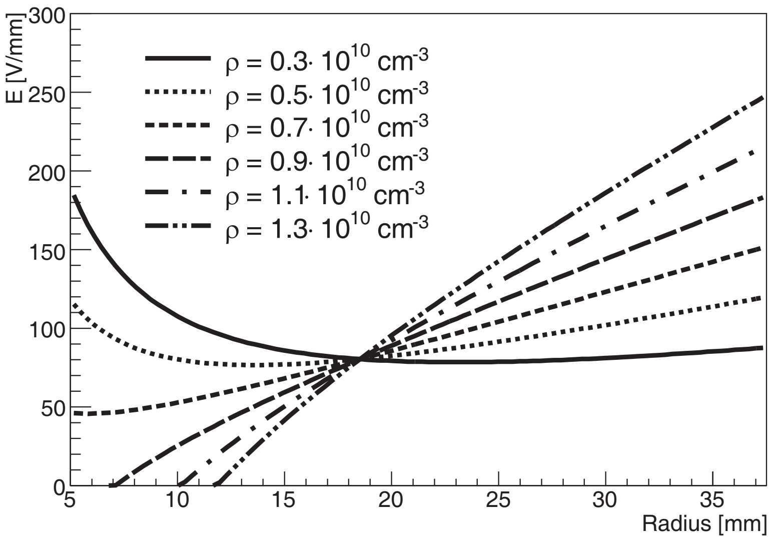

Figure 3.1: Dependence of the electric field on the radial coordinate r for different constant impurity densities, ρ, between 0.3 and $1.3 \cdot 10^{10}/\mathrm{cm}^3$ [20].

grid point are stored. For each position of the charge carriers, the corresponding values for $\mathbf{E}$ and Φ_ω are obtained by interpolation between the values of the neighboring grid points.

More details regarding the calculation of the electric field and the weighting potentials can be found in [32].

Figure 3.2 shows a cut through a detector with the indication of a charge deposition and electron and hole trajectories. The weighting potentials, calculated for segment 6, in which the energy was deposited, and for its neighbor, segment 13, are displayed in Figs. 3.2(a) and (b), respectively.

3.3 Charge carrier drift

For each of the clusters defined in Sec. 3.1, the drift trajectories of the electron and the hole are determined by calculating their drift velocities, $\mathbf{v}_e(\mathbf{r})$ and $\mathbf{v}_h(\mathbf{r})$, in time-steps, Δt, using the previously calculated electric field, $\mathbf{E}(\mathbf{r})$, at the position of the charge carrier, $\mathbf{r}$:

$$\mathbf{v}_{e,h} = \mu_{e,h}(\mathbf{r}) \cdot \mathbf{E}(\mathbf{r}),$$

where $\mu_e(\mathbf{r})$ ($\mu_h(\mathbf{r})$) is the mobility of the electrons (holes).

$\mu_{e,h}(\mathbf{r})$ depends on the relative temperatures of the germanium crystal, $\mathrm{T}_{\mathrm{crystal}}$, and of the electrons (holes), T_e (T_h) [1]. If $\mathrm{T}_{\mathrm{crystal}} \approx \mathrm{T}_{\mathrm{e,h}}$, the drift velocities are directly proportional to the electric field with $\mu_{e,h}(\mathbf{r})$ becoming numbers, $\mu^0_{e,h}$, which are independent from the crystal structure.

[1] The velocities of a group of electrons (holes) follow a Maxwell-Boltzmann distribution. Their temperature is defined as the temperature of this distribution.

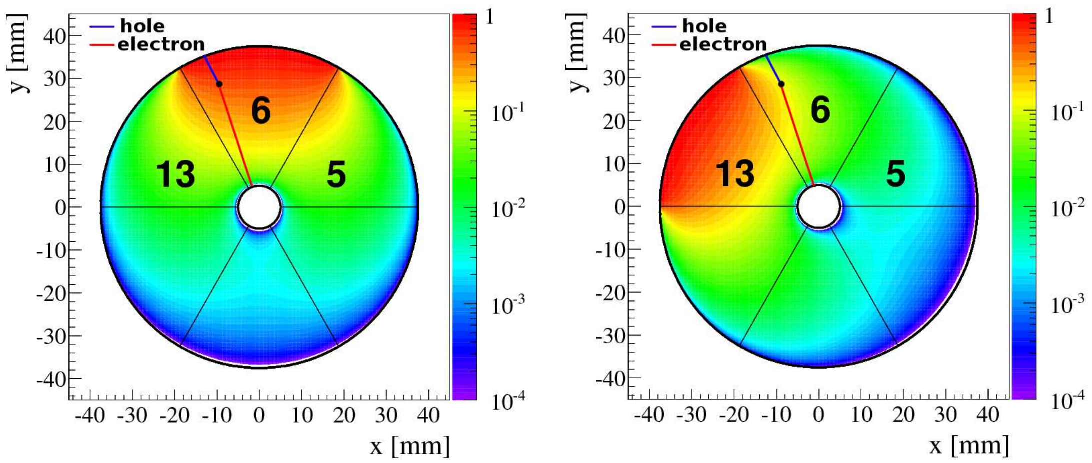

(a) (b)

Figure 3.2: Cut through a cylindrical detector with the indication of a charge deposition in segment 6. (a) Φ_ω for the segment in which energy is deposited. (b) Φ_ω for the neighboring segment.

At the operating temperatures of HPGe detectors of around 100 K, however, $T_{crystal} \ll T_{e,h}$, and the mobility becomes a complex tensor, depending on the crystal orientation. The drift velocities differ for different drift directions (longitudinal anisotropy) and are not always parallel to the electric field (transversal anisotropy) [33, 34]. The drift is only exactly parallel to the field lines when these are parallel to the crystal axes.

The crystal structure of a germanium crystal is face-centered-cubic (FCC) and the crystal axes, expressed in Miller indices, are <111>, <110> and <100>. For cylindrical detectors, the axis <001> is aligned to the z-axis, which is implemented in the simulation. In the $r\phi$-plane, the position of the axes <100> and <110> relative to the segment boundaries can be adjusted according to the detector which is simulated.

Measurements of the drift velocities along the crystal axes are parametrized to extract the tensor elements of $\mu_{e,h}$. Due to the longitudinal anisotropy, the magnitude of the mobility varies for different crystal axes. The drift time for charge carriers is minimal along the axis <100> and maximal along the axis <110>.

In Fig. 3.3(a), the drift trajectories of electrons, coming from the outer surface, are projected on the xy-plane. In Fig. 3.3(b), the same is done for holes, originating on the inner surface of the detector. The crystal axis <110> is aligned to the x–axis and the starting points are distributed equidistantly on the outer and inner mantle, respectively, taking into account the lithium drifted zone on the inner surface. The operating voltage is set to 3 kV. The drift time considered is 400 ns, within which not all of the holes reach the segment electrodes, while all electrons arrive at the inner surface. This is explained by the fact that electrons drift faster than holes. The differences in the distances traveled by the holes for different starting positions clearly reveal the lon-

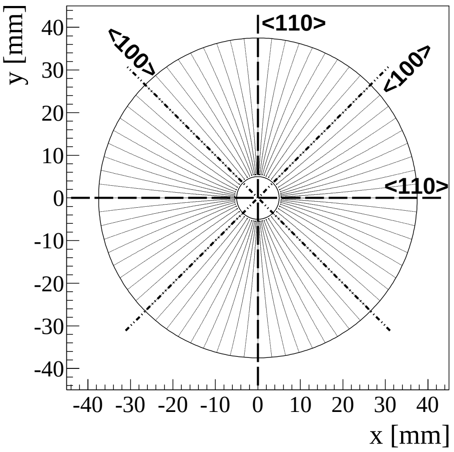

(a)

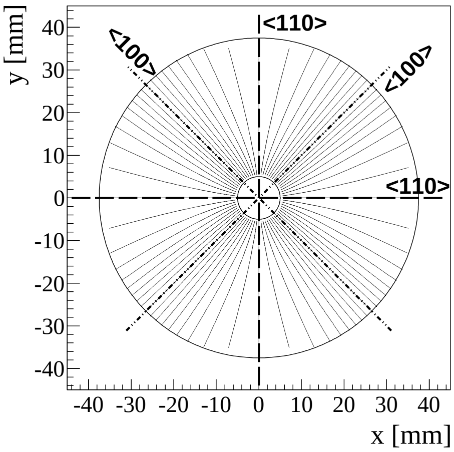

(b)

Figure 3.3: (a) Trajectories of electrons drifting inward from the outer mantle. (b) Trajectories of holes drifting outward from the inner mantle.

gitudinal anisotropy. Along the crystal axes, the drift trajectories are straight. Along other directions, however, they are bent, making apparent the transversal anisotropy.

The combination of the velocity measurements along the axes <111> and <100> allows to determine the mobility for any point in the crystal. The details of the calculation and the parameters used in the simulation can be found in [35] and references therein.

3.4 Time development of the induced charges

A fourth order Runge-Kutta method is used to determine the position of each charge carrier at each time-step. A step-length, $\Delta t = 13.3\,\mathrm{ns}$, is chosen for all simulations in accordance with the sampling period of the data aquisition system, DAQ. Equation (3.1) is used to calculate the charges induced in the electrodes for each time-step by summing up the contributions of all charge carriers.

In general, charge sensitive amplifiers are used for germanium detectors. In accordance, the induced charges are integrated over time. The result is the time development of the induced charges, the raw pulse.

The core pulse of the event indicated in Fig. 3.2 is shown in Fig. 3.4. Also shown are the pulses of segment 6, in which energy was deposited, and its left and right neighbors, segments 5 and 13.

3.5 Effects of the electronics

The simulated raw pulses are quite different from measured pulses. A pulse decays with a time constant, τ, to allow the amplifier output level to return to its baseline.

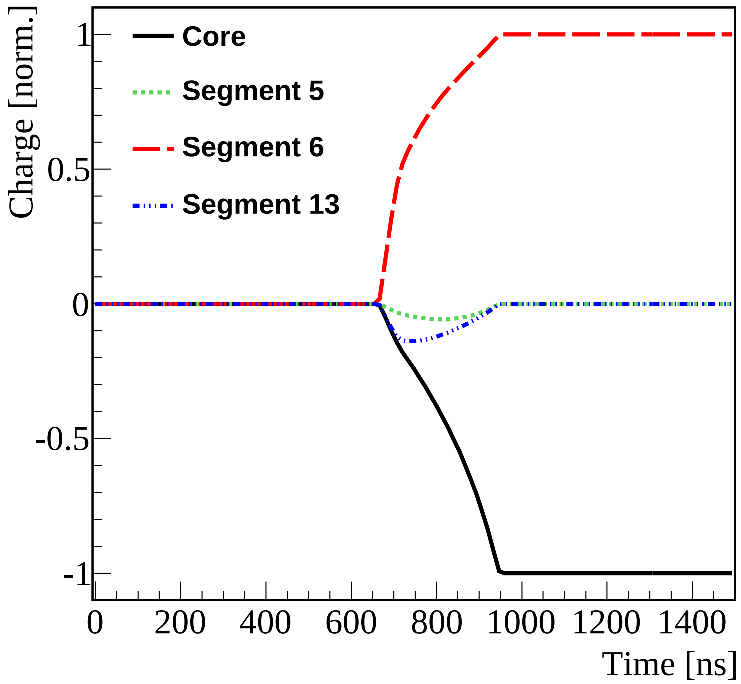

Figure 3.4: Real pulses of the core and the hit segment and mirror pulses of the neighboring segments.

In addition, the bandwidth of the amplifiers and of the transmission cables is limited. Frequencies higher than the bandwidth limit are cut off and sharp edges in a pulse are smeared out. Another strong effect is electronic noise. Since all these electronic effects change the shape as well as the amplitude of the pulses, they have to be simulated and the raw pulses have to be changed accordingly.

Figure 3.5 shows the modified pulses of segments 5, 6, and 13 after folding in the decay, the limited bandwidth, and Gaussian noise. The decay constant $\tau = 50\,\mu$s and the bandwidth-cutoff is 10 MHz. The noise level is set to 0.25% of the pulse amplitude, which represents the situation for the double escape peak, DEP, events of the 2.6 MeV line of ^{208}Tl. The smoothing of the pulses by the limited bandwidth makes the start and end of the pulse become less distinct. The most important effect is the noise. The small mirror pulse in segment 5 is much less evident in Fig. 3.5(d) after noise is added.

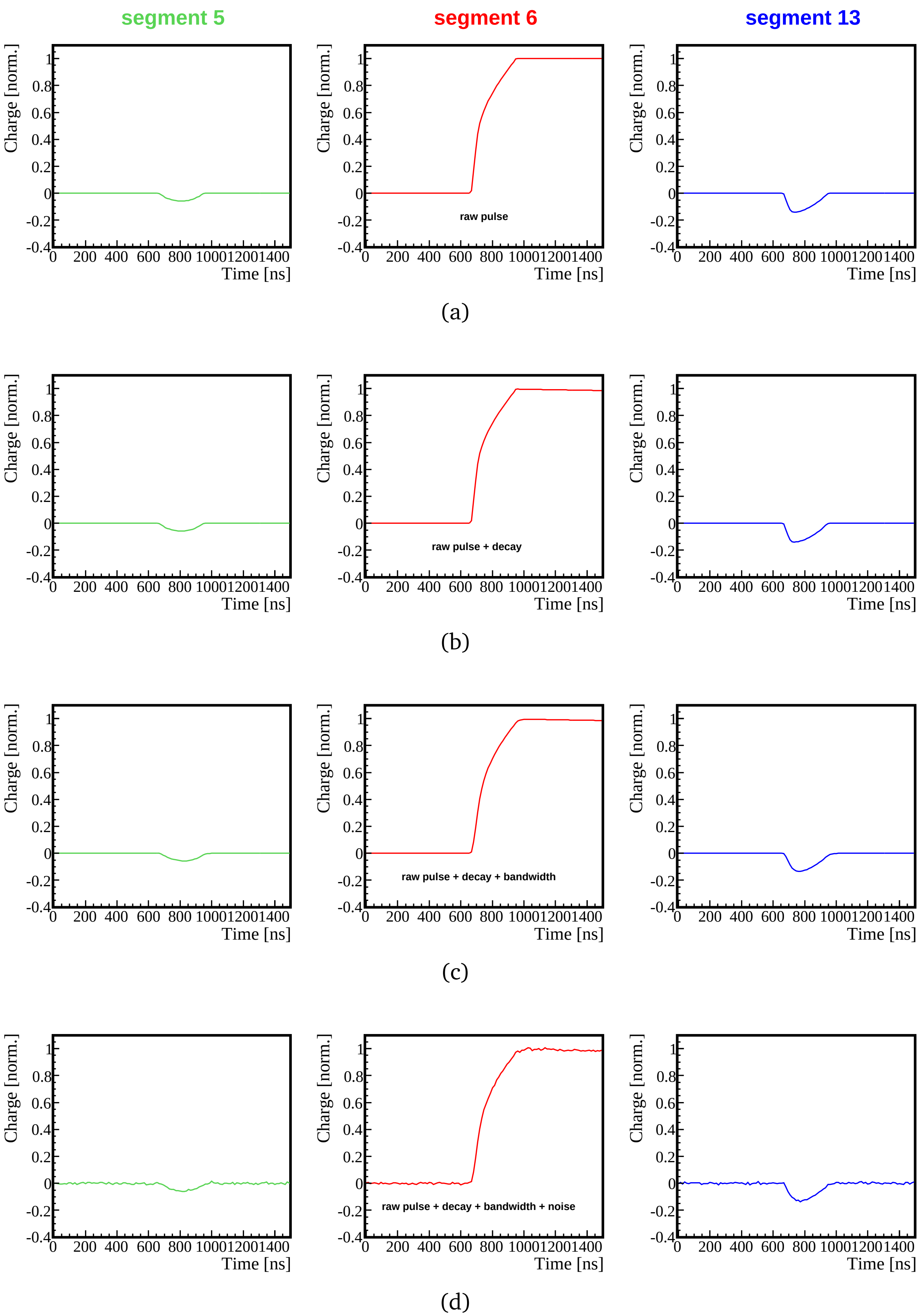

Figure 3.5: Raw pulses (a) and modified pulses after folding in the decay (b), the decay and the limited bandwidth (c), the decay, the limited bandwidth and the noise (d).

.

Chapter 4

Position reconstruction of energy depositions using mirror pulses

As mentioned in Sec. 1.8, position reconstruction of energy depositions is a powerful tool for the detection and localization of background sources in experiments searching for $0\nu\beta\beta$. It will also play an important role in future γ-tracking experiments like GRETA [28] and AGATA [27].

Mirror pulses show distinct features that depend on the position of the energy deposition in a segmented detector. This dependence is demonstrated for single energy depositions using pulse shape simulation. Parameters quantifying the relation are introduced and a method to reconstruct the position for single energy depositions using these parameters is presented.

4.1 Characteristics of mirror pulses

When energy is deposited in one segment of a segmented HPGe detector, mirror charges are induced in the electrodes of the adjacent segments. These mirror charges and the corresponding mirror pulses were introduced in Sec. 2.4. The shapes and amplitudes of the mirror pulses are highly dependent on the position of the energy deposition [36, 37, 19].

In the following, the 18–fold segmented n-type HPGe detector SIII, presented in Sec. 2.5, is considered. The coordinate system is defined in Fig. 2.3(a). A cut through the $r\phi$-plane at the detector center, $z = 0$, is shown in Fig. 4.1.

For all simulations, the impurity density was set to $\rho_{\text{imp}} = 0.7 \cdot 10^{10}\text{cm}^{-3}$ and the angle between the crystal axis <110> and the x-axis was set to 32°. This is in correspondence to SIII.

Mirror pulses carry two kinds of information regarding the position of single energy depositions:

1. **Distance from crystal center:** The polarity of the mirror pulse gives information

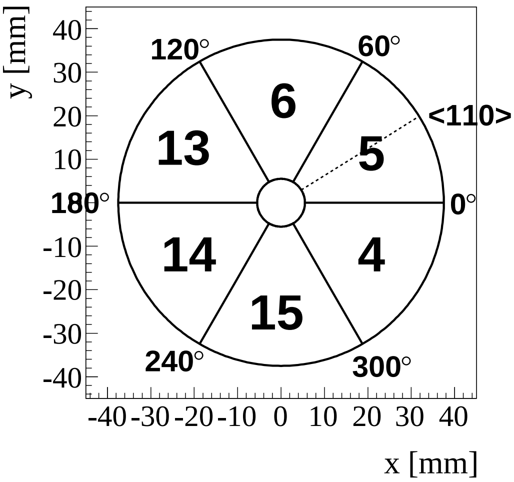

Figure 4.1: Projection on the $r\phi$-plane at the detector center, $z = 0$. The segments forming the middle layer of the detector are indicated. The crystal axis <110> is indicated at $\phi = 32°$.

about the radial coordinate, r, at which energy was deposited. It is positive for energy depositions at small r, because the electrons are collected before the holes and the drifting holes induce a positive charge. For large r, the opposite is the case, since the mirror pulse is induced by the electrons drifting towards the core electrode. At intermediate radii, the contributions from holes and electrons are nearly equal. Since the two contributions cancel out, the effective amplitude is small. The amplitude is defined as the maximum deviation from the baseline. A mirror pulse can also change polarity during its time development, if it is first dominated by the drift of one and then of the other type of charge carrier.

2. **Distance to neighboring segment:** The closer the energy was deposited to a neighboring segment, the higher is the absolute value of the amplitude of the mirror pulse in this neighboring segment. The amplitudes of the mirror pulses in the left and right neighboring segments, A_l and A_r, thus carry information about the azimuthal position, ϕ. The amplitudes of the mirror pulses in the upper and lower neighboring segments, A_u and A_d, provide information on the vertical position, z.

Figure 4.2 demonstrates the position dependence of mirror pulses using simulated pulses. Energy is deposited in segment 5 at varying r and varying ϕ at fixed $z = 0$. The corresponding real pulse for segment 5 and the mirror pulses for the left neighboring segment (segment 4) and the right neighboring segment (segment 6) are depicted. Left is defined as a clockwise rotation when looking from above on the $r\phi$-plane. Accordingly, the right neighbor lies in the counterclockwise direction from the segment with the energy deposition. The pulses were generated for a single electron-hole pair and the amplitudes of the real pulses were normalized to 1. The

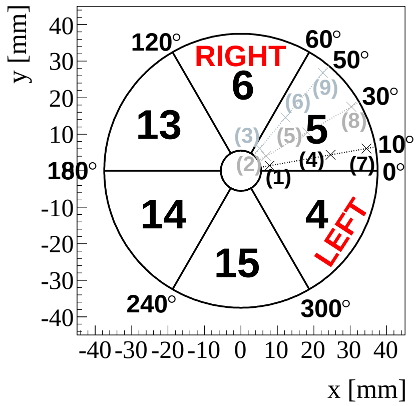

(a)

	r [mm]	ϕ [°]	z [mm]
(1)	8	10	0
(2)	8	30	0
(3)	8	50	0
(4)	25	10	0
(5)	21	30	0
(6)	19	50	0
(7)	35	10	0
(8)	35	30	0
(9)	35	50	0

(b)

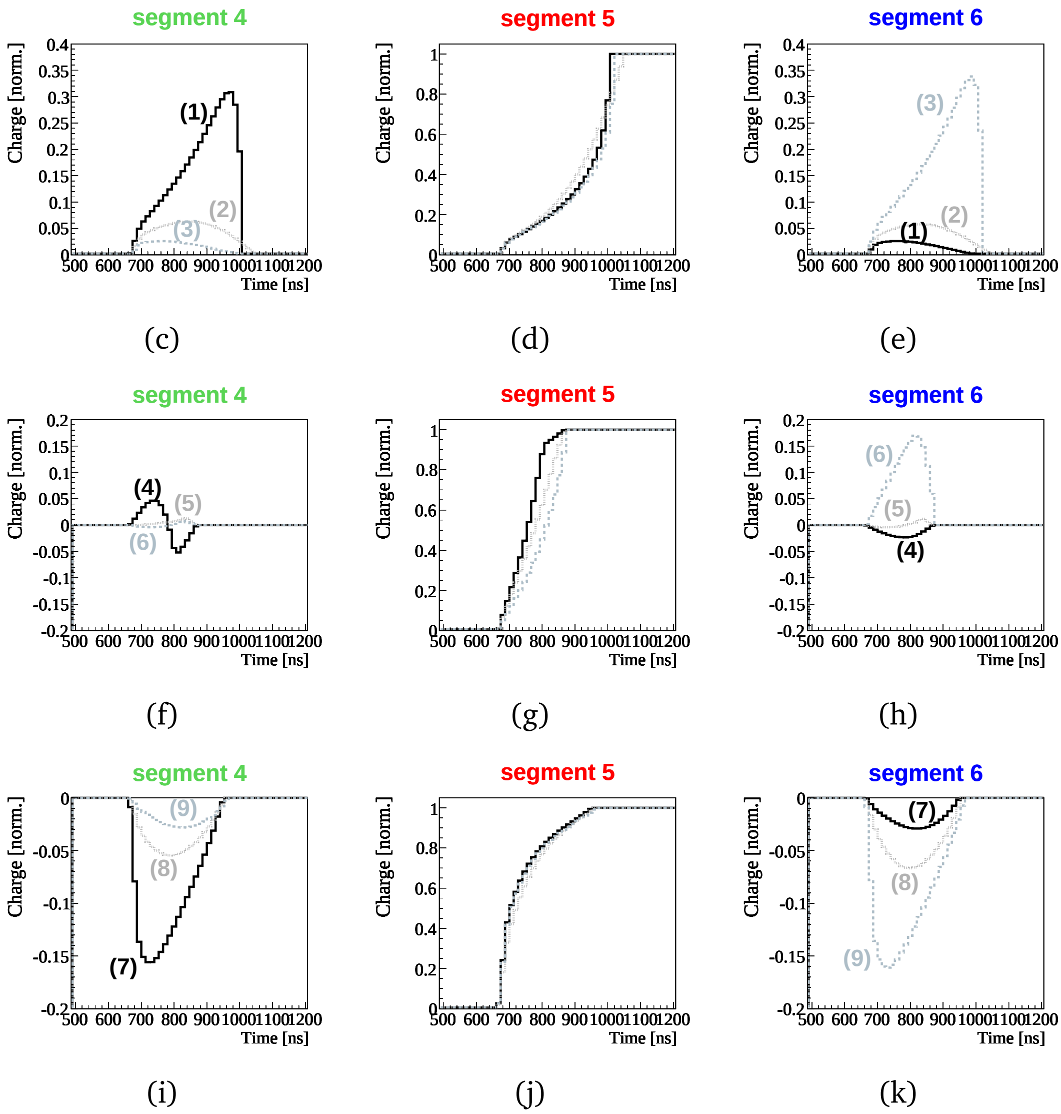

Figure 4.2: (a) Indication of nine locations of energy depositions in segment 5 with $z = 0$ and varying r and ϕ. Segment 4 is called left, segment 6 is called right neighboring segment. (b) List of the locations of energy deposition. (c)-(k) Corresponding mirror pulses in segments 4 and 6 and real pulses in segment 5. The amplitudes of the real pulses are normalized to 1. The mirror pulses are normalized to the real pulses. Note the varying scales.

mirror pulses were normalized to the core pulse. In the following, this normalization is always applied. Note the different scales for real and mirror pulses and for mirror pulses at different r.

For Figs. 4.2(c-e), the electron-hole pair was generated at small $r = 8\,\mathrm{mm}$, resulting in positive mirror pulses. For Figs. 4.2(i-k), the electron-hole pair was generated at large $r = 35\,\mathrm{mm}$, leading to a negative polarity of the mirror pulses. In both cases, the absolute values of the amplitudes increase with decreasing distance between the respective segment boundary and the position of the energy deposition. Figures 4.2(f-h) depict the pulses for energy depositions at r where the polarity of the mirror pulses changes. This r depends on the distance between the position of energy deposition and the segment boundary. If the electron-hole pair is generated at a distance of 10° to the segment boundary, the polarity of the mirror pulse in the respective neighboring segment changes at $r \approx 25\,\mathrm{mm}$. The mirror pulse is first positive and then negative. The mirror pulse in the other neighboring segment has a negative polarity. Close to the segment center, the polarity changes for energy depositions at $r \approx 21\,\mathrm{mm}$. The mirror pulses in both neighboring segments almost vanish, as the contributions from electrons and holes are of the same order and cancel. If the electron-hole pair is generated at a distance of 50° to the segment boundary, the polarity of the mirror pulse in the respective neighboring segment changes at $r \approx 19\,\mathrm{mm}$. The polarity is first negative and then positive, with very small amplitudes. The mirror pulse in the other neighboring segment exhibits a much larger positive amplitude.

The behavior of the mirror pulses was studied not only for selected positions. Electron-hole pairs were generated evenly distributed in the $r\phi$-plane at $z = 0$. The grid in the $r\phi$-plane had a 1 mm spacing in the x- and y-direction, respectively. The same was done in the rz-plane at $\phi = 30^\circ$. A spacing of 1 mm in the r- and z-direction was applied. In Fig. 4.3, (a) A_l, (b) A_r, (c) A_u, and (d) A_d, are depicted. The amplitude of the respective mirror pulse is plotted at the position where the electron-hole pair is produced. If a mirror pulse has a negative as well as a positive amplitude, the one with the higher absolute value is plotted.

The above mentioned characteristics can be seen clearly. In all cases, the amplitude of the mirror pulse rises as the position of the energy deposition approaches the respective segment boundary. At $r \approx 18-25\,\mathrm{mm}$, the change from positive to negative amplitudes can be observed. The dependence of r, at which this transition happens, on the distance between the position of the energy deposition and the segment boundary is observable.

It is also clearly visible that the actual segment boundaries are not at 0°, 60°, 120°, 180°, 240°, and 300°. In Fig. 4.3(b), for instance, the band of highest amplitudes is shifted away from the 60° segment boundary. This can be accounted for by the transversal anisotropy of the drift trajectories due to the crystal axes. As a result, the effective volume of a segment differs, depending on the relative position of the

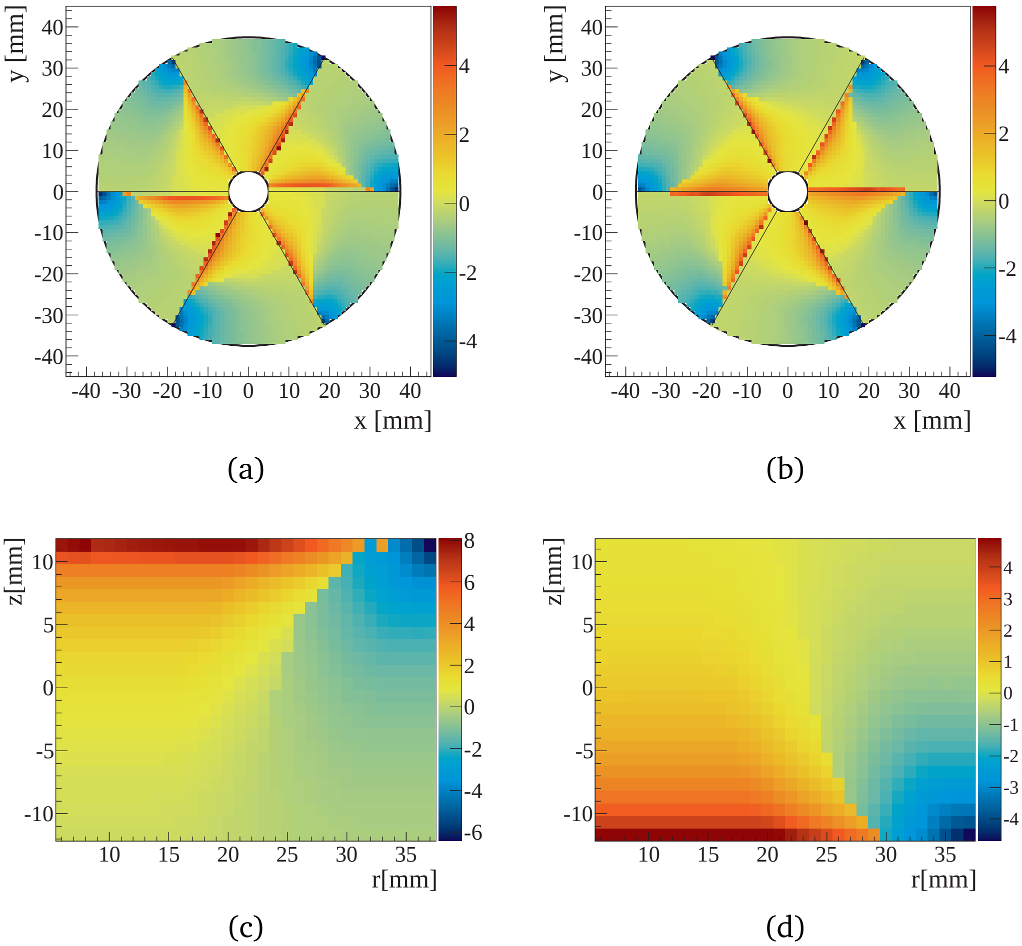

Figure 4.3: (a) Normalized A_l (b) Normalized A_r (c) Normalized A_u (d) Normalized A_d. The amplitude of the mirror pulse is plotted at the point where the electron-hole pair causing it was produced. (a) and (b): $z = 0$. (c) and (d): $\phi = 30°$.

segment boundaries to the crystal axes.

4.2 Pulse amplitude reconstruction

As long as pulses are simulated without noise, the reconstruction of the amplitudes is trivial. Since noise has to be applied when efficiencies and resolutions are to be evaluated, the reconstruction has to be suitable under such circumstances.

A pulse consists of a sequence of samples, each covering a time period $\Delta t = 13.3\,\mathrm{ns}$, as presented in Sec. 3.4. To smooth out the noise, a Gaussian filter is applied to the mirror pulses. The smoothed value of a sample, Q_S, is calculated taking into account its unsmoothed value, Q_0, and the unsmoothed values of the two samples to its left, Q_{-1} and Q_{-2}, and to its right, Q_1 and Q_2. The time corresponding to the center of the sample whose value is to be calculated is denoted with t_0. A Gaussian function, $G(t) = c \cdot \exp(-(t-\mu)^2/2\sigma^2)$, is defined,

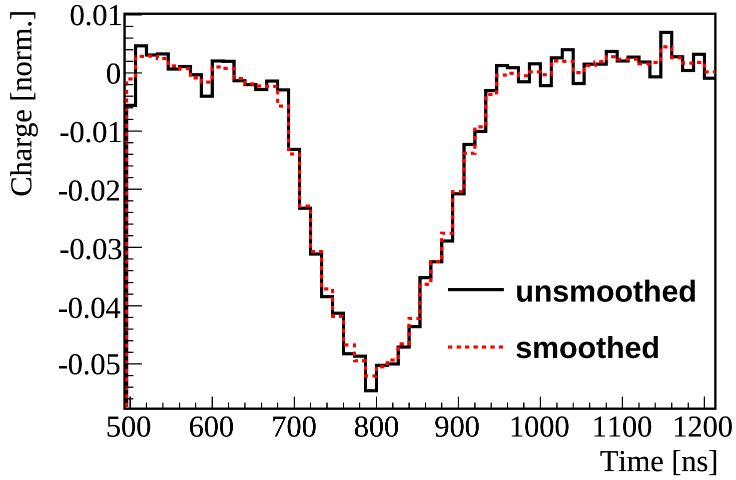

Figure 4.4: The unsmoothed pulse for an energy deposition at $r = 30\,\text{mm}$, $\phi = 30°$, $z = 0\,\text{mm}$ is drawn in black. The smoothed pulse after the application of the Gaussian filter is drawn with a red dashed line.

with mean value $\mu = t_0$, width σ with $3\sigma = 2.5\Delta t$, and amplitude c such that $G(t_0 - 2\Delta t) + G(t_0 - \Delta t) + G(t_0) + G(t_0 + \Delta t) + G(t_0 + 2\Delta t) = 1$.

Q_S is then calculated as

$$Q_S = \sum_{i=-2}^{+2} G(t_0 + i \cdot \Delta t) \cdot Q_i.$$

In Fig.4.4, a simulated mirror pulse is depicted before and after the application of the Gaussian filter. To illustrate the effect of the filter, electronics effects are added. The values correspond to the situation for DEP events of the 2.6 MeV line of ^{208}Tl. The decay constant was set to $\tau = 50\,\mu$s, the bandwidth-cutoff to 10 MHz, and the noise level to 0.25% of the pulse amplitude.

The amplitude of a mirror pulse is reconstructed by determining the maximum deviation from the baseline of the smoothed mirror pulse. If the amplitude is smaller than two times the noise level, it is set to zero. All further analysis is done with amplitudes that have been reconstructed in this way.

4.3 Mirror pulse parameters

In order to quantify the dependences of the shapes of the mirror pulses on the location of the interaction point, parameters have to be introduced.

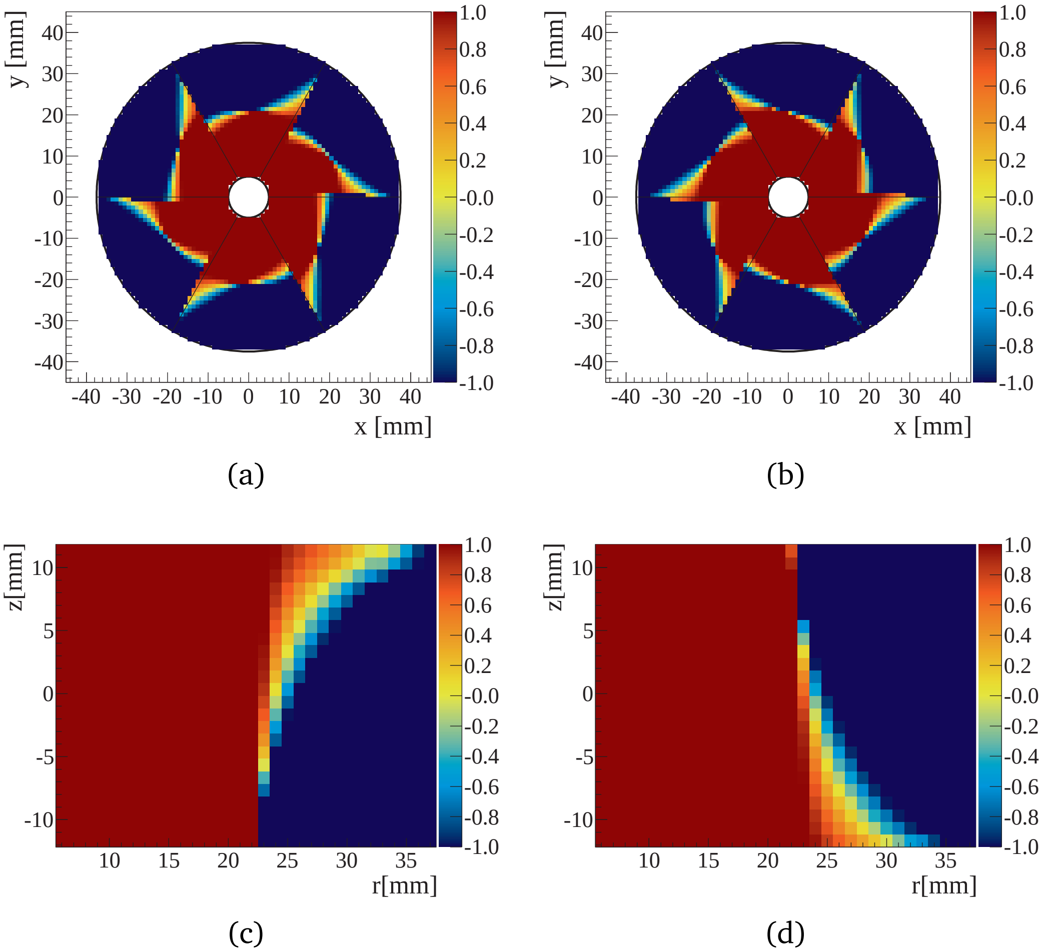

Figure 4.5: (a) τ_l (b) τ_r (c) τ_u (d) τ_d. The type of the mirror pulse is plotted at the point where the electron-hole pair causing it was produced. (a) and (b): $z = 0$. (c) and (d): $\phi = 30°$.

4.3.1 Type

To quantify the radial position information, the *type*, τ, of the mirror pulse,

$$\tau = (|A_p| - |A_n|)/(|A_p| + |A_n|)$$

is introduced, where $|A_p|$ and $|A_n|$ are the absolute values of the positive and the negative amplitude of a mirror pulse, calculated as presented in Sec. 4.2.

This definition yields $\tau = +1$ for mirror pulses with a positive polarity like the examples depicted in Figs. 4.2(c) and (e), $-1 < \tau < +1$ for mirror pulses with a positive and a negative amplitude as seen in Fig. 4.2(f), and $\tau = -1$ for mirror pulses with a negative polarity as depicted in Figs. 4.2(i) and (k). The distributions of τ for mirror pulses induced in the left and right neighboring segments, τ_l and τ_r, for energy depositions uniformly distributed in the $r\phi$-plane at $z = 0$ are shown in Figs. 4.5(a) and (b). Figures 4.5(c) and (d) show τ of the mirror pulses in the upper and lower

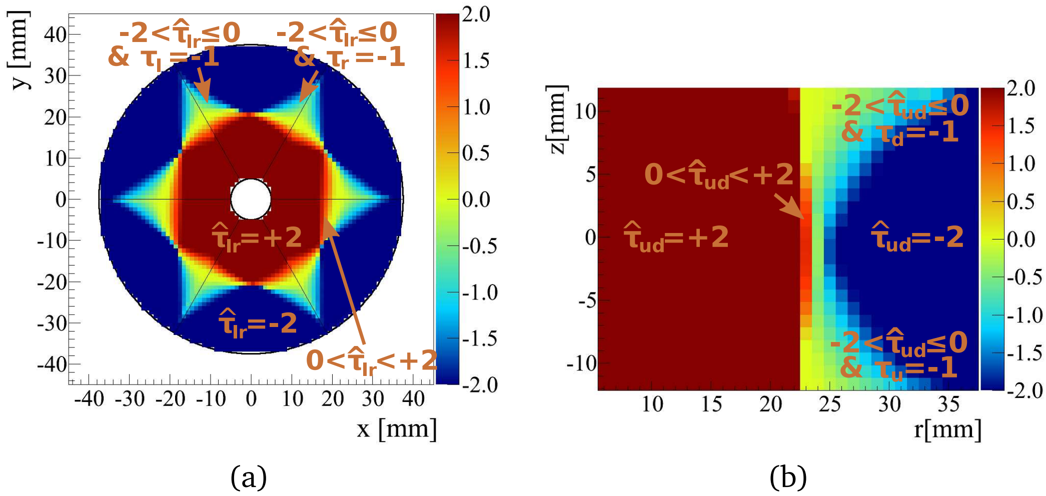

Figure 4.6: (a) $\hat{\tau}_{lr}$ (b) $\hat{\tau}_{ud}$. The value of $\hat{\tau}_{lr}$ and $\hat{\tau}_{ud}$, respectively, is plotted at the point where the electron-hole pair causing it was produced. The regions where the different categories of $\hat{\tau}_{lr}$ and $\hat{\tau}_{ud}$ appear are labeled. (a): $z = 0$. (b): $\phi = 30°$.

neighboring segments, τ_u and τ_d, for the rz-plane at $\phi = 30°$. The respective value of τ was plotted at the position of the energy deposition.

As expected, $\tau_i = -1$, with $i = l, r, u, d$, for mirror pulses originating from energy depositions in the outer part of the cylindrical volume, i.e. at large r, since the hole is collected quickly by the segment electrode and the electron drifting to the core electrode dominates the shape of the mirror pulse. Correspondingly, $\tau_i = +1$ close to the inner surface of the detector, i.e. at small r. Events with $-1 < \tau_l < +1$ ($-1 < \tau_r < +1$) are found from $r \approx 18 - 22$ mm and close to the left (right) segment boundary. Events with $-1 < \tau_u < +1$ ($-1 < \tau_d < +1$) are found from $r \approx 18-22$ mm and close to the upper (lower) segment boundary.

In order to combine the information from both neighboring segments, $\hat{\tau}_{lr} = \tau_l + \tau_r$ and $\hat{\tau}_{ud} = \tau_u + \tau_d$ are defined. If both mirror pulses are entirely negative, $\hat{\tau}_{lr} = -2$ ($\hat{\tau}_{ud} = -2$). If both mirror pulses are entirely positive, $\hat{\tau}_{lr} = +2$ ($\hat{\tau}_{ud} = +2$). In all other cases, $|\hat{\tau}_{lr}| < 2$ ($|\hat{\tau}_{ud}| < 2$). In Fig. 4.6(a), $\hat{\tau}_{lr}$ is depicted for the $r\phi$-plane at $z = 0$. Figure 4.6(b) shows $\hat{\tau}_{ud}$ for the rz-plane at $\phi = 30°$.

The events can be categorized as follows for the case of $\hat{\tau}_{lr}$:

I$_{\phi}$**:** $\hat{\tau}_{lr} = +2$,

II$_{\phi}$**:** $0 < \hat{\tau}_{lr} < +2$,

IIIa$_{\phi}$**:** $-2 < \hat{\tau}_{lr} \leq 0$ with $\tau_l = -1$, $-1 < \tau_r \leq +1$

IIIb$_{\phi}$**:** $-2 < \hat{\tau}_{lr} \leq 0$ with $\tau_r = -1$, $-1 < \tau_l \leq +1$

IV$_{\phi}$**:** $\hat{\tau}_{lr} = -2$

For the case of $\hat{\tau}_{ud}$, the categories are:

I$_z$: $\hat{\tau}_{ud} = +2$,

II$_z$: $0 < \hat{\tau}_{ud} < +2$,

IIIa$_z$: $-2 < \hat{\tau}_{ud} \leq 0$ with $\tau_u = -1$, $-1 < \tau_d \leq +1$

IIIb$_z$: $-2 < \hat{\tau}_{ud} \leq 0$ with $\tau_d = -1$, $-1 < \tau_u \leq +1$

IV$_z$: $\hat{\tau}_{ud} = -2$

The zones where the different categories appear are marked in Fig. 4.6.

Events in category I$_\phi$ cover $\approx 27\%$ of the $r\phi$-plane, events in category II$_\phi$ $\approx 6\%$, events in categories IIIa$_\phi$ and IIIb$_\phi$ $\approx 7\%$ and events in category IV$_\phi$ cover the largest part, $\approx 60\%$.

4.3.2 Left-right and up-down asymmetries

The position information in ϕ is quantified using the amplitudes of the mirror pulses in the neighboring segments as defined in Sec. 4.2 and depicted in Fig. 4.3. The left-right asymmetry, α_{lr}, is defined as

$$\alpha_{lr} = \log_{10}(|A_l|/|A_r|).$$

Accordingly, the up-down asymmetry, α_{ud},

$$\alpha_{ud} = \log_{10}(|A_u|/|A_d|),$$

is a measure for the position in z. The parameter α_{ud} can only be calculated for the middle layer of the detector. If $-1 < \tau_i < +1$, that is, the mirror pulse has a positive as well as a negative amplitude, the one with the higher absolute value is used to calculate the asymmetry. Asymmetries are also calculated in case of differing type of the two mirror pulses determining it. By doing so, α_{lr} is defined for every event and α_{ud} is defined for every interaction in the middle layer of the detector.

The distributions of the asymmetries are shown in Fig. 4.7 for the $r\phi$-plane at $z = 0$ and for the rz-plane at $\phi = 30°$. By plotting α_{lr} (α_{ud}) at the production position of the electron-hole pair, its dependence on ϕ (z) becomes evident. The asymmetry is large and positive for interactions close to the left (upper) neighboring segment due to large $|A_l|$ ($|A_u|$) and small $|A_r|$ ($|A_d|$) for these positions. It decreases with increasing ϕ (z) and vanishes at the segment center, where $|A_l| \approx |A_r|$ ($|A_u| \approx |A_d|$) and therefore $\log_{10}(|A_l|/|A_r|) \approx 0$ ($\log_{10}(|A_u|/|A_d|) \approx 0$). Close to the right (lower) segment boundary, the asymmetry is negative with large absolute values.

4.4 Position reconstruction

The mirror pulse parameters $\hat{\tau}_{lr}$ and $\hat{\tau}_{ud}$, and α_{lr} and α_{ud} are used to determine the position of single energy depositions.

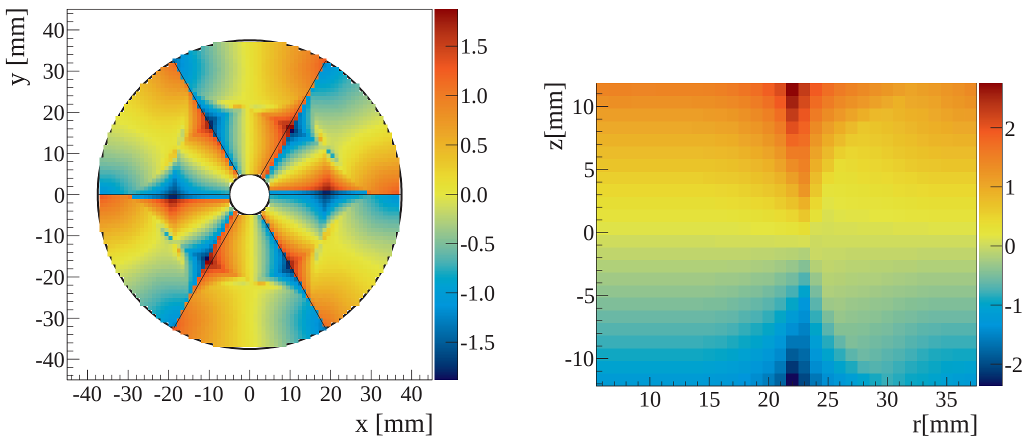

(a) (b)

Figure 4.7: (a) α_{lr} (b) α_{ud}. The asymmetry is plotted at the point where the electron-hole pair causing it was produced. (a): $z = 0$. (b): $\phi = 30°$.

4.4.1 Radius

Observing $\hat{\tau}_{lr}$ ($\hat{\tau}_{ud}$) of an event allows a rough determination of the radial coordinate.

According to the simulation, events in categories IV$_\phi$ and IV$_z$ are located at $r > 22$ mm, whereas events in categories I$_\phi$ and I$_z$ are only found for interactions at $r < 22$ mm. For mirror pulses in categories II$_\phi$ and II$_z$, the energy was deposited at intermediate r, 18 mm $< r <$ 22 mm. Events in categories IIIa$_\phi$, IIIb$_\phi$ and IIIa$_z$, IIIb$_z$ arise from energy depositions at 19 mm $< r <$ 35 mm.

As this is only a coarse classification, other methods are needed to refine the determination of the position in r. Typically, this is done by measuring the rise-time of the core or segment real pulse. It is minimal at positions for which the drift times of the electrons and the holes are equal, hence at intermediate r. The rise-time increases for smaller and for larger r, since the distance traveled becomes longer for either electrons or holes. This can be clearly seen in Figs. 4.2(d), (g), and (j). Taking into account also crystal axes effects, the rise-time can be used to deduce the radial position [37, 19]. However, there is an ambiguity in the radius determination [38] due to the increase in the rise-time for small as well as for large r. This can be resolved by taking into account the type of the mirror pulses.

4.4.2 Azimuth angle

The position in ϕ can be derived from α_{lr}. Electron-hole pairs were created in the $r\phi$-plane in steps of $\Delta r = 1$ mm and $\Delta\phi = 1°$. This was done for $z = 0$ mm, 6 mm, 10 mm (middle layer) and 14 mm, 20 mm, 26 mm, 32 mm (top layer) to study possible effects depending on z. Due to the cylindrical symmetry and the homogeneous ρ_{imp}, the outcome would be the same for the lower half of the detector. As the simulation will be compared to data, electronics effects mimicking the situation for DEP events of the

2.6 MeV line of ^{208}Tl were added to the pulse shapes. The decay constant was set to $\tau = 50\,\mu$s, the bandwidth-cutoff to 10 MHz, and the noise level to 0.25% of the pulse amplitude.

The correlation between α_{lr} and ϕ is shown in Figs. 4.8 and 4.9 for events from all seven heights. The events were selected to have the real pulse in segments 2 or 5. In Figs. 4.8 and 4.9 and all following figures in this section, $\hat{\tau}$ is used as an abbreviation for $\hat{\tau}_{lr}$.

Also shown in Figs. 4.8 and 4.9 are fits to first-order polynomials,

$$\phi_{\text{fit}} = s_\phi \cdot \alpha_{lr} + \phi_0. \tag{4.1}$$

The fits were performed separately for events in the different categories of $\hat{\tau}_{lr}$. The events with $-2 < \hat{\tau}_{lr} \leq 0$ split up into two categories, categories IIIa$_\phi$ and IIIb$_\phi$. The events in category IIIa$_\phi$ ($\tau_l = -1$ and $-1 < \tau_r \leq +1$) have predominantly $\alpha_{lr} < 0$ and are located at $30° < \phi < 60°$. The events in category IIIb$_\phi$ ($\tau_r = -1$ and $-1 < \tau_l \leq +1$) have predominantly $\alpha_{lr} > 0$ and are located at $0° < \phi < 30°$. These two groups of events can also be distinguished in Figs. 4.5(a) and (b): Events in category IIIa$_\phi$ are located close to the right segment boundaries at $r > 20$ mm. Events in category IIIb$_\phi$ can be seen close to the left segment boundaries at $r > 20$ mm.

There were no events that did not fall into one of the categories I$_\phi$, II$_\phi$, IIIa$_\phi$, IIIb$_\phi$, or IV$_\phi$.

Nominal segment boundaries are not identical with effective segment boundaries. This was already seen in Fig. 4.3. The effect here is demonstrated in Fig. 4.10.

It shows the same distributions as Figs. 4.8(a) and 4.9(b), with the difference that events were selected to have $0° < \phi < 60°$, that is to be within the nominal segment boundaries of segments 2 and 5, instead of requiring a real pulse in segments 2 or 5. In Fig. 4.10(a), two clusters of entries appear that were absent in Fig. 4.8(a): one is located at $0° < \phi < 10°$ and large negative α_{lr} and consists of events with the real pulse in segments 1 or 4; the other one is located at $50° < \phi < 60°$ and large positive α_{lr} and consists of events with the real pulse in segments 3 or 6. The existence of these events is due to the transversal anisotropy, which causes the deflection of the hole and electron drift trajectories away from the crystal axis <110>. This effect is demonstrated in Fig. 3.3. With the axis <110> at $\phi = 32°$, the charge carriers in segments 2 and 5 are driven to the outside. Close to a boundary, it is possible that the hole, drifting to the outer surface, crosses the geometrical boundary and is collected by the electrode of the neighboring segment. In this case, α_{lr} has to be calculated from the mirror pulses of this neighboring segment's left and right neighbors. The effect is larger for energy depositions at small r, where the distance traveled by the holes is longer and thus the influence of the transversal anisotropy is larger. The effective volume of a segment is thus determined by the relative position of its segment boundaries to the crystal axes.

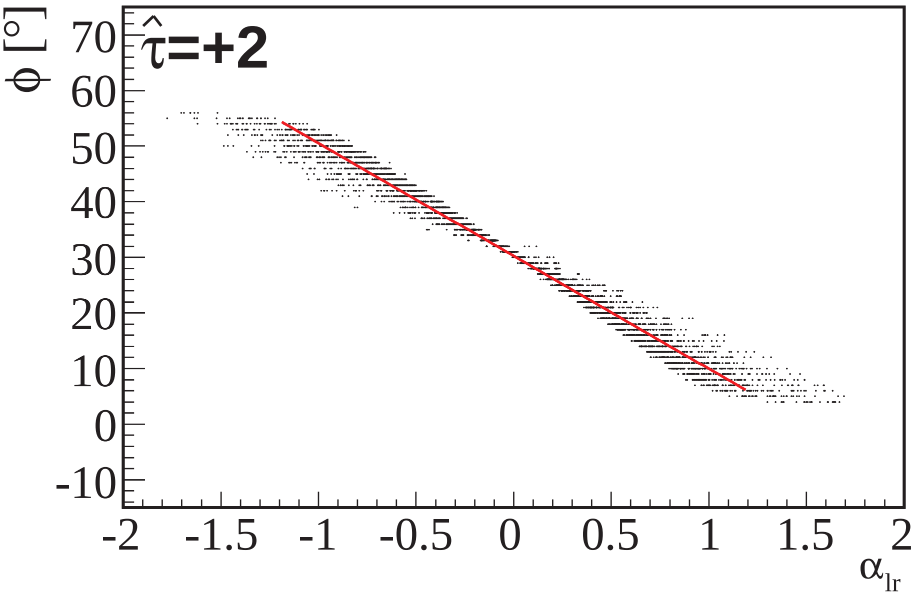

(a)

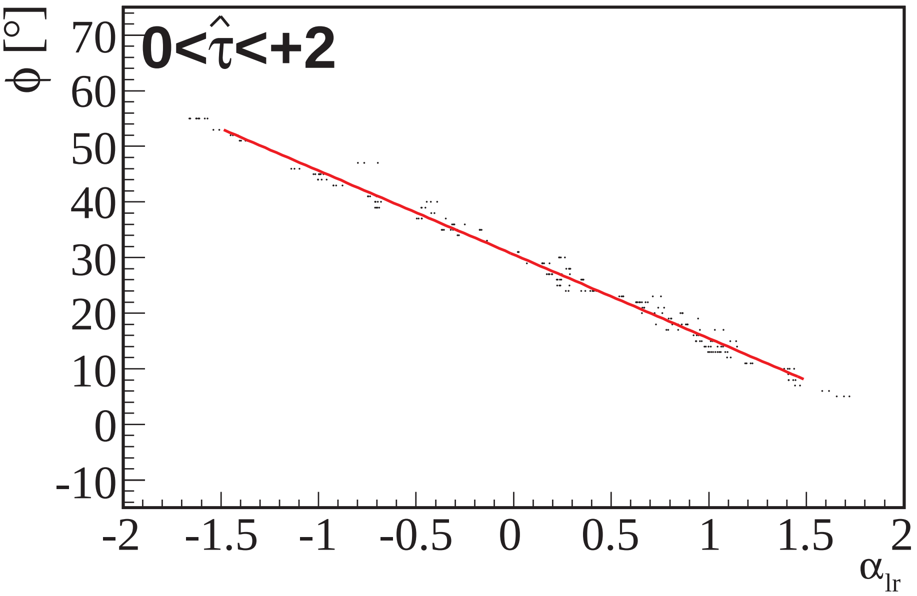

(b)

Figure 4.8: Correlation between ϕ and α_{lr} for events in category (a) I_ϕ ($\hat{\tau}_{lr} = +2$) and (b) II_ϕ ($0 < \hat{\tau}_{lr} < +2$). Each symbol represents one event. Events were simulated at $z = 0$ mm, 6 mm, 10 mm, 14 mm, 20 mm, 26 mm, and 32 mm and selected to fall into segments 2 or 5. Also shown are linear fits. The fit results are listed in Tables 4.2 and 4.3.

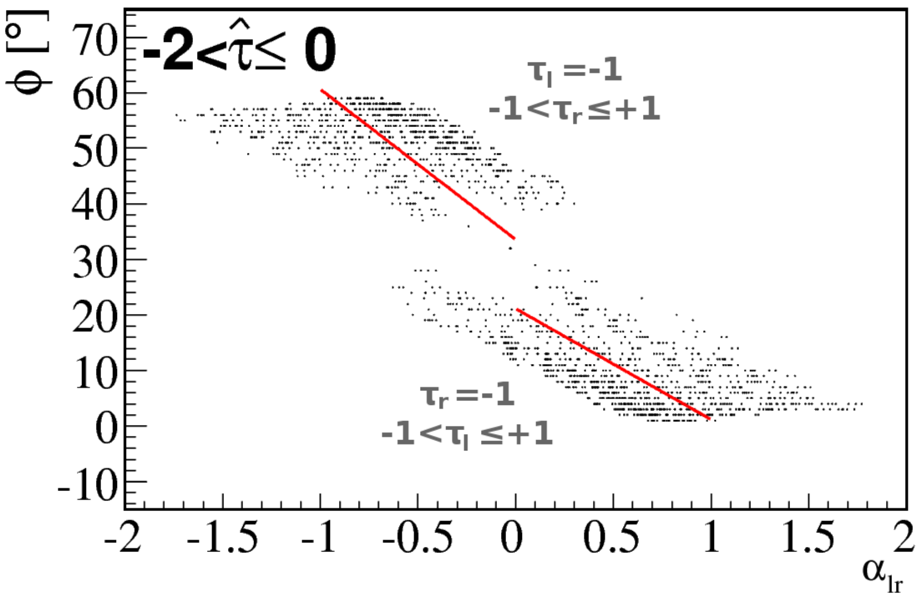

(a)

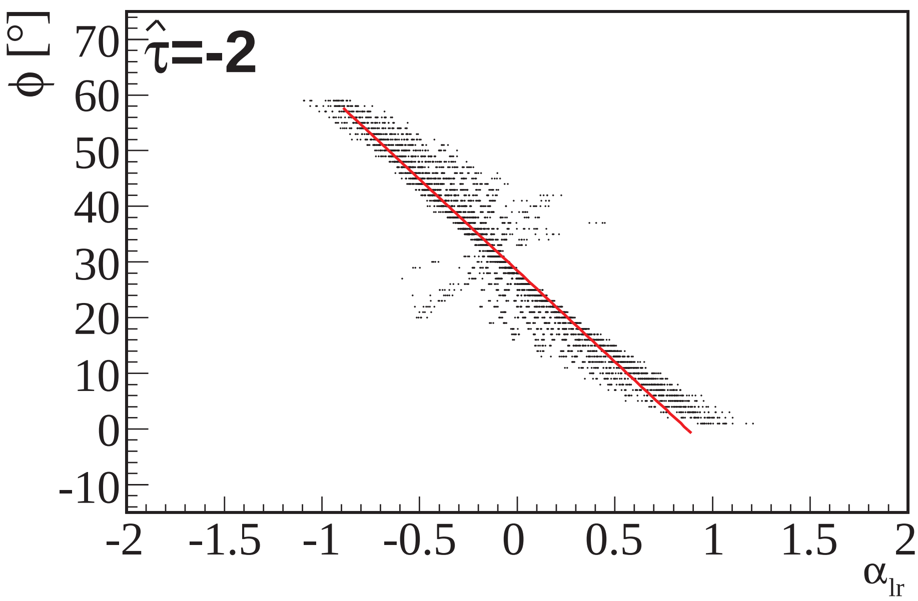

(b)

Figure 4.9: Correlation between ϕ and α_{lr} for events in category (a) IIIa$_\phi$ and IIIb$_\phi$ ($-2 < \hat{\tau}_{lr} \leq 0$) and (b) IV$_\phi$ ($\hat{\tau}_{lr} = -2$). Each symbol represents one event. Events were simulated at $z = 0$ mm, 6 mm, 10 mm, 14 mm, 20 mm, 26 mm, and 32 mm and selected to fall into segments 2 or 5. Also shown are linear fits. The fit results are listed in Tables 4.2 and 4.3.

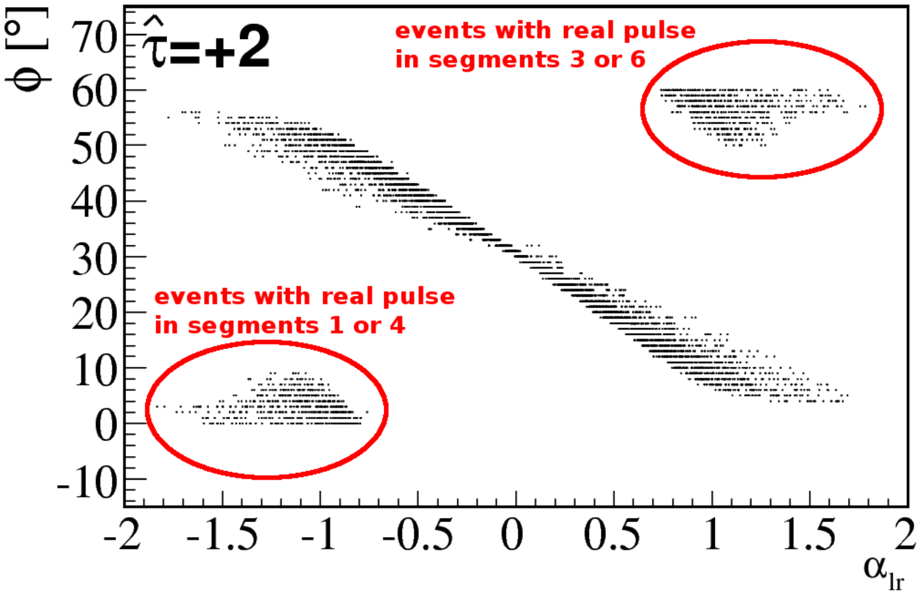

(a)

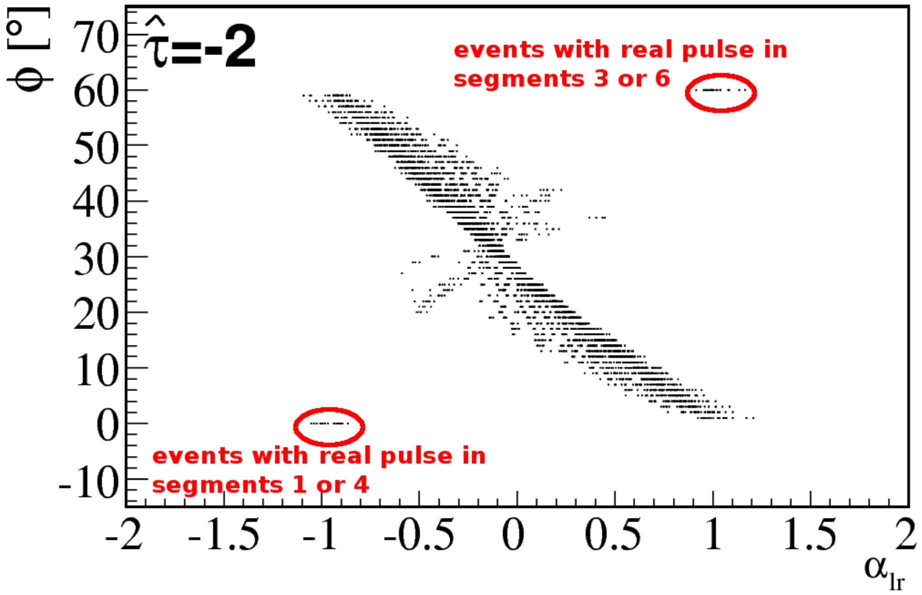

(b)

Figure 4.10: Correlation between ϕ and α_{lr} for events in category (a) I_ϕ ($\hat{\tau}_{lr} = +2$) and (b) IV_ϕ ($\hat{\tau}_{lr} = -2$). Each symbol represents one event. Events were simulated at $z = 0$ mm, 6 mm, 10 mm, 14 mm, 20 mm, 26 mm, and 32 mm and selected to have $0° \leqslant \phi \leqslant 60°$. Events with the real pulse in segments 3 or 6 and with the real pulse in segments 1 or 4 are encircled.

The bands in Figs. 4.8 and 4.9 are relatively wide and seem to be overlays of bands with different slopes. Figure 4.11 compares the situation for the segment center at $z = 0$ mm and close to the upper segment boundary at $z = 10$ mm. Events were selected to be in category I_ϕ and to have the real pulse in segment 5.

The structure of the band does not change close to the segment boundary. This is true also for events in categories II_ϕ, IIIa_ϕ, IIIb_ϕ, and IV_ϕ. Table 4.1 gives the fit results for the different z for events selected to fall into segments 2 or 5. The uncertainties listed are statistical only. Although some variations occur, there is no significant z dependence that could explain the width of the bands in Figs. 4.8 and 4.9. From here on, the events are not separated in z. Differences for different z enter the systematic uncertainties.

In Appendix A, the correlation between ϕ and α_{lr} is given for different sets of segments covering the same ϕ range. For all five categories of $\hat{\tau}_{lr}$, the bands look very similar to the ones for segments 2 and 5, shown in Figs. 4.8 and 4.9. These segments are thus representative.

The nominal segment size is 60° and the crystal axes in the $r\phi$-plane, <110> and <100>, have a 90° degeneracy. Therefore, the simulations in the $r\phi$-plane show a 180° azimuthal symmetry. In the following discussion, segments are grouped according to their position in ϕ, i.e. into 2 and 5, 3 and 6, and 16 and 13. The results for these six segments can be applied to all remaining segments due to the ϕ- and z-symmetries.

The structure of the correlation between ϕ and α_{lr} is examined in detail for events that are selected to fall into segments 2 and 5. This is done to understand and extract the systematic uncertainties on the position reconstruction in ϕ. The correlations are analyzed separately for the different categories of $\hat{\tau}_{lr}$ and are shown in Figs. 4.12 and 4.13. The corresponding correlations for segments 3 and 6, and segments 16 and 13 are shown in Appendix A. In all cases, the correlation can be described using Equation (4.1). The fit results are reported in Tables 4.2 and 4.3.

I_ϕ ($\hat{\tau}_{lr} = +2$) The flattest-slope border of the band in Fig. 4.12(a) is formed by events with $r = 18\,\mathrm{mm} - 22\,\mathrm{mm}$, that is by events in which energy was deposited at the largest r possible for events in category I_ϕ. It is expected that the steepest-slope border consists of events with interactions at the smallest r, $r = 6\,\mathrm{mm} - 7\,\mathrm{mm}$. This is the case for the correlations in segments 3 and 6, and segments 16 and 13, as can be seen in Figs. A.1(a) and A.3(a) in Appendix A. For events falling into segments 2 or 5, however, the steepest slope is found by selecting events with $r = 10\,\mathrm{mm} - 11\,\mathrm{mm}$. This is due to the fact that the effective volume of segments 2 and 5 is smaller than the effective volume of segments 3, 6, 16, and 13. The inward bend of the band of highest amplitude and thus of the segment border can be seen clearly in Fig.4.3(b) at $\phi \approx 60°$. At $r \approx 10$ mm, this indentation is maximal and the distance between the left and right border of segments 2 and 5 is minimal. Therefore, the fastest change of α_{lr} with ϕ

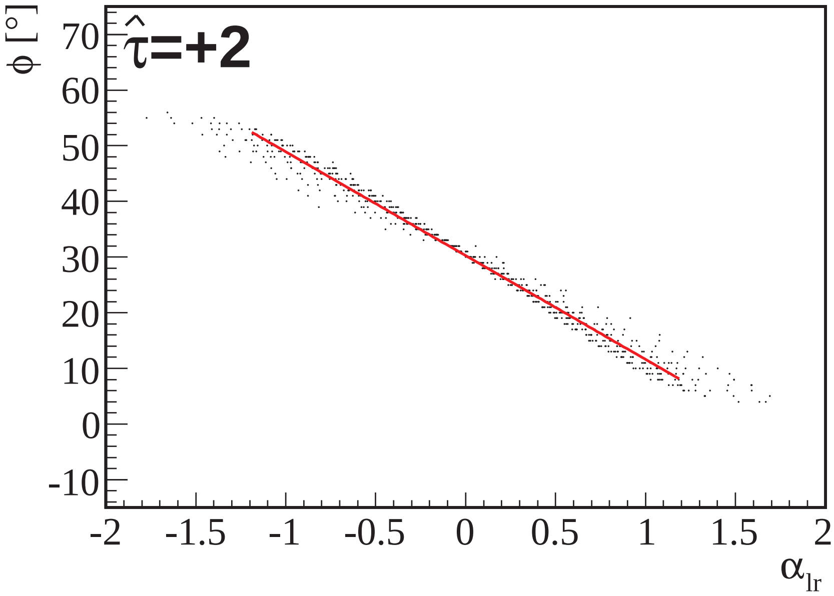

(a)

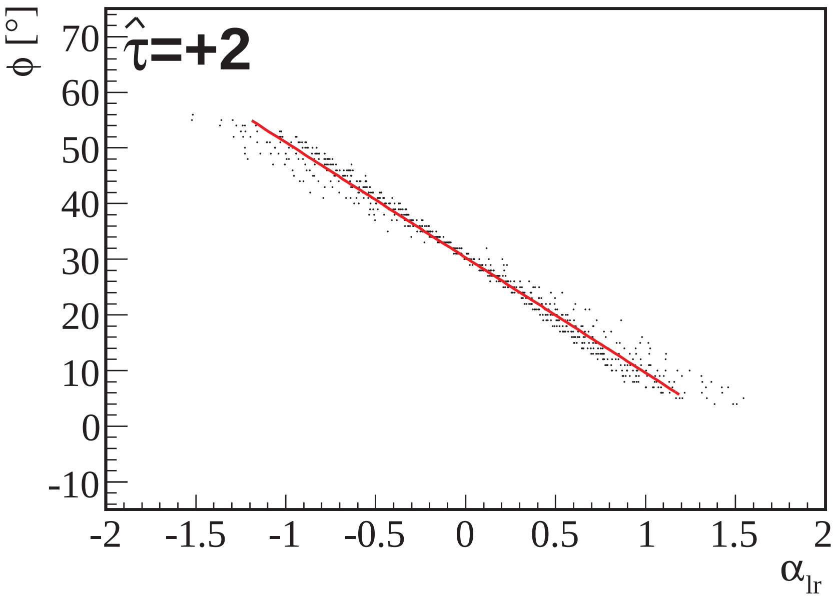

(b)

Figure 4.11: Correlation between ϕ and α_{lr} for events in category I_ϕ ($\hat{\tau}_{lr} = +2$). Events were simulated at (a) $z = 0$ mm and (b) $z = 10$ mm. Each symbol represents one event. Events were selected to fall into segment 5. Also shown are linear fits. The fit results are listed in Table 4.1.

z [mm]	category	s_ϕ [°]	ϕ_0 [°]
0	I_ϕ	-18.6 ± 0.1	30.3 ± 0.1
	II_ϕ	-15.5 ± 0.4	32.1 ± 0.3
	IIIa_ϕ	-26.1 ± 0.3	33.0 ± 0.2
	IIIb_ϕ	-17.6 ± 0.4	20.3 ± 0.2
	IV_ϕ	-30.6 ± 0.1	28.5 ± 0.1
6	I_ϕ	-19.2 ± 0.1	30.3 ± 0.1
	II_ϕ	-15.8 ± 0.4	32.0 ± 0.3
	IIIa_ϕ	-26.4 ± 0.4	33.7 ± 0.2
	IIIb_ϕ	-19.6 ± 0.3	21.5 ± 0.2
	IV_ϕ	-31.4 ± 0.1	28.5 ± 0.1
10	I_ϕ	-20.7 ± 0.1	30.3 ± 0.1
	II_ϕ	-17.8 ± 0.6	31.7 ± 0.3
	IIIa_ϕ	-23.6 ± 0.4	35.7 ± 0.2
	IIIb_ϕ	-18.4 ± 0.3	20.7 ± 0.2
	IV_ϕ	-33.6 ± 0.1	28.5 ± 0.1
14	I_ϕ	-20.9 ± 0.1	30.2 ± 0.1
	II_ϕ	-15.2 ± 0.2	30.3 ± 0.2
	IIIa_ϕ	-30.1 ± 0.4	32.4 ± 0.2
	IIIb_ϕ	-21.1 ± 0.4	21.7 ± 0.2
	IV_ϕ	-33.8 ± 0.1	28.5 ± 0.1
20	I_ϕ	-20.6 ± 0.1	30.2 ± 0.1
	II_ϕ	-14.7 ± 0.2	30.3 ± 0.2
	IIIa_ϕ	-28.1 ± 0.4	33.4 ± 0.2
	IIIb_ϕ	-20.2 ± 0.4	20.8 ± 0.2
	IV_ϕ	-32.8 ± 0.1	28.4 ± 0.1
26	I_ϕ	-20.9 ± 0.1	30.2 ± 0.1
	II_ϕ	-15.0 ± 0.2	30.2 ± 0.1
	IIIa_ϕ	-29.8 ± 0.4	32.5 ± 0.2
	IIIb_ϕ	-21.8 ± 0.4	21.6 ± 0.2
	IV_ϕ	-33.1 ± 0.1	28.4 ± 0.1
32	I_ϕ	-21.3 ± 0.1	30.2 ± 0.1
	II_ϕ	-15.3 ± 0.2	30.2 ± 0.1
	IIIa_ϕ	-26.5 ± 0.4	34.3 ± 0.2
	IIIb_ϕ	-22.4 ± 0.4	21.7 ± 0.2
	IV_ϕ	-33.8 ± 0.1	28.4 ± 0.1

Table 4.1: Results of fitting $s_\phi \cdot \alpha_{lr} + \phi_0$ to α_{lr}-ϕ-distributions for simulations at $z =$ 0 mm, 6 mm, 10 mm, 14 mm, 20 mm, 26 mm, and 32 mm separately. The fit was done separately for category I_ϕ ($\hat{\tau}_{lr} = +2$), II_ϕ ($0 < \hat{\tau}_{lr} < +2$), IIIa_ϕ ($-2 < \hat{\tau}_{lr} \leq 0$ with $\tau_l = -1$), IIIb_ϕ ($-2 < \hat{\tau}_{lr} \leq 0$ with $\tau_r = -1$), and IV_ϕ ($\hat{\tau}_{lr} = -2$). Events were selected to fall into segments 2 or 5.

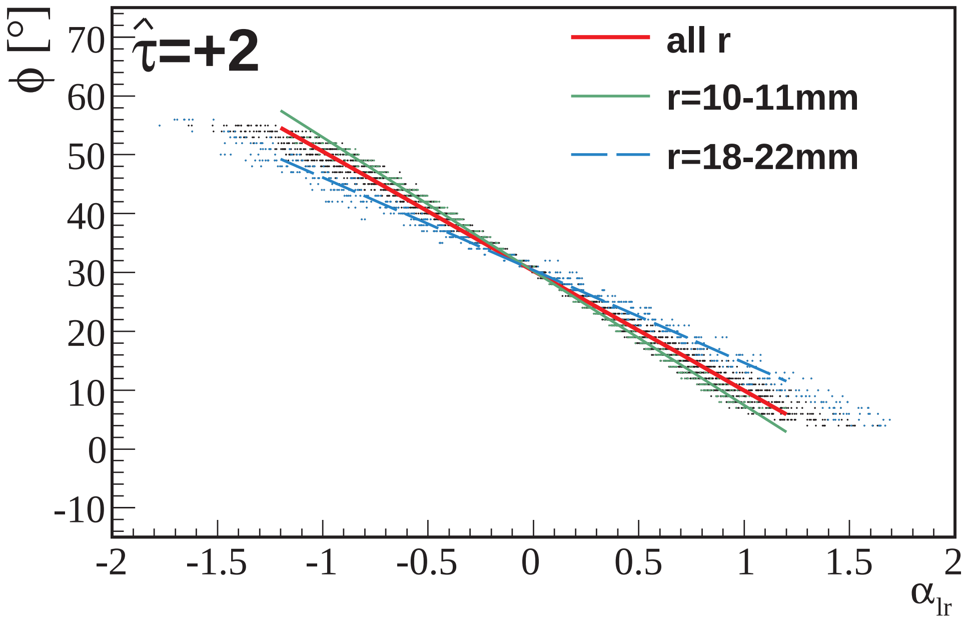

(a)

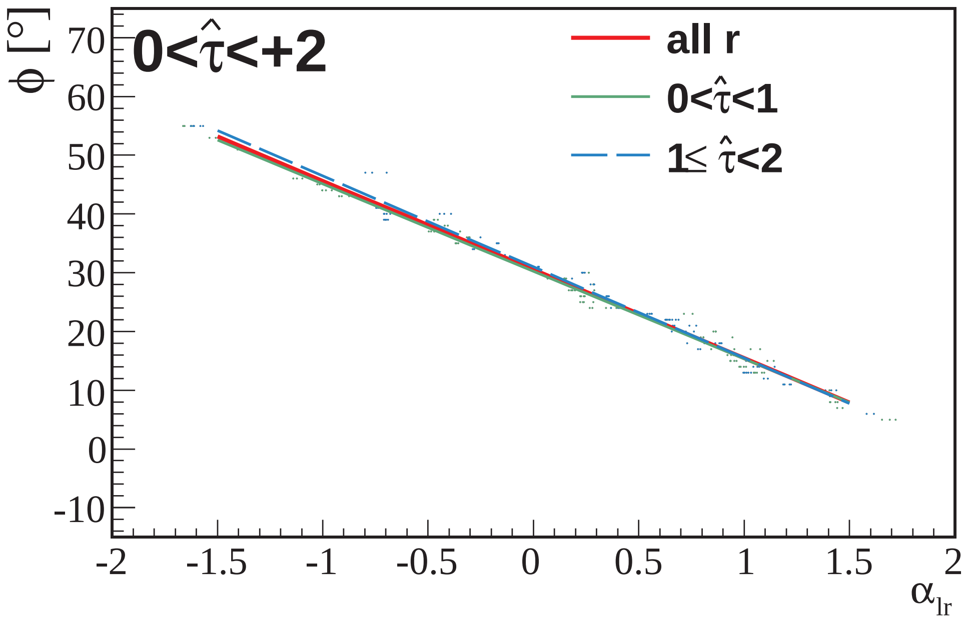

(b)

Figure 4.12: Correlation between ϕ and α_{lr} for events in category (a) I_ϕ ($\hat{\tau}_{lr} = +2$) and (b) II_ϕ ($0 < \hat{\tau}_{lr} < +2$). Each symbol represents one event. Events were simulated at $z = 0$ mm, 6 mm, 10 mm, 14 mm, 20 mm, 26 mm, and 32 mm and selected to fall into segments 2 or 5. Also shown are linear fits to (a) the whole distribution and to events with $r = 10 - 11$ mm and with $r = 18 - 22$ mm separately (b) the whole distribution and to events with $0 < \hat{\tau}_{lr} < 1$ and with $1 \leq \hat{\tau}_{lr} < 2$ separately. The fit results are listed in Tables 4.2 and 4.3.

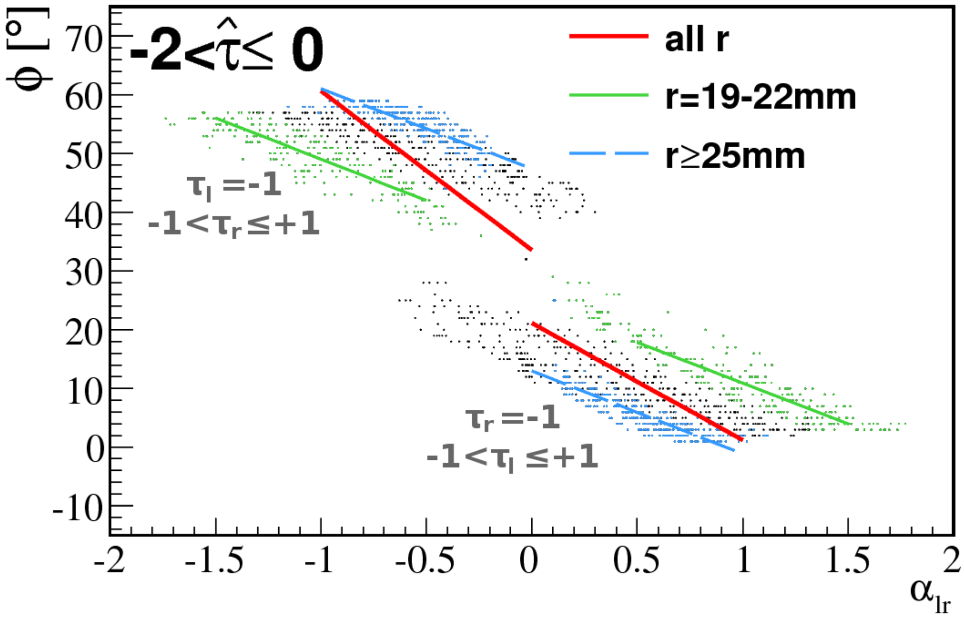

(a)

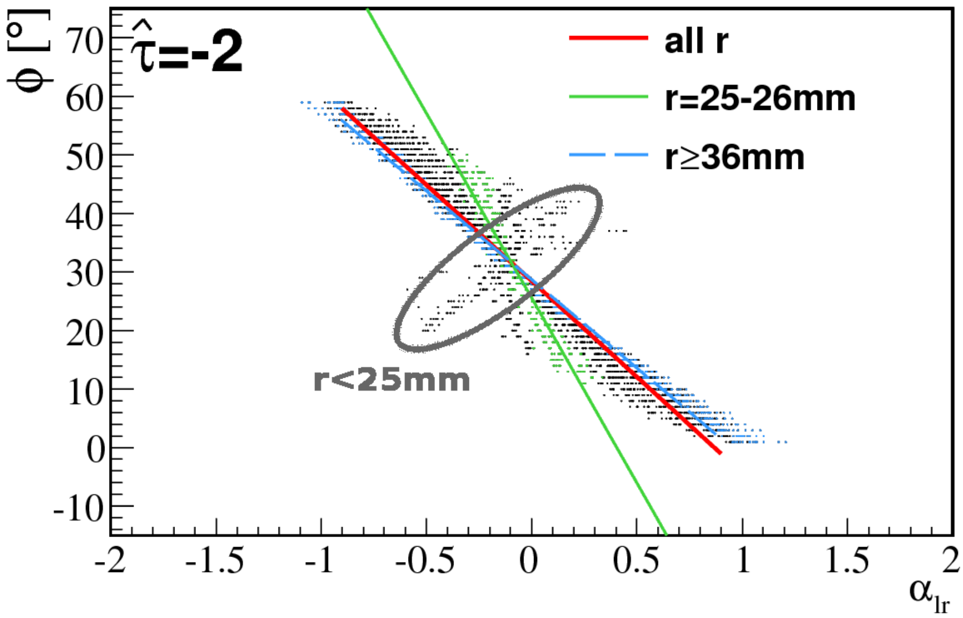

(b)

Figure 4.13: Correlation between ϕ and α_{lr} for events in category (a) IIIa$_\phi$ and IIIb$_\phi$ ($-2 < \hat{\tau}_{lr} \leq 0$) and (b) IV$_\phi$ ($\hat{\tau}_{lr} = -2$). Each symbol represents one event. Events were simulated at $z = 0$ mm, 6 mm, 10 mm, 14 mm, 20 mm, 26 mm, and 32 mm and selected to fall into segments 2 or 5. Also shown are linear fits to (a) the whole distribution and to events with $r = 19 - 22$ mm and with $r \geq 25$ mm separately (b) the whole distribution and to events with $r = 25 - 26$ mm and with $r \geq 36$ mm separately. The fit results are listed in Tables 4.2 and 4.3. In (b), events with $r < 25$ mm are encircled.

happens in this region. For segments 3, 6, 16, and 13, there is no such inward bend but rather an outward bend of the band of highest amplitude. The smallest distance between the segment boundaries is located at $r = 6\,\mathrm{mm} - 7\,\mathrm{mm}$. The systematical uncertainties of the fit to the full band are derived from fits to the steepest- and flattest-slope borders. For segments 3 and 6 and segments 16 and 13, the systematical uncertainties are much larger.

II_ϕ ($0 < \hat{\tau}_{lr} < +2$) The events cover only a small range in r and the band is rather narrow. Two groups of events can be distinguished by separating events with $0 < \hat{\tau}_{lr} < +1$ from events with $+1 \leq \hat{\tau}_{lr} < +2$. To determine the systematical uncertainty of the fit describing the correlation between ϕ and α_{lr} for all events, straight lines are fitted to these two groups of events.

IIIa_ϕ and IIIb_ϕ ($-2 < \hat{\tau}_{lr} \leq 0$) The events separate into the two categories IIIa_ϕ at $30^\circ < \phi < 60^\circ$ and mainly $\alpha_{lr} < 0$ and IIIb_ϕ at $0^\circ < \phi < 30^\circ$ and mainly $\alpha_{lr} > 0$. The bands formed by both categories are very wide. In the case of category IIIa_ϕ, events with the smallest possible r for this event type, $r = 19\,\mathrm{mm} - 22\,\mathrm{mm}$, form the left border, while the interactions leading to the events in the right border have the largest r possible, $r \geq 25\,\mathrm{mm}$. The opposite is the case for category IIIb_ϕ. The parameters describing the linear correlation between ϕ and α_{lr} for all events are determined separately for the two categories. The systematical uncertainties are deduced from fits to events with $r = 19\,\mathrm{mm} - 22\,\mathrm{mm}$ and $r \geq 25\,\mathrm{mm}$, respectively.

IV_ϕ ($\hat{\tau}_{lr} = -2$) Similar to the case of category I_ϕ, the flattest-slope border is formed by events at the largest r, $r \geq 36\,\mathrm{mm}$. The steepest slope border is formed by events with $r = 25\,\mathrm{mm} - 26\,\mathrm{mm}$. There are, however, events in category IV_ϕ with $r < 25\,\mathrm{mm}$ that have a completely different correlation. The method to reconstruct the position breaks down for these events. They are marked with a circle in Fig. 4.13(b).

If α_{lr} and $\hat{\tau}_{lr}$ are known for a single segment event and a single energy deposition is assumed, Equation (4.1) and the parameters in Tables 4.2 and 4.3 allow to reconstruct the azimuth angle of the interaction. The parameters were determined for three groups of segments using the segment pairs as described before.

The position in ϕ of the energy deposition was reconstructed for all simulated events. The deviation of the reconstructed position, ϕ_{rec}, from the true position, ϕ_{true}, $\Delta\phi$, was calculated as

$$\Delta\phi = (\phi_{\mathrm{true}} - \phi_{\mathrm{rec}}) \cdot r, \tag{4.2}$$

where r is the true radial position and ϕ_{true}, ϕ_{rec} are expressed in rad. The distributions of $\Delta\phi$ for events in all five categories of $\hat{\tau}_{lr}$ are depicted in Fig. 4.14. They are normalized to the total number of events for each case.

For events in categories I_ϕ, II_ϕ, and IV_ϕ, the $\Delta\phi$-distributions are centered around $\Delta\phi = 0$. A Gaussian function is fitted to each distribution to determine the resolution of the position reconstruction, σ_ϕ. The results are listed in Table 4.4. The

segments	category	s_ϕ [°]	Δs_ϕ [°] (stat.)	Δs_ϕ [°] (syst.)
2,5	I_ϕ	−20.3	0.1	$^{+4.6}_{-2.4}$
	II_ϕ	−15.1	0.1	$^{+0.2}_{-0.4}$
	IIIa_ϕ	−27.1	0.1	$^{+13.5}_{-0.0}$
	IIIb_ϕ	−20.0	0.1	$^{+6.1}_{-0.0}$
	IV_ϕ	−32.8	0.1	$^{+2.6}_{-30.3}$
3,6	I_ϕ	−29.7	0.1	$^{+10.3}_{-8.3}$
	II_ϕ	−18.6	0.1	$^{+0.0}_{-1.0}$
	IIIa_ϕ	−21.0	0.1	$^{+9.8}_{-0.0}$
	IIIb_ϕ	−23.9	0.1	$^{+11.2}_{-0.0}$
	IV_ϕ	−32.9	0.1	$^{+3.7}_{-17.7}$
16,13	I_ϕ	−29.1	0.1	$^{+10.4}_{-7.4}$
	II_ϕ	−18.1	0.1	$^{+0.0}_{-0.1}$
	IIIa_ϕ	−24.8	0.1	$^{+11.2}_{-0.0}$
	IIIb_ϕ	−26.3	0.1	$^{+15.3}_{-0.0}$
	IV_ϕ	−38.8	0.1	$^{+3.2}_{-38.9}$

Table 4.2: Results on s_ϕ of fitting $s_\phi \cdot \alpha_{lr} + \phi_0$ to α_{lr}-ϕ-distributions for three pairs of segments for simulations at $z = 0$ mm, 6 mm, 10 mm, 14 mm, 20 mm, 26 mm, and 32 mm. The fit was done separately for category I_ϕ ($\hat{\tau}_{lr} = +2$), II_ϕ ($0 < \hat{\tau}_{lr} < +2$), IIIa_ϕ ($-2 < \hat{\tau}_{lr} \leq 0$ with $\tau_l = -1$), IIIb_ϕ ($-2 < \hat{\tau}_{lr} \leq 0$ with $\tau_r = -1$), and IV_ϕ ($\hat{\tau}_{lr} = -2$). Statistical and systematical uncertainties are given.

segments	category	ϕ_0[°]	$\Delta\phi_0$[°] (stat.)	$\Delta\phi_0$[°] (syst.)
2,5	I_ϕ	30.2	0.1	$^{+0.2}_{-0.0}$
	II_ϕ	30.6	0.1	$^{+0.4}_{-0.4}$
	IIIa_ϕ	33.6	0.1	$^{+13.8}_{-0.0}$
	IIIb_ϕ	21.1	0.1	$^{+3.7}_{-8.1}$
	IV_ϕ	28.5	0.1	$^{+0.2}_{-3.0}$
3,6	I_ϕ	91.2	0.1	$^{+1.2}_{-0.0}$
	II_ϕ	90.7	0.1	$^{+1.8}_{-0.5}$
	IIIa_ϕ	100.0	0.1	$^{+9.8}_{-3.5}$
	IIIb_ϕ	81.5	0.1	$^{+3.1}_{-11.0}$
	IV_ϕ	91.3	0.1	$^{+1.3}_{-0.2}$
16,13	I_ϕ	148.3	0.1	$^{+0.0}_{-1.4}$
	II_ϕ	148.8	0.1	$^{+0.2}_{-0.2}$
	IIIa_ϕ	157.4	0.1	$^{+12.0}_{-0.3}$
	IIIb_ϕ	143.8	0.1	$^{+0.7}_{-14.2}$
	IV_ϕ	150.2	0.1	$^{+0.4}_{-0.0}$

Table 4.3: Results on ϕ_0 of fitting $s_\phi \cdot \alpha_{lr} + \phi_0$ to α_{lr}-ϕ-distributions for three pairs of segments for simulations at $z = 0$ mm, 6 mm, 10 mm, 14 mm, 20 mm, 26 mm, and 32 mm. The fit was done separately for category I_ϕ ($\hat{\tau}_{lr} = +2$), II_ϕ ($0 < \hat{\tau}_{lr} < +2$), IIIa_ϕ ($-2 < \hat{\tau}_{lr} \leq 0$ with $\tau_l = -1$), IIIb_ϕ ($-2 < \hat{\tau}_{lr} \leq 0$ with $\tau_r = -1$), and IV_ϕ ($\hat{\tau}_{lr} = -2$). Statistical and systematical uncertainties are given.

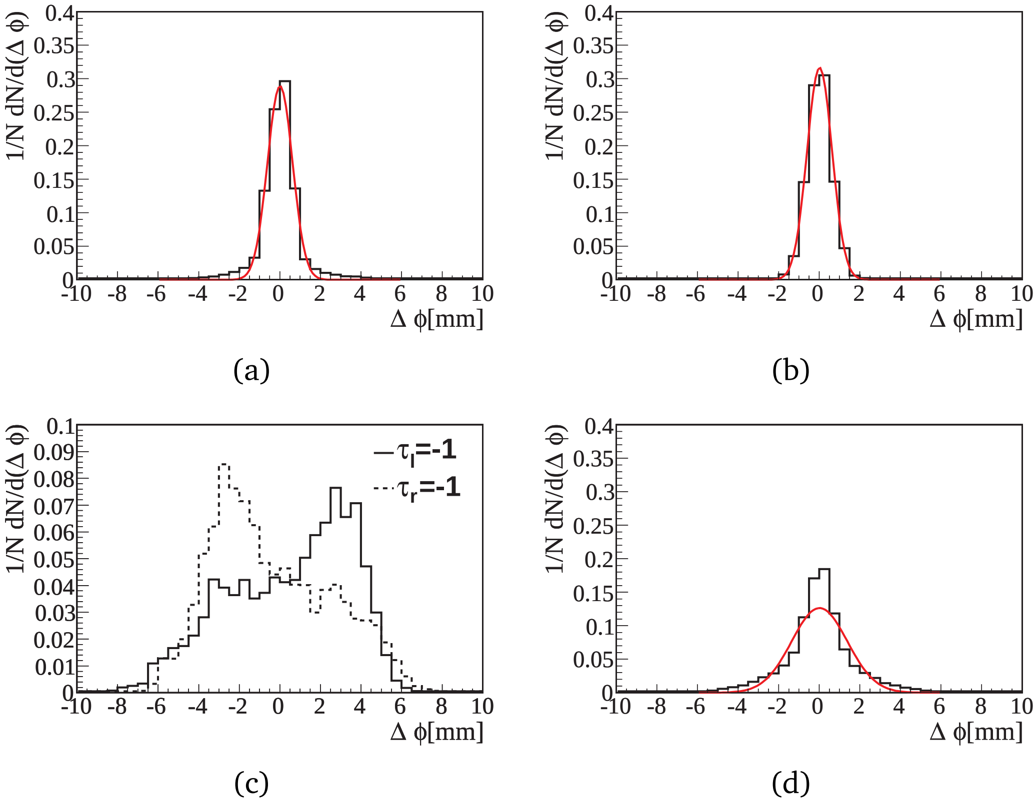

Figure 4.14: Distribution of $\Delta\phi$ for events in category (a) I_ϕ ($\hat{\tau}_{lr} = +2$), (b) II_ϕ ($0 < \hat{\tau}_{lr} < +2$), (c) IIIa_ϕ and IIIb_ϕ ($-2 < \hat{\tau}_{lr} \leq 0$), (d) IV_ϕ ($\hat{\tau}_{lr} = -2$). Events were simulated at $z = 0\,\mathrm{mm}$, $6\,\mathrm{mm}$, $10\,\mathrm{mm}$, $14\,\mathrm{mm}$, $20\,\mathrm{mm}$, $26\,\mathrm{mm}$ and $32\,\mathrm{mm}$. The distributions are normalized to the total number of events in each case. In (a), (b), (d), fits to a Gaussian function are shown.

resolution is dominated by the systematical uncertainties on s_ϕ and ϕ_0. For categories I_ϕ and IV_ϕ, all events with $\alpha_{lr} > 0$ and $\phi < \phi_{\mathrm{fit}}$ and $\alpha_{lr} < 0$ and $\phi > \phi_{\mathrm{fit}}$ in Figs. 4.12(a), A.1(a), A.3(a), and Figs. 4.13(b), A.2(b), A.4(b), respectively, are reconstructed too close to the segment center. For category IV_ϕ, this is the case for the majority of the events. The extent of the effect varies with the relative position of the segment boundaries to the crystal axes.

category	$\sigma_\phi\,[\mathrm{mm}]$
I_ϕ	0.62 ± 0.01
II_ϕ	0.62 ± 0.01
IV_ϕ	1.37 ± 0.01

Table 4.4: Results of fitting a Gaussian function to the $\Delta\phi$-distribution for simulations at $z = 0\,\mathrm{mm}$, $6\,\mathrm{mm}$, $10\,\mathrm{mm}$, $14\,\mathrm{mm}$, $20\,\mathrm{mm}$, $26\,\mathrm{mm}$ and $32\,\mathrm{mm}$. The fit was done separately for category I_ϕ ($\hat{\tau}_{lr} = +2$), II_ϕ ($0 < \hat{\tau}_{lr} < +2$), and IV_ϕ ($\hat{\tau}_{lr} = -2$).

For categories IIIa_ϕ and IIIb_ϕ, the bands of the correlation between ϕ and α_{lr} are much broader than in the other cases. As a consequence, $\Delta\phi$ is much larger. The distributions of $\Delta\phi$ are shown separately for events in categories IIIa$_\phi$ and IIIb$_\phi$ in Fig. 4.14(c). Neither distribution is centered around $\Delta\phi = 0$ and both show peaks at $|\Delta\phi| \approx 3$ mm. These peaks can be associated with events at certain r.

Figure 4.15(a) shows the dependence of $\Delta\phi$ on r for events in category IIIa$_\phi$. Events with $r \leq 20$ mm are located at $\Delta\phi \approx -6$ mm, implying that ϕ_{rec} was overestimated compared to ϕ_{true}. The absolute value of $\Delta\phi$ decreases with increasing r until $r \approx 23$ mm, where $\Delta\phi \approx 0$. The distribution for $r > 23$ mm is centered at $\Delta\phi \approx 3$ mm, implying that ϕ_{rec} is underestimated for these events. This behavior is expected from Fig. 4.13(a) and the corresponding correlations in Appendix A.

For events in category IIIb$_\phi$, the distribution is a reflection at $\Delta\phi = 0$. The correlation between $\Delta\phi$ and r for this case is depicted in Fig. 4.15(b).

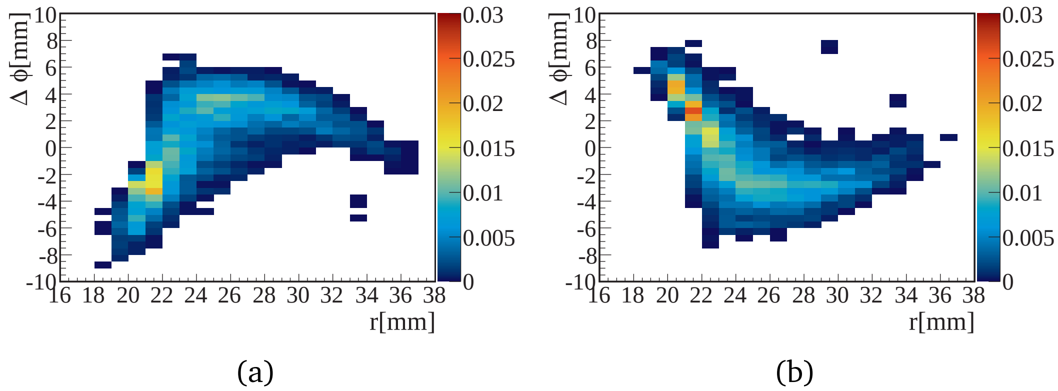

Figure 4.15: Correlation between $\Delta\phi$ and r for events in category (a) IIIa$_\phi$ ($-2 < \hat{\tau}_{lr} \leq 0$ and $\tau_l = -1$), (b) IIIb$_\phi$ ($-2 < \hat{\tau}_{lr} \leq 0$ and $\tau_r = -1$). Events were simulated at $z = 0$ mm, 6 mm, 10 mm, 14 mm, 20 mm, 26 mm and 32 mm. The distributions are normalized to the total number of events in each case.

For categories IIIa$_\phi$ and IIIb$_\phi$, the position reconstruction does not work well. This is not surprising looking at the structure of the mirror pulses. Most events are reconstructed to origin in the center of the segment even if they are located close to the segment boundaries. Fortunately, this affects only $\approx 7\%$ of the volume of the crystal.

4.4.3 Height

For the middle layer, the position in z can be derived from α_{ud}. Interactions were simulated in the rz-plane in steps of $\Delta r = 1$ mm and $\Delta z = 1$ mm. To study possible dependences on ϕ, this was done at $\phi = 0°, 15°, 30°, 45°, 60°, 75°, 90°, 105°, 120°, 135°, 150°$, and $165°$. Due to the $180°$ azimuthal symmetry, it is sufficient to examine the range from $\phi = 0° - 180°$.

Electronics effects, mimicking the situation for DEP events of the 2.6 MeV line of ^{208}Tl, were again added to the pulse shapes. The decay constant was set to $\tau = 50\,\mu$s, the bandwidth-cutoff to 10 MHz, and the noise level to 0.25% of the pulse amplitude.

The impurity density is assumed to be uniform and the crystal axis <001> is aligned to the z-axis. Therefore, the drift trajectories are perpendicular to the z-axis and the nominal segment boundaries at $z \approx \pm 11.7$ mm coincide with the effective segment boundaries.

The correlation between α_{ud} and z is shown in Figs. 4.16 and 4.17 for events from all twelve azimuthal positions. In these and all following figures in this section, $\hat{\tau}$ is used as an abbreviation for $\hat{\tau}_{ud}$. The value of α_{ud} was determined for all events with the real pulse in one of the segments in the middle layer of the detector.

Fits to first-order polynomials,

$$z_{\text{fit}} = s_z \cdot \alpha_{ud} + z_0, \tag{4.3}$$

are also depicted.

To reconstruct the position, the method as described in Sec. 4.4.2 was applied. The fits were performed separately for events in the different categories of $\hat{\tau}_{ud}$. The events with $-2 < \hat{\tau}_{ud} \leq 0$ can be divided into two categories, categories IIIa_z and IIIb_z. The events in category IIIa_z ($\tau_u = -1$ and $-1 < \tau_d \leq +1$) have predominantly $\alpha_{ud} < 0$ and are located at $-11.7\,\text{mm} < z < 0\,\text{mm}$. The events in category IIIb_z ($\tau_d = -1$ and $-1 < \tau_u \leq +1$) have predominantly $\alpha_{ud} > 0$ and are located at $0\,\text{mm} < z < 11.7\,\text{mm}$. In Figs. 4.5(c) and (d), these two groups can be distinguished close to the segment boundaries.

There were no events that did not fall into one of the categories I_z, II_z, IIIa_z, IIIb_z, or IV_z.

To determine the reason for the large width of the bands in Figs. 4.16 and 4.17, the correlation between α_{ud} and z was examined separately for all ϕ. In Fig. 4.18, the correlation is shown for events in category I_z at the left boundary of segment 5 ($\phi = 0°$) and at the center of segment 5 ($\phi = 30°$), close to the crystal axis <110>. The real pulse was required to be in a middle layer segment.

The structure of the two bands is not significantly different. The same holds for events in categories II_z, IIIa_z, IIIb_z, and IV_z. The fit results for all twelve positions in ϕ are reported in Table 4.5. The uncertainties listed are statistical only. No fit was carried out for category II_z, since there were only ≈ 4 events for each ϕ. Although some differences are observed for the different ϕ, there is no significant effect that would warrant a ϕ-dependent z-reconstruction. The observed differences enter the systematic uncertainties.

The structure of the correlation between z and α_{ud} is examined in detail for all events with the real pulse in one of the segments in the middle layer of the detector. This is done to understand and extract the systematic uncertainties on the position reconstruction in z. The five categories of $\hat{\tau}_{ud}$ are analyzed separately. The respective correlations are depicted in Figs. 4.19 and 4.20. Equation (4.3) describes the correlation in all cases. The fit results are listed in Tables 4.6 and 4.7.

I_z ($\hat{\tau}_{ud} = +2$) The flattest-slope border of the distribution is formed by events with $r = 20\,\text{mm} - 22\,\text{mm}$. These are the largest r at which events in category I_z can

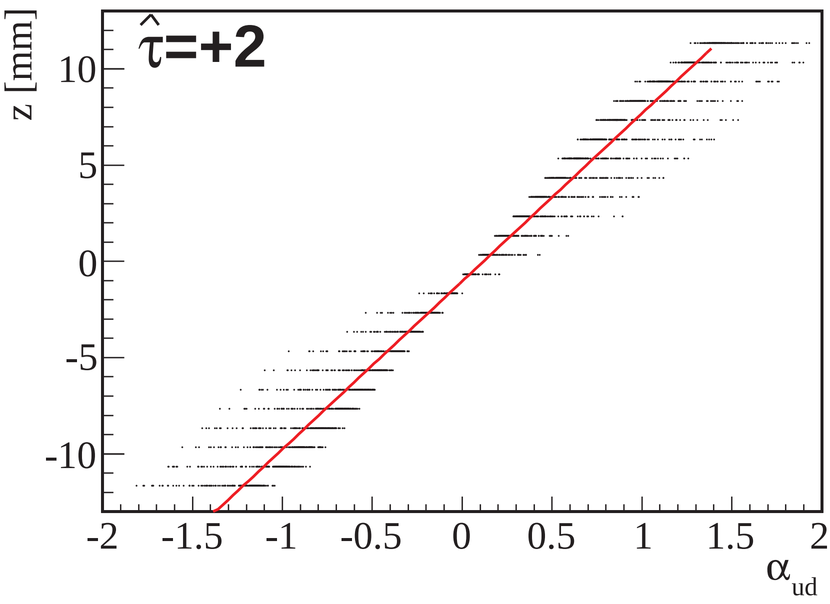

(a)

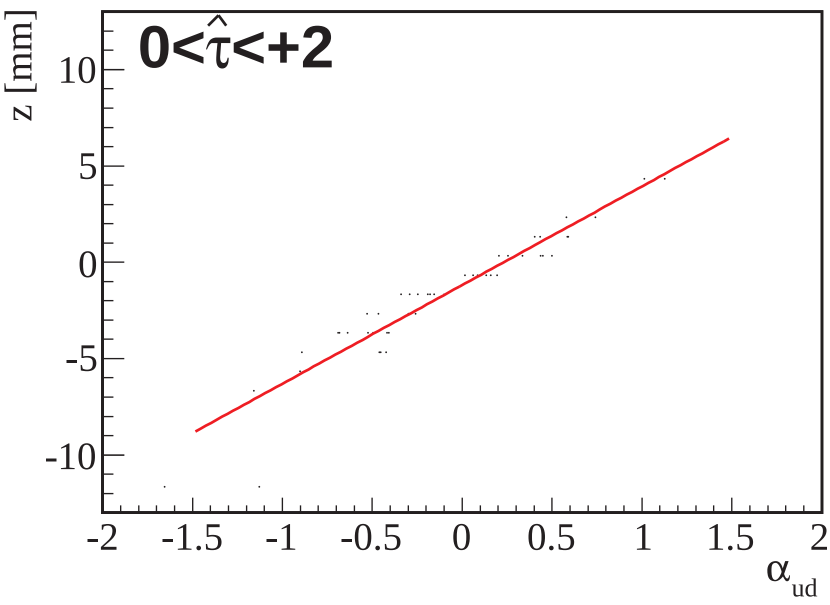

(b)

Figure 4.16: Correlation between z and α_{ud} for events in category (a) I_z ($\hat{\tau}_{ud} = +2$) and (b) II_z ($0 < \hat{\tau}_{ud} < +2$). Each symbol represents one event. Events were simulated at $\phi = 0°, 15°, 30°, 45°, 60°, 75°, 90°, 105°, 120°, 135°, 150°$, and $165°$. Also shown are linear fits. The fit results are listed in Tables 4.6 and 4.7.

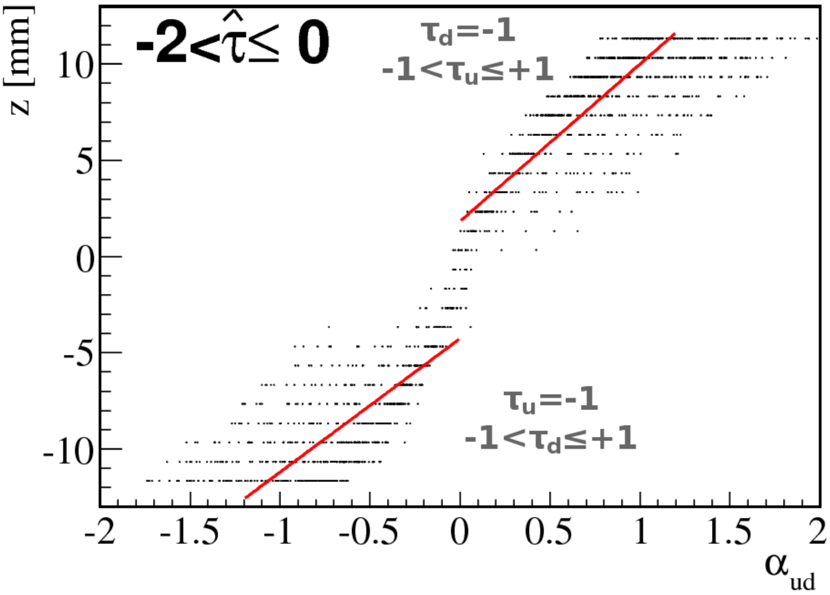

(a)

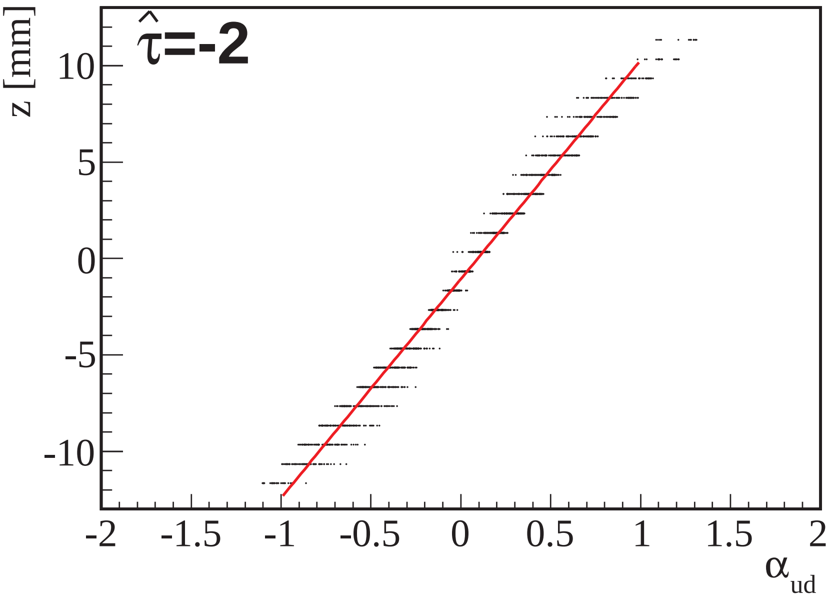

(b)

Figure 4.17: Correlation between z and α_{ud} for events in category (a) IIIa$_z$ and IIIb$_z$ ($-2 < \hat{\tau}_{ud} \leq 0$), and (b) IV$_z$ ($\hat{\tau}_{ud} = -2$). Each symbol represents one event. Events were simulated at $\phi = 0°$, 15°, 30°, 45°, 60°, 75°, 90°, 105°, 120°, 135°, 150°, and 165°. Also shown are linear fits. The fit results are listed in Tables 4.6 and 4.7.

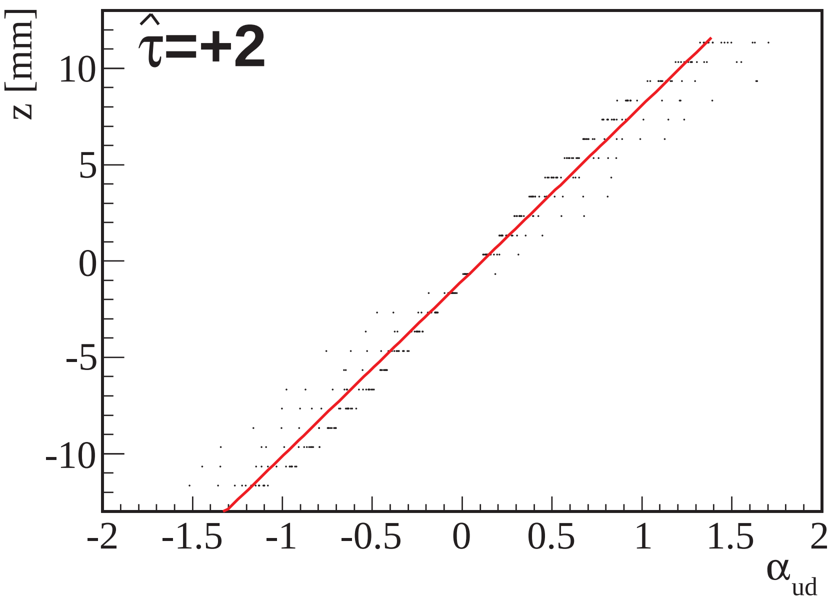

(a)

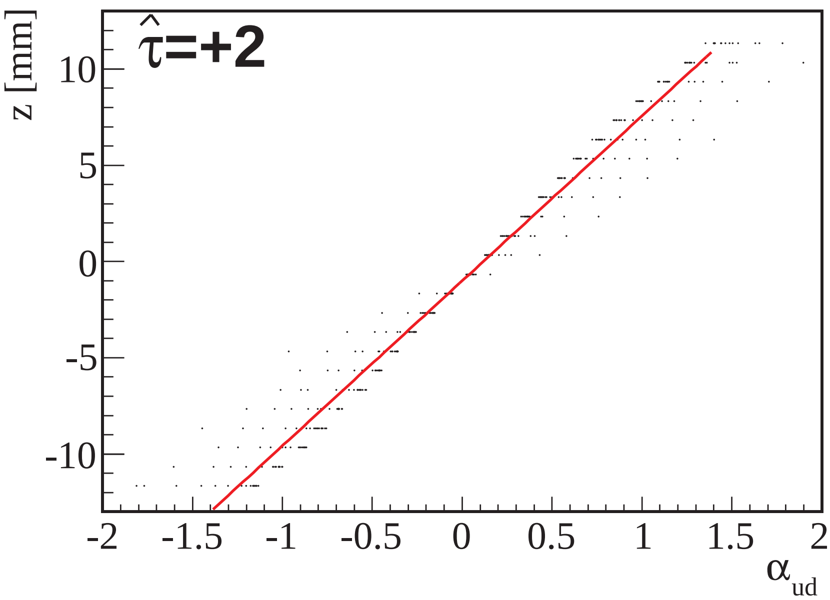

(b)

Figure 4.18: Correlation between z and α_{ud} for events in category I_z ($\hat{\tau}_{ud} = +2$). Events were simulated at (a) $\phi = 0°$ and (b) $\phi = 30°$. Each symbol represents one event. The fit results are listed in Table 4.5.

$\phi\,[^\circ]$	category	$s_z\,[\mathrm{mm}]$	$z_0\,[\mathrm{mm}]$
0	I_z	9.1 ± 0.1	-1.0 ± 0.1
	IIIa_z	6.4 ± 0.6	-5.3 ± 0.4
	IIIb_z	8.6 ± 0.4	2.0 ± 0.3
	IV_z	12.5 ± 0.1	-1.1 ± 0.1
15	I_z	8.7 ± 0.1	-1.0 ± 0.1
	IIIa_z	6.7 ± 0.5	-4.4 ± 0.3
	IIIb_z	7.8 ± 0.4	1.7 ± 0.3
	IV_z	11.1 ± 0.2	-1.1 ± 0.1
30	I_z	8.6 ± 0.1	-1.0 ± 0.1
	IIIa_z	7.2 ± 0.4	-3.8 ± 0.3
	IIIb_z	7.6 ± 0.4	2.2 ± 0.3
	IV_z	10.9 ± 0.1	-1.1 ± 0.1
45	I_z	8.7 ± 0.1	-1.0 ± 0.1
	IIIa_z	6.9 ± 0.4	-4.1 ± 0.3
	IIIb_z	8.1 ± 0.4	1.6 ± 0.3
	IV_z	11.1 ± 0.1	-1.1 ± 0.1
60	I_z	9.0 ± 0.1	-1.1 ± 0.1
	IIIa_z	5.9 ± 0.5	-5.3 ± 0.3
	IIIb_z	9.5 ± 0.4	1.6 ± 0.3
	IV_z	12.4 ± 0.2	-1.1 ± 0.1
75	I_z	8.6 ± 0.1	-1.1 ± 0.1
	IIIa_z	7.4 ± 0.4	-3.9 ± 0.3
	IIIb_z	8.7 ± 0.4	1.3 ± 0.3
	IV_z	11.0 ± 0.2	-1.1 ± 0.1
90	I_z	8.5 ± 0.1	-1.0 ± 0.1
	IIIa_z	7.8 ± 0.4	-3.5 ± 0.3
	IIIb_z	7.3 ± 0.4	2.3 ± 0.3
	IV_z	10.8 ± 0.1	-1.1 ± 0.1
105	I_z	8.5 ± 0.1	-1.1 ± 0.1
	IIIa_z	6.7 ± 0.4	-3.9 ± 0.3
	IIIb_z	7.7 ± 0.4	2.0 ± 0.3
	IV_z	11.1 ± 0.1	-1.1 ± 0.1
120	I_z	9.5 ± 0.1	-1.1 ± 0.1
	IIIa_z	6.8 ± 0.6	-5.2 ± 0.3
	IIIb_z	7.7 ± 0.4	3.2 ± 0.3
	IV_z	12.6 ± 0.2	-1.1 ± 0.1
135	I_z	8.5 ± 0.1	-1.1 ± 0.1
	IIIa_z	6.4 ± 0.5	-4.5 ± 0.3
	IIIb_z	8.6 ± 0.4	1.3 ± 0.3
	IV_z	11.0 ± 0.1	-1.1 ± 0.1
150	I_z	8.5 ± 0.1	-1.0 ± 0.1
	IIIa_z	8.1 ± 0.5	-3.5 ± 0.3
	IIIb_z	8.7 ± 0.4	1.3 ± 0.3
	IV_z	10.8 ± 0.1	-1.1 ± 0.1
165	I_z	8.6 ± 0.1	-1.0 ± 0.1
	IIIa_z	6.7 ± 0.4	-4.2 ± 0.3
	IIIb_z	7.9 ± 0.3	1.7 ± 0.3
	IV_z	11.0 ± 0.1	-1.1 ± 0.1

Table 4.5: Results of fitting $s_z \cdot \alpha_{ud} + z_0$ to α_{ud}-z-distributions for simulations at $\phi = 0^\circ, 15^\circ, 30^\circ, 45^\circ, 60^\circ, 75^\circ, 90^\circ, 105^\circ, 120^\circ, 135^\circ, 150^\circ$, and 165° separately. The fit was done separately for category I_z ($\hat{\tau}_{ud} = +2$), IIIa_z ($-2 < \hat{\tau}_{ud} \leq 0$ with $\tau_u = -1$), IIIb_z ($-2 < \hat{\tau}_{ud} \leq 0$ with $\tau_d = -1$), and IV_z ($\hat{\tau}_{ud} = -2$).

be found. The steepest-slope border is formed by events with interactions at the smallest r, $r = 6\,\mathrm{mm} - 7\,\mathrm{mm}$. To derive the systematical uncertainties, the steepest- and flattest-slope borders are fitted separately.

II_z ($0 < \hat{\tau}_{ud} < +2$) Only very few events fall into category II_z due to the small volume in which these events are possible. The systematical uncertainties are determined by fitting events with $0 < \hat{\tau}_{ud} < +1$ and events with $1 \leq \hat{\tau}_{ud} < +2$ separately.

IIIa_z and IIIb_z ($-2 < \hat{\tau}_{ud} \leq 0$) Two groups of events can be distinguished: events falling into category IIIa_z at $-11.7\,\mathrm{mm} < z < 0\,\mathrm{mm}$ and events falling into category IIIb_z, which are located at $0\,\mathrm{mm} < z < 11.7\,\mathrm{mm}$. In both cases, the bands are very wide. The left border of the first group is formed by events with $r = 21\,\mathrm{mm} - 23\,\mathrm{mm}$. These are slightly larger r than in the case of α_{lr}. The interactions leading to the events in the right border have $r \geq 27\,\mathrm{mm}$, again larger than in the case of α_{lr}. For the other group of events, the left border is formed by events at large r, and the right border by events at the smallest r possible for this type of event. The parameters describing the linear correlation between z and α_{ud} for all events are determined separately for the two groups. The systematical uncertainties are deduced from fits to the left and right border of the distributions, respectively.

IV_z ($\hat{\tau}_{ud} = -2$) Again, the interactions leading to the flattest-slope border are located at the largest r, $r \geq 36\,\mathrm{mm}$. The steepest-slope border is formed by events with $r = 25\,\mathrm{mm} - 28\,\mathrm{mm}$. No events with $r < 25\,\mathrm{mm}$ exist in category IV_z. The break down of the position reconstruction method observed for the case of α_{lr} and ϕ does not happen.

The z-position of a single energy deposition was calculated with Equation (4.3) and the parameters in Tables 4.6 and 4.7 for all simulated events. The deviation, Δz, of the reconstructed position, z_{rec}, from the true position, z_{true},

$$\Delta z = z_{\mathrm{true}} - z_{\mathrm{rec}}, \tag{4.4}$$

was determined. Figure 4.21 shows the distributions of Δz for events in category I_z, II_z, IIIa_z and IIIb_z, and IV_z. They are normalized to the total number of events for each case. A larger binsize was chosen for category II_z due to the small number of events.

For events in categories I_z, II_z, and IV_z, the Δz-distributions are centered around $\Delta z = 0$. The resolution of the position reconstruction is obtained by fitting a Gaussian function to each distribution. The resolution is defined as the width of the Gaussian, σ_z. The results are reported in Table 4.8. The resolution is dominated by the systematical uncertainties on s_z and z_0. Events in category I_z with $|z| < |z_{\mathrm{fit}}|$ in Fig. 4.19(a) are reconstructed too far away from the segment center. This effect is rather large ($\gtrsim 3\,\mathrm{mm}$) for the majority of events. Events in category IV_z, on the other hand, have a larger fraction of events with $|z| > |z_{\mathrm{fit}}|$, as can be seen in Fig. 4.20(b). These events

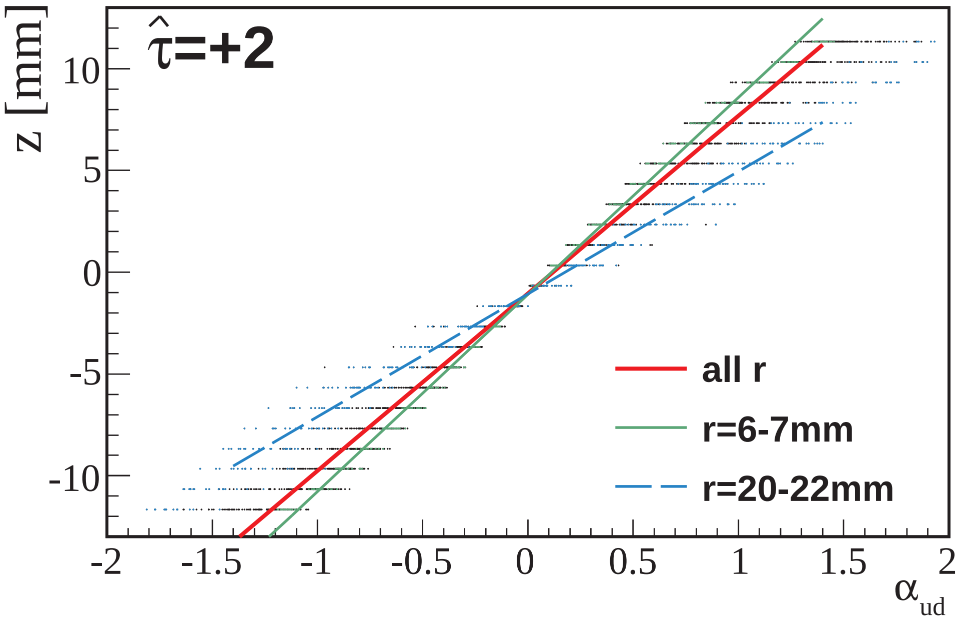

(a)

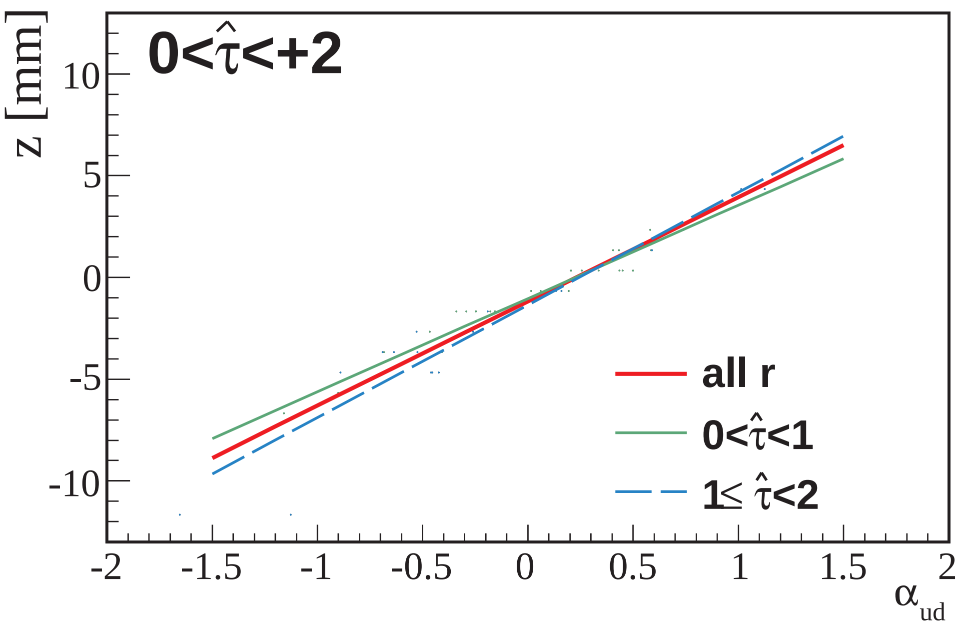

(b)

Figure 4.19: Correlation between z and α_{ud} for events in category (a) I_z ($\hat{\tau}_{ud} = +2$) and (b) II_z ($0 < \hat{\tau}_{ud} < +2$). Each symbol represents one event. Events were simulated at $\phi = 0°, 15°, 30°, 45°, 60°, 75°, 90°, 105°, 120°, 135°, 150°$, and $165°$. Also shown are linear fits to (a) the whole distribution and to events with $r = 6-7$ mm and with $r = 20-22$ mm separately (b) the whole distribution and to events with $0 < \hat{\tau}_{ud} < 1$ and with $1 \leq \hat{\tau}_{ud} < 2$ separately. The fit results are listed in Tables 4.6 and 4.7.

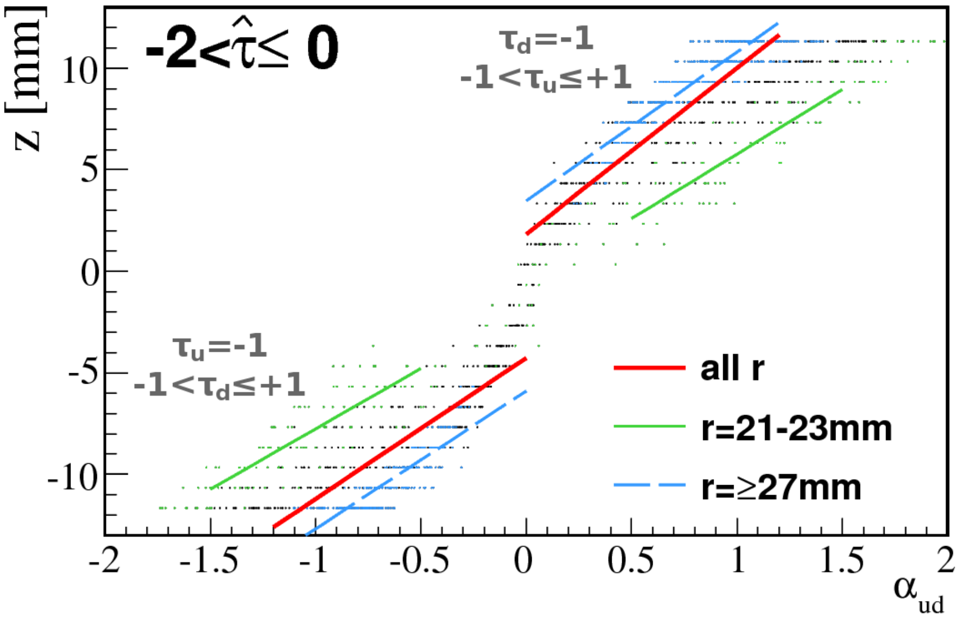

(a)

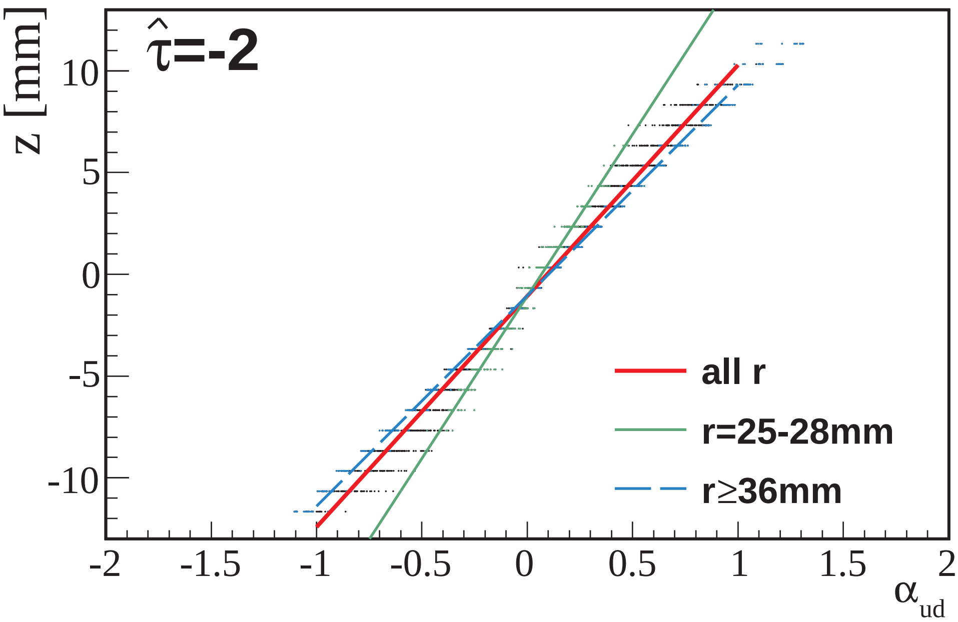

(b)

Figure 4.20: Correlation between z and α_{ud} for events in category (a) IIIa$_z$ and IIIb$_z$ ($-2 < \hat{\tau}_{ud} \leq 0$), and (b) IV$_z$ ($\hat{\tau}_{ud} = -2$). Each symbol represents one event. Events were simulated at $\phi = 0°, 15°, 30°, 45°, 60°, 75°, 90°, 105°, 120°, 135°, 150°$, and $165°$. Also shown are linear fits to (a) the whole distribution and to events with $r = 21 - 23$ mm and with $r \geq 27$ mm separately (b) the whole distribution and to events with $r = 25 - 28$ mm and with $r \geq 36$ mm separately. The fit results are listed in Tables 4.6 and 4.7.

category	s_z [mm]	Δs_z [mm] (stat.)	Δs_z [mm] (syst.)
I_z	8.7	0.1	${}^{+2.7}_{-1.0}$
II_z	5.1	0.3	${}^{+0.4}_{-0.5}$
IIIa_z	6.9	0.1	${}^{+0.0}_{-1.0}$
IIIb_z	8.2	0.1	${}^{+0.0}_{-1.8}$
IV_z	11.4	0.1	${}^{+4.5}_{-1.1}$

Table 4.6: Results on s_z of fitting $s_z \cdot \alpha_{ud} + z_0$ to α_{ud}-z-distributions for simulations at $\phi = 0°, 15°, 30°, 45°, 60°, 75°, 90°, 105°, 120°, 135°, 150°$, and $165°$. The fit was done separately for category I_z ($\hat{\tau}_{ud} = +2$), II_z ($0 < \hat{\tau}_{ud} < +2$), IIIa_z ($-2 < \hat{\tau}_{ud} < 0$ with $\tau_u = -1$), IIIb_z ($-2 < \hat{\tau}_{ud} < 0$ with $\tau_d = -1$), and IV_z ($\hat{\tau}_{ud} = -2$).

category	z_0 [mm]	Δz_0 [mm] (stat.)	Δz_0 [mm] (syst.)
I_z	−1.0	0.1	${}^{+0.0}_{-0.1}$
II_z	−1.2	0.1	${}^{+0.2}_{-0.2}$
IIIa_z	−4.3	0.1	${}^{+2.5}_{-1.6}$
IIIb_z	1.8	0.1	${}^{+1.7}_{-2.4}$
IV_z	−1.1	0.1	${}^{+0.0}_{-0.1}$

Table 4.7: Results on z_0 of fitting $s_z \cdot \alpha_{ud} + z_0$ to α_{ud}-z-distributions for simulations at $\phi = 0°, 15°, 30°, 45°, 60°, 75°, 90°, 105°, 120°, 135°, 150°$, and $165°$. The fit was done separately for category I_z ($\hat{\tau}_{ud} = +2$), II_z ($0 < \hat{\tau}_{ud} < +2$), IIIa_z ($-2 < \hat{\tau}_{ud} < 0$ with $\tau_u = -1$), IIIb_z ($-2 < \hat{\tau}_{ud} < 0$ with $\tau_d = -1$), and IV_z ($\hat{\tau}_{ud} = -2$).

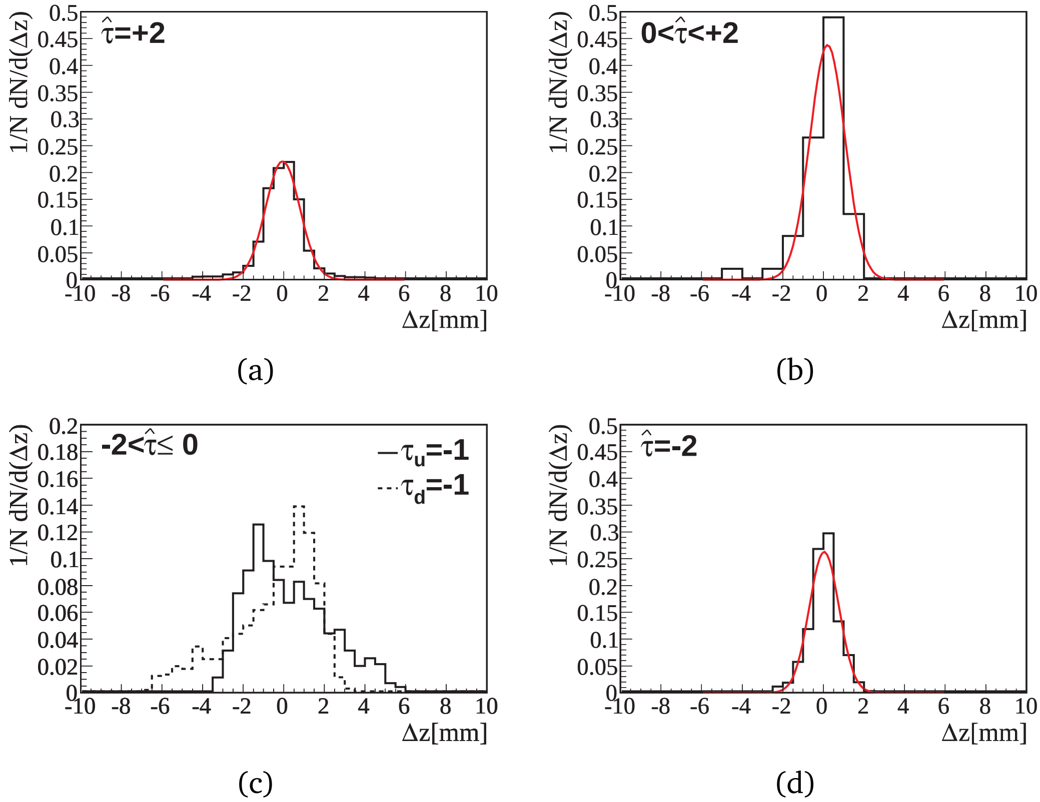

Figure 4.21: Distribution of Δz for events in category (a) I_z ($\hat{\tau}_{ud} = +2$), (b) II_z ($0 < \hat{\tau}_{ud} < +2$), (c) $IIIa_z$ and $IIIb_z$ ($-2 < \hat{\tau}_{ud} \leq 0$), (d) IV_z ($\hat{\tau}_{ud} = -2$). Events were simulated at $\phi = 0°, 15°, 30°, 45°, 60°, 75°, 90°, 105°, 120°, 135°, 150°$, and $165°$. The distributions are normalized to the total number of events in each case. In (a), (b), (d) Gaussian fits are shown. Note the different scale in (c) and the larger binwidth in (b).

category	σ_z [mm]
I_z	0.85 ± 0.01
II_z	0.87 ± 0.16
IV_z	0.73 ± 0.01

Table 4.8: Results of fitting a Gaussian function to the Δz-distribution for simulations at $\phi = 0°, 15°, 30°, 45°, 60°, 75°, 90°, 105°, 120°, 135°, 150°$, and $165°$. The fit was done separately for category I_z ($\hat{\tau}_{ud} = +2$), II_z ($0 < \hat{\tau}_{ud} < +2$), and IV_z ($\hat{\tau}_{ud} = -2$).

are reconstructed too close to the segment center. The effect is less pronounced than the shift away from the segment center for events in category I_z.

As a consequence of the much broader bands of the correlation between z and α_{ud} in categories $IIIa_z$ and $IIIb_z$, Δz can be much larger than in the other cases. The total distribution is a superposition of the distribution for events in category $IIIa_z$ and events in category $IIIb_z$. Each of these subdistributions is not centered around $\Delta z = 0$, but around $|\Delta z| \approx 1\,\text{mm}$. The dependence of Δz on r for category IIIa_z is shown in Fig. 4.22(a). Events with $r \leq 22\,\text{mm}$ appear at $\Delta z \approx 5\,\text{mm}$, implying that $|z_{\text{rec}}|$ was overestimated. With increasing r, Δz decreases. At $r \approx 25\,\text{mm}$, $\Delta z \approx 0$. It increases again until $r \approx 27\,\text{mm}$, where $\Delta z \approx -2$. The distribution for $r > 27\,\text{mm}$ is centered at $\Delta z \approx -1\,\text{mm}$, implying that $|z_{\text{rec}}|$ was underestimated for these events. Figure 4.20(a) anticpated this behavior. For events in category IIIb_z, the distribution is a reflection at $\Delta z = 0$. The corresponding correlation between Δz and r is depicted in Fig. 4.22(b).

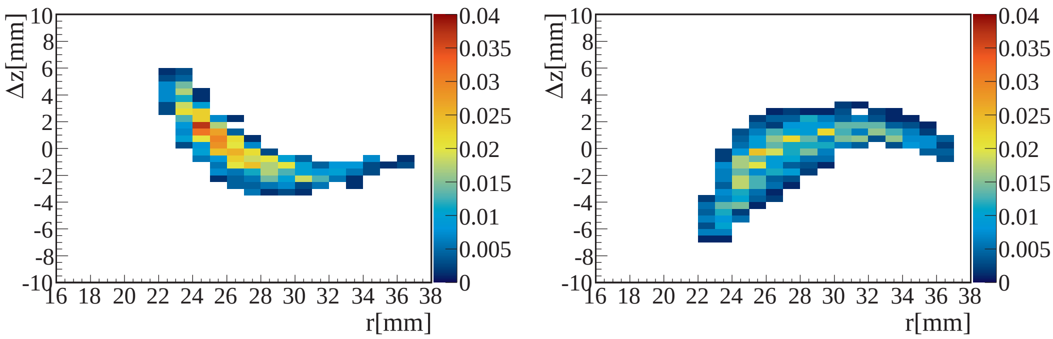

(a) (b)

Figure 4.22: Correlation between Δz and r for events in category (a) IIIa_z ($-2 < \hat{\tau}_{ud} \leq 0$ and $\tau_u = -1$), (b) IIIb_z ($-2 < \hat{\tau}_{ud} \leq 0$ and $\tau_d = -1$). Events were simulated at $\phi = 0°, 15°, 30°, 45°, 60°, 75°, 90°, 105°, 120°, 135°, 150°$, and $165°$. The distributions are normalized to the total number of events in each case.

For categories IIIa_z and IIIb_z, the reconstructed position does not coincide well with the true position, as is expected from the structure of the mirror pulses. Events that are located close to the segment boundaries are reconstructed with a shift towards the segment center.

4.5 Summary on position resolution

A simple linear ansatz using the polarities and asymmetries of mirror pulses results in a position resolution of the order of 1 mm for more than 90% of the volume.

For the reconstruction in ϕ, a systematic shift of the reconstructed position towards the segment center is observed. The extent of the shift depends on the relative position of the segment boundaries to the crystal axes and on $\hat{\tau}_{lr}$.

The reconstructed position in z shows a systematic shift towards larger $|z|$ for events in category I_z, while events in categories IIIa_z, IIIb_z, and IV_z are shifted towards $z = 0$. The extent of the former effect is larger than that of the latter.

The results hold for a simulation where energy depositions are represented by one single electron-hole pair, i.e. for pointlike energy depositions. In reality, energy depositions have an extension of about 1 mm. Some effect, especially close to the segment boundaries, is expected and some distributions will be washed out.

Chapter 5

Measurements and detector characterization

The task was to design and perform measurements which would allow the verification of the mirror pulse simulation and the method to reconstruct the position of single energy depositions. Such measurements have to collect events with predominantly one localized energy deposition. After several options were considered, a thorium source was used to collect DEP events from the 2.6 MeV ^{208}Tl line. The detector used was the 18–fold segmented n-type HPGe detector Siegfried III, SIII. A europium source was used to characterize the detector, i.e. to determine the energy dependence of the resolution of the detector, the position of the segment boundaries, and the orientation of the crystal axes.

5.1 Definition of localized events

A previously tested parameter to describe the localization of an event is the radius R_{90} [16]. It is defined as the radius of the volume that contains 90% of the total energy, E, deposited in an event. It is calculated by first determining the barycenter, $\boldsymbol{x}_{\mathrm{bc}}$, of the event,

$$\boldsymbol{x}_{\mathrm{bc}} = \frac{\sum_i E_i \boldsymbol{x}_i}{\sum_i E_i}, \tag{5.1}$$

where E_i and $\boldsymbol{x}_i$ are the energies and locations of the individual energy depositions. Subsequently, the energy depositions are ordered according to their distance to $\boldsymbol{x}_{\mathrm{bc}}$ and a resummation of the E_i, starting with the deposition closest to $\boldsymbol{x}_{\mathrm{bc}}$, is performed. The distance of the deposition at which the sum exceeds 90% of E is defined as R_{90}.

Single-site events are events with an R_{90} of the order of millimeters, implying that the significant energy depositions are in a small, localized volume. This is the case for most events in which the energy is deposited by electrons or positrons, since the range of electrons or positrons with an energy in the MeV-region is about one millimeter in germanium. Double beta decay events fall into this category, since the final state consists of two electrons emitted at the same position. Three types of photon induced processes mostly also fall into this category:

1. **Photoelectric absorption process:** The photon is absorbed in the process and the final state contains one electron only.
2. **Single Compton scattering:** The photon Compton-scatters only once in the detector. Thus, energy is deposited by only one electron inside the detector.
3. ***Double escape peak (DEP)* events:** The photon produces an electron-positron pair. If the two photons originating from the subsequent annihilation of the positron escape from the detector, only the ionization energies of the electron and the positron are deposited.

Multi-site events, on the contrary, are characterized by several large energy depositions separated by distances well above 1 mm. Typically, the R_{90} is of the order of centimeters. This is characteristic for events in which a photon with energy $E_\gamma = \mathcal{O}(\mathrm{MeV})$ Compton-scatters multiple times.

5.2 Options to obtain localized events

A clean sample of single-site events, as defined above, is difficult to obtain. The options considered were:

1. In a germanium detector, photons with $E_\gamma < 200\,\mathrm{keV}$ interact predominantly through the photo effect. Events from the 122 keV line of a ^{152}Eu source therefore seem to be good candidates. However, most mirror pulse amplitudes have an absolute value smaller than 5% of the real pulse amplitude. For a 122 keV photon, this results in mirror pulse amplitudes of less than 6 keV. The average noise level achieved in the experimental setup described below was $\approx 4\,\mathrm{keV}$. Such events could therefore not be used, since a large percentage of the mirror pulses could not have been distinguished from noise. In addition, the peak-to-background ratio for the 122 keV peak was less than 1.
2. Single Compton scattering events can be identified in coincidence measurements using two germanium detectors. Taking into account the measured energies and the angle between the detectors, events can be selected in which the photon Compton-scattered only once in the detector under examination. Since these measurements are very time consuming [39] and were geometrically unfeasible in the setup used, this was not practicable.
3. The decay chain of ^{228}Th contains ^{208}Tl, which subsequently decays into ^{208}Pb, emitting a photon with an energy of 2615 keV. This happens after 36% of all ^{228}Th decays. The associated DEP events deposit an energy of 1593 keV in the

detector. In the majority of the events, the corresponding mirror pulse amplitudes are thus well above the noise level.

The DEP events were chosen as the best practical solution. Due to their high energy of 2615 keV, the photons could not be collimated, so that the interaction positions are unknown. Their distribution, however, can be deduced from simulation. Therefore, distributions of the parameters of the mirror pulses as well as distributions of reconstructed positions can be compared for simulation and data.

5.3 Measurements

A sufficiently large data set was recorded to provide a sample of localized events from the DEP of ^{208}Tl. Data were taken to determine the background from environmental sources. In addition, a partial scan of the detector with a ^{152}Eu source was perfomed to provide data to characterize the detector.

5.3.1 Test facility

The 18–fold segmented *n*-type HPGe detector SIII, presented in Sec. 2.5, was operated in the test facility *Gerdalinchen II* [26], GII. This is a special cryostat that allows the operation of up to three segmented germanium detectors directly submerged in a cryogenic liquid. It consists of a dewar inside an aluminum tank. The tank has a height of 974 mm and a diameter of 612 mm.

A schematic of GII is depicted in Fig. 5.1(a). The top flange can be lifted to allow the mounting of the detectors onto a vertical stainless steel bar. Figure 5.1(b) shows the opening of the cryostat. The infrared shield is visible. Signal and high-voltage feed-throughs for three detectors are integrated in the top flange. The filling with cryoliquid and flushing with gaseous nitrogen is possible through the flange without opening the cryostat.

A movable holder with a tungsten collimator is also attached to the top flange. The collimator is shown, mounted together with SIII, in Fig. 5.1(c). In Fig. 5.1(d), the unmounted collimator is depicted. The collimator is 2.8 cm long and 2.4 cm wide. The bore has a diameter of 2 mm and the distance between collimator and detector is $\approx$ 1 cm. This leads to a spot size [1] of $\approx$ 3.5 mm. The collimator can be moved along ϕ over a range of $\approx 80^\circ$ and along z over the total height of the detector. It was placed such that segment 14 could be scanned completely and segments 13 and 15 could be scanned partially.

SIII was completely submerged in liquid nitrogen, LN, for the complete measurement period and the cryostat was refilled every 48 hours.

A bias voltage of +3000 V was applied to the core of SIII. The signals were transmitted using the Kapton cable depicted in Fig. 2.3(b) and wiring specific to GII. They were

[1]The spot size was defined purely geometrically as the diameter of an ideally collimated beam.

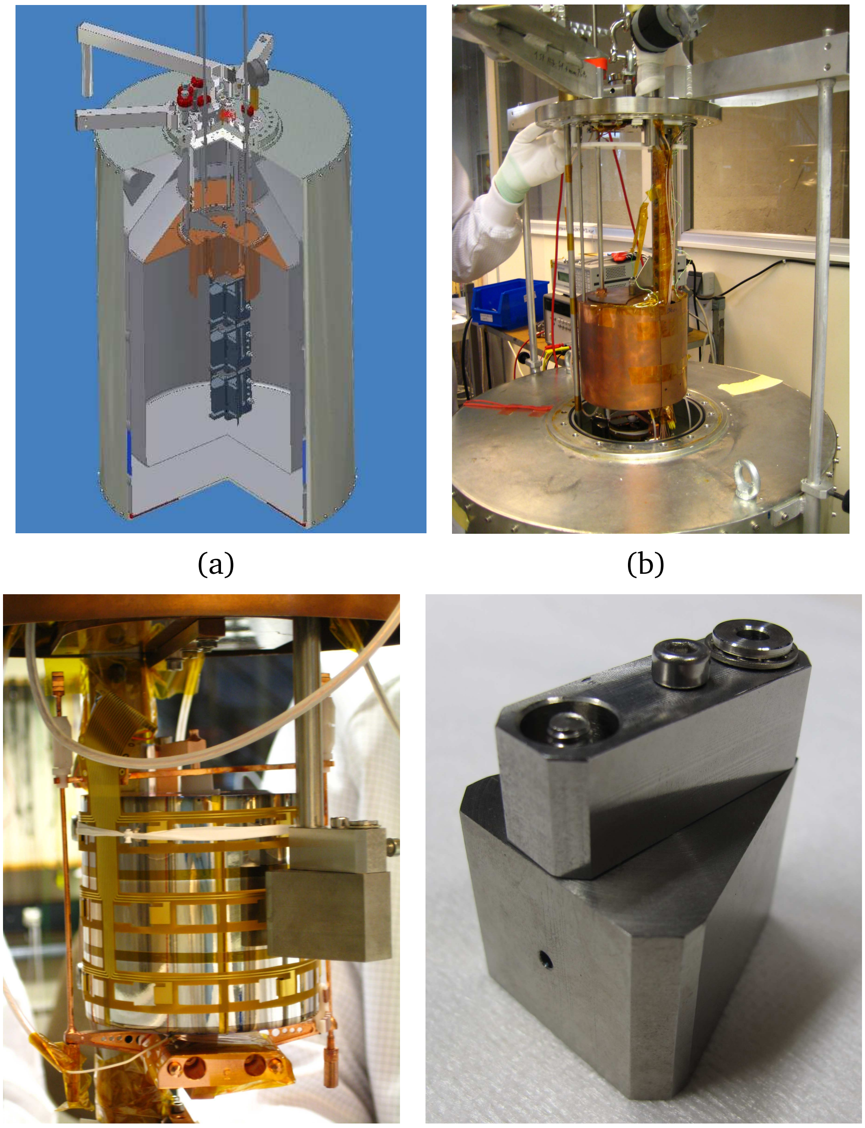

(a) (b) (c) (d)

Figure 5.1: (a) Schematic of GII. (b) Opening GII. (c) Mounted collimator in front of SIII. (d) Closeup of the collimator.

amplified by charge sensitive PSC-823C preamplifiers with a decay time of 50 μs. The 18 preamplifiers for all the segments and the preamplifier for the core were mounted inside two copper boxes on top of the top flange, which provided the common ground. The bandwidth limitation of the electronics was of the order of 10 MHz.

The amplified signals were digitized using a Pixie-4 XIA [40] data aquisition, DAQ, based on a 14-bit ADC with a sampling rate of 75 MHz. The core signal was used to trigger the events and the energies of the pulses were calculated using software filters. The energy determined for each segment and the core was recorded for every event in which the core energy, E_{core}, exceeded 40 keV. Within a certain measurement specific energy window, the digitized pulses themselves were also recorded for the core and all segments. A complete pulse record consisted of 300 samples, out of which 75 were baseline samples taken before the pulse.

5.3.2 Sources and data sets

A ^{228}Th source with an activity of 20 kBq was attached to the outside of the aluminum tank of GII at $\phi = 90^\circ$ and $z = -17$ cm, in the detector coordinate system defined in Fig. 4.1. During the measurements with the ^{228}Th source, also a ^{152}Eu source with an activity of 39 kBq was mounted in the tungsten collimator located inside the cryostat. It was positioned between $\phi = 168^\circ$ and $\phi = 244^\circ$ and $z = -16$ mm and $z = 16$ mm. Pulses were recorded for events with 1500 keV $< E_{\text{core}} <$ 3500 keV. The total lifetime of the measurement was $\approx$ 212 hours and a total of $9.35 \cdot 10^8$ events was recorded. The data set is referred to as Th_{data}.

To determine the background contribution due to environmental radioactivity in the ^{228}Th measurements, data was recorded without the ^{228}Th source. The pulses were recorded for all events. One part of the data set had the collimator with the ^{152}Eu source at $\phi = 40^\circ$ and $z = 0$ mm. It had a lifetime of 3.6 hours. The other part, with a lifetime of 4.0 hours, had the collimator at $\phi = 68^\circ$ and $z = 0$ mm. A total of $1.44 \cdot 10^7$ events was collected for each collimator position. The two sets were combined and are referred to as BG_{data}.

A partial scan of the detector was perfomed with the ^{152}Eu source inside the tungsten collimator. Measurements were carried out from $\phi = 168^\circ$ to $\phi = 244^\circ$ in steps of 2° at $z = 0$ mm and from $z = -16$ mm to $z = 16$ mm in steps of 2 mm at $\phi = 40^\circ$. Due to problems with the alignment, the collimator was rotated around its axis during the measurements by $\approx 3^\circ$. This lead to a systematic shift in the position in ϕ of $\Delta\phi \approx +2^\circ$ for all positions. The systematic uncertainties caused by varying shifts in the collimator adjustment are estimated to be $\pm 2^\circ$ in ϕ and ± 1 mm in z. Pulses were recorded for all events with 300 keV $< E_{\text{core}} <$ 400 keV, targeting the 344 keV line of ^{152}Eu. A total of $2.88 \cdot 10^6$ events was recorded for each scan point. The combined data set is referred to as Eu_{data}.

5.3.3 Offline selection

Offline, single-segment events, that is events in which exactly one of the segments had an energy deposition, E_{seg}, with $E_{\text{seg}} > 20$ keV, were selected. Segment 16 was not properly connected. This segment was ignored. To avoid events with a significant energy deposition in segment 16, events were also required to have $|E_{\text{core}} - E_{\text{seg}}| <$ 5 keV. Only the events fulfilling these selection criteria were used in the following.

Events were attributed to a given peak at energy E_p using a fit to the spectrum of the form

$$S(E) = \underbrace{\frac{c}{\sqrt{2 \cdot \Pi \sigma^2}} \cdot \mathrm{e}^{(-(E-\mu)^2/2\sigma^2)}}_{P(E)} + \underbrace{a \cdot E + b}_{B(E)}, \tag{5.2}$$

where E (σ, μ, c, a, b) is either E_{core} (σ_{core}, μ_{core}, c_{core}, a_{core}, b_{core}) or E_{seg} (σ_{seg}, μ_{seg}, c_{seg}, a_{seg}, b_{seg}). The peak is described by $P(E)$, while the background is described by $B(E)$. The fit range was ± 20 keV around E_p.

Figure 5.2(a) shows the core spectrum for Th_{data}. In Fig. 5.2(b), the DEP plus a fit according to Equation (5.2) is shown.

Events were selected for further analysis by requiring $|E_{\text{seg}} - E_p| < \sigma_{\text{seg}}$, where σ_{seg} was always the value obtained from the fit to Th_{data}.

DEP events in Th_{data} and BG_{data} were selected with $E_p = 1593$ keV. The resulting data sets are referred to as DEP_{data} and DEP_{BG}. They contain $3.88 \cdot 10^4$ and $1.35 \cdot 10^2$ events, respectively. These data sets were further reduced to ignore events with

- the left or the right mirror pulse in segment 16. These are events in which the energy was deposited in segments 3 or 17. The reduced data sets are referred to as $\text{DEP}_{\text{data},\phi}$ and $\text{DEP}_{\text{BG},\phi}$ and contain $3.35 \cdot 10^4$ and $1.13 \cdot 10^2$ events, respectively.
- the upper mirror pulse in segment 16. These are events in which energy was deposited in segment 13. The reduced data sets are referred to as $\text{DEP}_{\text{data},z}$ and $\text{DEP}_{\text{BG},z}$ and contain $8.25 \cdot 10^3$ and 32 events, respectively.

From Eu_{data}, data samples were selected using $E_p = 344$ keV and requiring the energy to be deposited in segment i, where $i = 11, 13, 14, 15, 17$. The corresponding data sets are referred to as Eu344_i.

5.3.4 Signal-to-background ratio

The signal is the number of events attributed to the peak, p. It is calculated as

$$p = \int_{E_p-\sigma}^{E_p+\sigma} P(E)\, dE.$$

The number of events attributed to background, b, is

$$b = \int_{E_p-\sigma}^{E_p+\sigma} B(E)\, dE.$$

The values of p and the peak-to-background ratios, p/b, for the DEP of ^{208}Tl are listed in Appendix B. The ratios are all above 2 and significantly better for the core and most of the segments. The FWHM of the core and all segments are also listed in Appendix B; the value for the core is 5.4 keV, while the segments have values between 4.3 keV and 5.3 keV.

In Appendix C, the lifetime, t_{life}, the number of signal events per unit time, p/t_{life}, the peak-to-background ratio, p/b, and the FWHM of the corresponding measurement are reported for segments 13, 14, and 15 for the scan in ϕ and for segments 11, 14, and 17 for the scan in z.

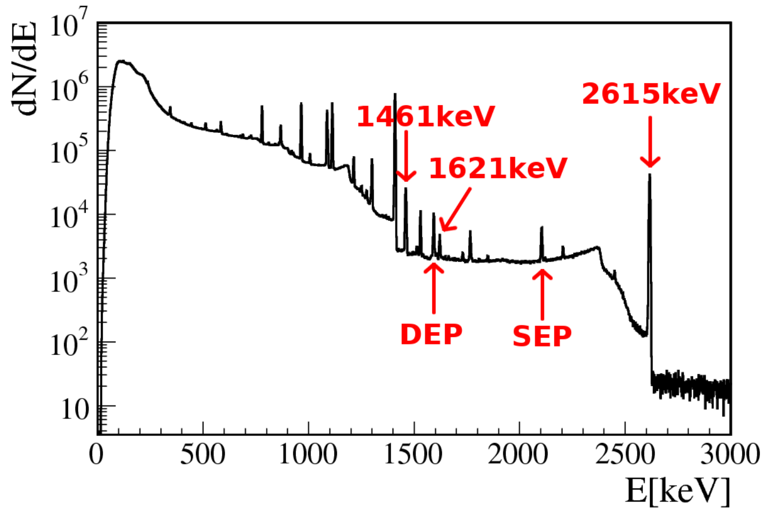

(a)

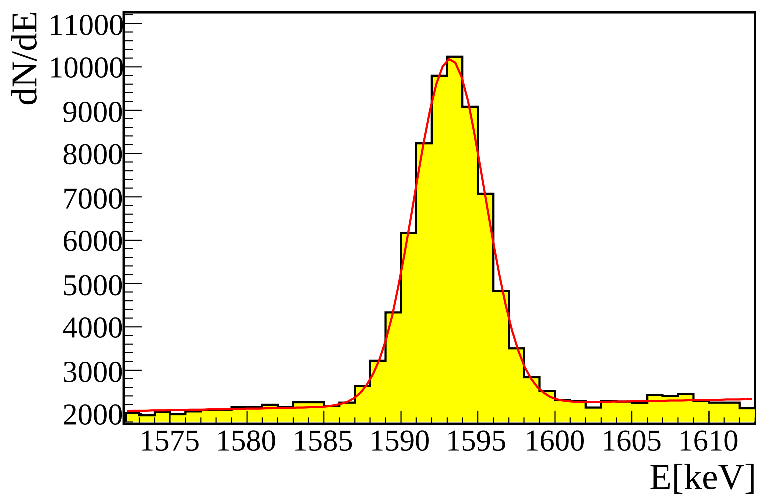

(b)

Figure 5.2: (a) The spectrum of the core. The DEP, SEP, 1621 keV peak, and 2615 keV peak of the ^{228}Th decay and a 1461 keV peak from ^{40}K are indicated. (b) The DEP of the core. Also shown is a fit with $S(E)$.

5.3.5 Noise level

The noise level was determined offline for the selected DEP_{data} events. For each event, the offset from 0 of the baseline of each segment pulse and the core pulse was calculated by averaging over the first 40 samples. This offset was then subtracted from each of the 300 samples of the pulse. The amplitude of the core pulse was normalized to one; all 17 segment pulses were normalized to the core pulse. The values of the first 40 samples of all 17 segment pulses of all events together were fitted with a Gaussian function. Figure 5.3 shows the measured noise together with the fit.

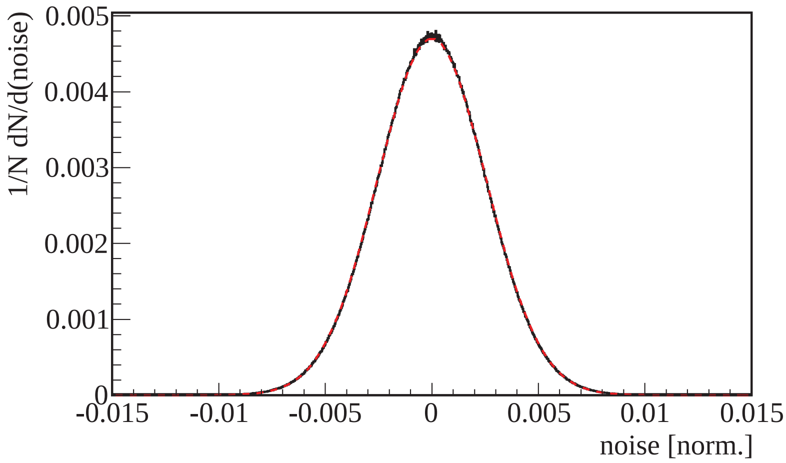

Figure 5.3: Deviation from 0 of the first 40 samples of all pulses from the 17 active segments in the DEP_{data} events. The histogram was normalized to the total number of entries. Also shown is a fit with a Gaussian function.

The noise level is defined as the width of the Gaussian function. It is $\sigma = (2.5454 \pm 0.0004) \cdot 10^{-3}$, which corresponds to $\approx 4.0\,\text{keV}$. The fit describes the data well ($\chi^2/NDF = 5.7$), indicating that the noise is indeed Gaussian.

5.3.6 Contribution of the environmental background

The data set BG_{data} was used to determine the background from environmental sources for DEP_{data}. The ^{152}Eu source was present during this measurement in accordance to its presence during the ^{228}Th running. To normalize the relevant data set, i.e. DEP_{BG}, to DEP_{data}, the peak of the decay of ^{40}K at 1461 keV, indicated in Fig. 5.2(a), was used. It does not appear in either the decay chain of ^{228}Th, or in the decay chain of ^{152}Eu. The ratio, R, is defined as $R = N_{\text{Th}}^{^{40}\text{K}}/N_{\text{BG}}^{^{40}\text{K}}$, where $N_{\text{Th}}^{^{40}\text{K}}$ ($N_{\text{BG}}^{^{40}\text{K}}$) is the number of events associated to the peak in the Th_{data} (BG_{data}) sample. R was determined for the core and all 17 active segments and averaged. Its value of $R = 31 \pm 4$ was used as input to all statistical comparisons between data and simulation, where the background was not simulated but subtracted from the data distribution. Within statistical errors, the value obtained for R is compatible with the relative lifetimes of the measurements.

5.4 Detector characterization

Parameters needed for the pulse shape simulation had to be obtained. They were acquired in a detector characterization using the data sets $\mathrm{Th}_{\mathrm{data}}$, $\mathrm{Eu}_{\mathrm{data}}$, and $\mathrm{Eu344}_i$.

5.4.1 Energy dependence of the resolution

The resolution is a function of the energy. To quantify this dependence, the FWHM of the core was plotted against E_p for several peaks in the ^{152}Eu spectrum and for the 2615 keV peak in the ^{228}Th spectrum. The result is depicted in Fig. 5.4.

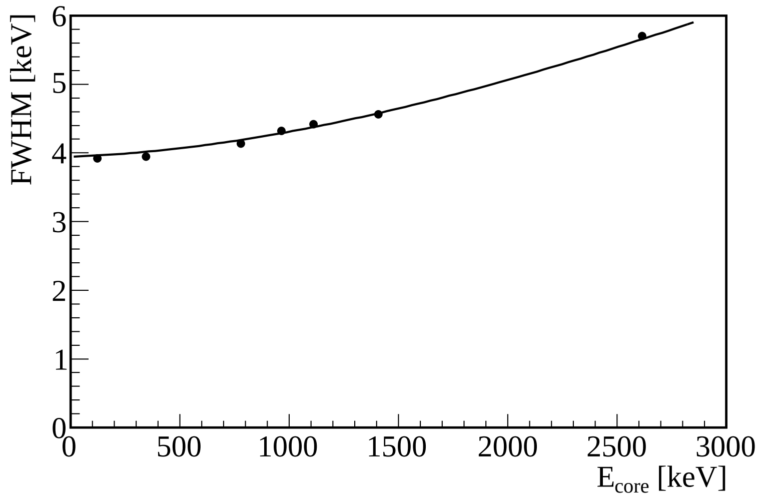

Figure 5.4: FWHM of the core as a function of the energy. A fit with Equation (5.3) is shown.

As discussed in Chapter 2, there are three effects that contribute to the energy resolution: the Fano term, the collection efficiency, and the energy-independent electronic noise. The FWHM in keV as a function of the energy is then expressed as

$$\mathrm{FWHM} = \Big(\underbrace{a \cdot (2.35^2 \cdot 2.96 \cdot 0.001) \cdot E_{\mathrm{core}}}_{\text{Fano term}} + \underbrace{b \cdot (0.001 \cdot E_{\mathrm{core}})^2}_{\text{efficiency}} + \underbrace{c^2}_{\text{noise}}\Big)^{1/2}, \qquad (5.3)$$

where E_{core} is in keV and a, b, and c are the fit parameters.

From a fit of Equation (5.3) to the distribution in Fig. 5.4, the parameters a, b, and c were obtained. They are reported in Table 5.1. The uncertainties listed are statistical only.

The resolution for a given E_{core} can be estimated using these results. Around the energy of the DEP, it is dominated by the electronic noise of ≈ 4 keV. The detector contribution can be estimated to be around 2.5 keV.

a	0.0600 ± 0.0019
b	2.03 ± 0.01
c	3.94 ± 0.01

Table 5.1: Results from fitting Equation (5.3) to the FWHM as a function of E_{core}. The uncertainties are statistical only.

5.4.2 Segment boundaries and crystal axes

Low energy photons with 122 keV from the ^{152}Eu decay can be used to determine the position of the segment boundaries as well as the position of the crystal axes. They can be collimated well and have a mean free path of only about 6 mm in germanium, see Fig. 2.1. The energy is deposited locally and predominantly close to the outer surface.

Segment boundaries are determined from the dependence of p/b on the scan position.

The orientation of the crystal axes is deduced from variations of the drift time of the charge carriers. The charge carrier creation close to the surface leads to long drift times for electrons, while the holes are collected quickly. This is desirable, since the variations in the drift times, which are due to the londitudinal anisotropy, are maximal.

Unfortunately, $p/b < 1$ for the 122 keV peak in Eu_{data}. Therefore, the Eu344_i samples were used. Photons with $E_\gamma = 344$ keV have a mean free path of about 2 cm in germanium. Thus, the interactions are still predominantly relatively close to the surface. Simulations concerning the localization showed that in 95% of all cases $R_{90} <$ 1 cm. The bandwidth limitation of the electronics is of the order of 10 MHz. With a velocity of ≈ 0.1 mm/ ns of the charge carriers, the position resolution is ≈ 1 cm. Thus, the local spread cannot be dissolved and the energy depositions of 344 keV photons can be considered single-site for this purpose.

Segment boundaries

The position of the segment boundaries in ϕ was determined from the correlation between p/b and ϕ in the data sets Eu344_{13}, Eu344_{14}, and Eu344_{15}. The result is depicted in Fig. 5.5(a).

For an infinitely small beam spot and single pointlike energy depositions, p/b would be constant within the segment and drop to zero at the boundary. In reality, the collimator provides a finite spot size and energy is deposited in a finite volume, creating clouds of charge carriers instead of single charge carriers. Therefore, the dependence of p/b on ϕ is smeared and the position of the boundaries corresponds to the point, where p/b becomes equal for two neighboring segments.

The accidental rotation of the collimator around its axis caused the distribution to be distorted. The collimator was rotated towards larger ϕ. As a consequence of the mean free path of the photons of about 2 cm, already at relatively large distances from the right segment boundary, some photons penetrated deeply enough to deposit their energy in segment 15. This explains the decrease in p/b in segment 14 and the

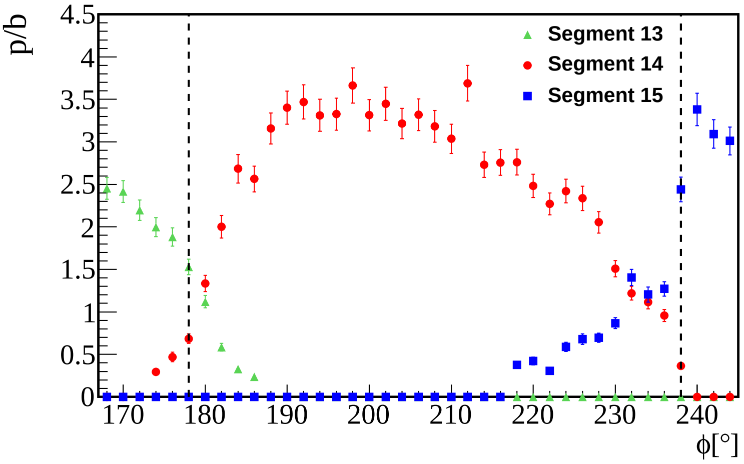

(a)

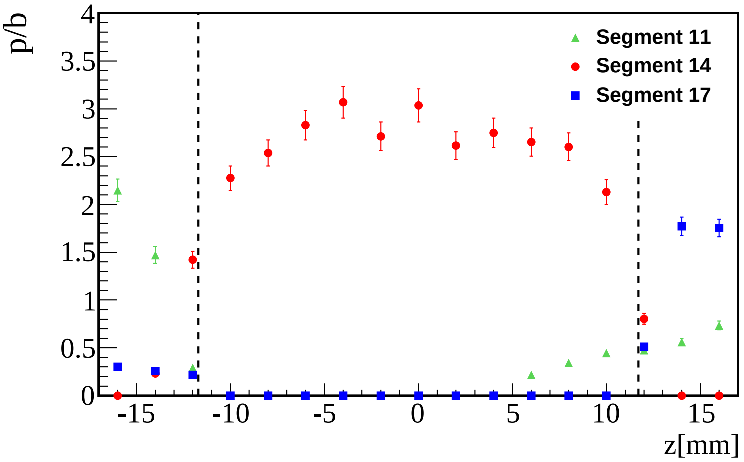

(b)

Figure 5.5: (a) Correlation between p/b and ϕ for $\mathrm{Eu344}_{13}$, $\mathrm{Eu344}_{14}$, $\mathrm{Eu344}_{15}$. (b) Correlation between p/b and z for $\mathrm{Eu344}_{11}$, $\mathrm{Eu344}_{14}$, and $\mathrm{Eu344}_{17}$. The uncertainties are statistical only. The segment boundaries determined from the measurements are indicated with dashed lines.

simultaneous increase of p/b in segment 15 starting at $\phi \approx 214°$. At the left boundary, the drop of p/b in segment 14 is sharp, since even close to the boundary almost all photons deposit their energy in segment 14.

The boundaries of segment 14 determined naively from Fig. 5.5(a) would be at $\phi = 180°$ and $\phi = 234°$. This results in an effective segment size of only 54°. The fact that segment 14 has a smaller effective volume than expected from the nominal segment widths of 60° hints at the influence of a crystal axis as described in Chapter 4. After the determination of the axes orientation and the inclusion of its effects in the simulation, the reduction of the effective volume could be confirmed. The corresponding nominal geometric segment boundaries of segment 14 are at

$\phi = 178°$ and $\phi = 238°$. They are indicated in Fig. 5.5(a). Adding 2° to these results to account for the systematic shift due to the rotation of the collimator and taking into account the statistical uncertainties and the systematical uncertainties of the positioning of the collimator, the boundaries of segment 14 were determined to be at $\phi = 180° \pm 3°$ and $\phi = 240° \pm 3°$. The other segment boundaries in ϕ follow from this.

The correlation between p/b and z for $Eu344_{11}$, $Eu344_{14}$, and $Eu344_{17}$ was analyzed to determine the segment boundaries in z. It is shown in Fig. 5.5(b). No distortions similar to the ones in Fig. 5.5(a) can be observed. Taking into account the statistical and systematical uncertainties, the segment boundaries are determined to be at $z = -11.7\,\text{mm} \pm 2\,\text{mm}$ and at $z = 11.7\,\text{mm} \pm 2\,\text{mm}$. This is in agreement with the nominal size of the segment.

An a priori surprising feature is that p/b for segment 11 is increasing again when the beam gets close to the upper boundary of segment 14 at $z \geq 6\,\text{mm}$, eventhough segment 11 is located below segment 14. The equivalent effect is seen for segment 17 at $z \leq -14\,\text{mm}$. This is due to the geometry of the holder of the source behind the collimator. There is no tungsten underneath and above the source, leaving a small solid angle through which photons can escape upwards and downwards. Close to the detector center, these photons do not hit the detector. At small z, however, the photons escaping upwards hit the top layer of the detector, while photons escaping downwards deposit energy in the bottom layer when the collimator is positioned at large z.

Crystal axes

The crystal axes are determined exploiting the variations in the drift times at different ϕ due to the longitudinal anisotropy. Along the crystal axis <110>, the drift time is maximal, while it is minimal along the crystal axis <100>.

The *10-90-risetime*, τ_{10-90}, is a measure of the drift time. It is the time period between the point, where a real pulse reaches 10% and 90% of its final amplitude.

Fig. 5.6 shows the fraction of events with $\tau_{10-90} > 260\,\text{ns}$ for the core pulse for $Eu344_{13}$ from $\phi = 168°$ to $\phi = 178°$, for $Eu344_{14}$ from $\phi = 180°$ to $\phi = 234°$, and for $Eu344_{15}$ from $\phi = 136°$ to $\phi = 244°$. The respective data samples were chosen taking into account the effective segment boundaries. Also shown is a fit with a sine function with a period of 90°. Deviations from the sine function are only observed close to the segment boundaries. These can be accounted for by the accidental rotation of the collimator. At the boundaries, photons with a shorter penetration depth deposit their energy in one segment, while photons with a longer penetration depth interact in the other segment. This causes large variations in the drift times of the electrons, which disguise the smaller effect due to the longitudinal anisotropy. Therefore, the four data points that are closest to the left and right segment boundary of segment 14, respectively, were excluded from the fit.

The position of the crystal axis <110> is determined as the maximum of the sine function fitted to the data. It is at $\phi = 210°$. Adding $\Delta\phi$ to account for the systematic shift due to the rotation of the collimator and taking into account the statistical and

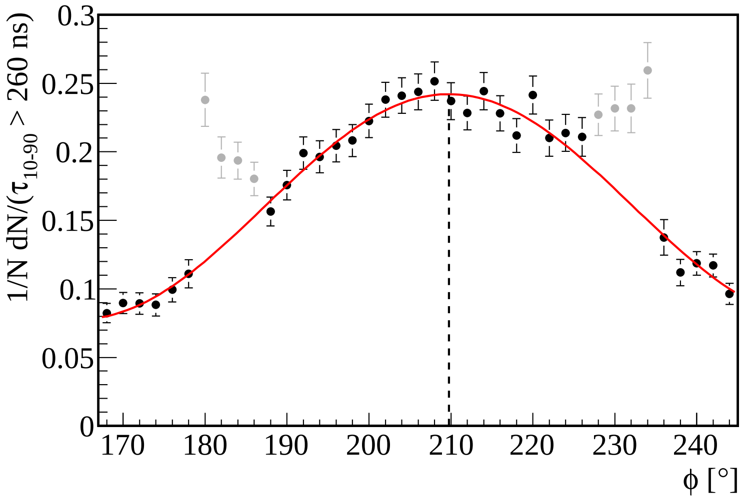

Figure 5.6: Fraction of events with $\tau_{10-90} > 260\,\mathrm{ns}$ for the core pulse for Eu344$_{13}$ from $\phi = 168°$ to $\phi = 178°$, for Eu344$_{14}$ from $\phi = 180°$ to $\phi = 234°$, and for Eu344$_{15}$ from $\phi = 136°$ to $\phi = 244°$. The uncertainties are statistical only. Also shown is a fit of a sine function to the data. The data points indicated in light grey were excluded from the fit.

systematical uncertainties, the crystal axis <110> is determined to be at $\phi = 212° \pm 3°$. Accordingly, crystal axes <110> are also at $\phi = 302° \pm 3°$, $\phi = 32° \pm 3°$, and $\phi = 122° \pm 3°$. The crystal axes <100> are found at $\phi = 257° \pm 3°$, $\phi = 347° \pm 3°$, $\phi = 77° \pm 3°$, and $\phi = 167° \pm 3°$.

5.4.3 Impurity density

Equation (2.1) gives the relation between the depletion voltage, V_{depl}, and the impurity density, ρ_{imp}, for a true coaxial detector with fixed inner radius, r_i, and outer radius, r_o. From this, ρ_{imp} can be determined through the determination of V_{depl}. For SIII, $V_{\mathrm{depl}} = +2500\,\mathrm{V}$ was estimated, see Section 2.5. This leads to $\rho_{\mathrm{imp}} = 0.7 \cdot 10^{10}\,\mathrm{cm}^{-3}$.

According to the manufacturer, ρ_{imp} varies between $\rho_{\mathrm{imp}} = 0.61 \cdot 10^{10}\,\mathrm{cm}^{-3}$ at the bottom and $\rho_{\mathrm{imp}} = 1.35 \cdot 10^{10}\,\mathrm{cm}^{-3}$ at the top of SIII. However, the larger value would not allow for the detector to be fully depleted at a bias voltage of +2500 V. A uniformly distributed $\rho_{\mathrm{imp}} = 0.7 \cdot 10^{10}\,\mathrm{cm}^{-3}$ was chosen for all simulations.

Chapter 6

Monte Carlo

In Chapter 5, DEP events from 2.6 MeV photons from the decay of ^{208}Tl were identified as a good data sample to verify the pulse shape simulation and to test the method to reconstruct the position of single energy depositions developed in Chapter 4. As 2.6 MeV photons can basically not be collimated and their mean free path in germanium is ≈ 5 cm, the interaction point cannot be controlled. However, distributions of mirror pulse parameters and reconstructed positions can be compared. To allow this, events were generated for the setup described in Chapter 5. Pulses were simulated for events associated to the DEP. The interaction points were reconstructed and compared to the MC-true position. The resolutions obtained were compared to the results in Chapter 4.

6.1 Monte Carlo description of the setup

The Monte Carlo framework MaGe was used to simulate the experimental setup described in Chapter 5. A schematic of the geometry implemented for GII is shown in Fig. 6.1. Events were only generated for the ^{228}Th source. Its position is indicated in Fig. 6.1. The source was simulated as a cuboid with a length and width of 3 mm and a height of 1 mm. As the stainless steel capsule is very thin (≈ 1.4 mm), only the radioactive material was implemented. The specifications about the geometry of the radioactive material were provided by the manufacturer of the source.

6.2 Event generation

Within the MaGe framework, GEANT4 with its low energy parameter settings was used to simulate the actual interactions.

Due to the large distance of the ^{228}Th source from the detector and the large amount of simulated events needed to obtain a significant number of DEP events, simulating the complete decay chain of ^{228}Th was too time consuming. Only the relevant photon lines were simulated. This was primarily the 2615 keV line from ^{208}Tl.

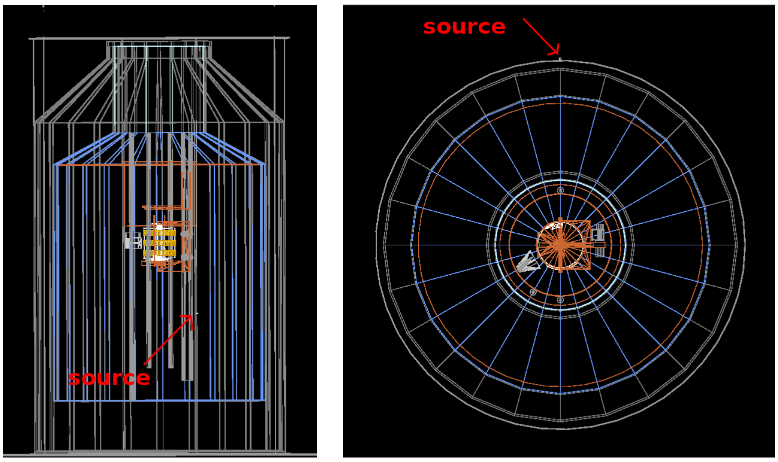

(a) (b)

Figure 6.1: (a) Schematic of the geometry implemented for GII. (b) Top view. The position of the ^{228}Th source is indicated in both cases.

In addition, photon lines above 1593 keV, the DEP energy of 2615 keV ^{208}Tl photons, need to be generated, if they contribute significantly to the background under the DEP. This happens when the photons Compton-scatter in the detector and deposit $\approx$ 1593 keV before escaping from the detector. They can also Compton-scatter in the material surrounding the detector, losing a part of their energy, and then deposit the remaining energy of $\approx$ 1593 keV in the detector. In the Th$_{\mathrm{data}}$ spectrum shown in Fig. 5.2(a), only one relevant peak is visible. It originates from the decay of ^{212}Bi to ^{212}Po and the photons have an energy of 1621 keV. This was the only photon line simulated besides the signal line.

The output of GEANT4 is a list of hits with energies E_i. The energy in a segment, E_{seg}, is calculated as

$$E_{\mathrm{seg}} = \sum_i^{\mathrm{seg}} E_i,$$

where the sum runs over all hits in the segment. The nominal segment boundaries were used, because E_{seg} was calculated before the drift of the charge carriers. The energy of the core, E_{core}, was calculated as

$$E_{\mathrm{core}} = \sum_i^{\mathrm{event}} E_i,$$

where the sum runs over all hits in the event.

The energy resolution was dominated by the read-out system, which was globally taken into account by smearing E_{seg} and E_{core} with the resolutions determined from data, see Sec. 5.4.1, Equation (5.3), and Table 5.1.

A total of $9 \cdot 10^9$ photons with $E_\gamma = 2615$ keV and $4 \cdot 10^8$ photons with $E_\gamma = 1621$ keV was simulated. Energy was deposited in the detector in $6.52 \cdot 10^7$ events in the first case and in $2.99 \cdot 10^6$ events in the second case.

6.3 Event selection and normalization

Single-segment events, that is events in which exactly one of the segments had an energy deposition with $E_{seg} > 20\,\text{keV}$, were selected. In addition, the events were required to have $|E_{core} - E_{seg}| < 5\,\text{keV}$, in analogy to the selection criteria applied to the data. This was done for the output of the simulation of 2615 keV photons as well as for the output of the simulation of 1621 keV photons. The respective data sets are referred to as MC2615 and MC1621. They contain $4.38 \cdot 10^7$ and $2.09 \cdot 10^6$ events, respectively.

MC2615 and MC1621 were combined to the data sample Th_{simu}. The contribution of MC1621 to Th_{simu}, C, can be determined from the relative intensity of the 1621 keV line to the 2615 keV line. The respective branching ratios of the decay of ^{228}Th are 35.86% and 1.49%. This results in $C = 4.2\%$.

To check whether the data was well understood, C was also determined using Th_{data}, MC2615 and MC1621. In Th_{data}, the DEP, single escape peak (SEP), the 1621 keV and the 2615 keV peak were fitted with Equation (5.2) for the relevant $E_p \pm 20\,\text{keV}$. The resulting number of events associated to the respective peak, $N_{\text{DEP,data}}$, $N_{\text{SEP,data}}$, $N_{\text{1621,data}}$, and $N_{\text{2651,data}}$, was used to calculate the ratio $r_x = N_{\text{1621,data}}/N_{x,\text{data}}$, where $x = \text{DEP, SEP, 2615}$. This was done for all segments and the core.

For MC2615, the number of events associated to the DEP, the SEP, and the 2615 keV peak, $N_{\text{DEP,simu}}$, $N_{\text{SEP,simu}}$, and $N_{\text{2615,simu}}$, were calculated using Equation (5.2). For MC1621, the number of events associated to the 1621 keV peak, $N_{\text{1621,simu}}$, was determined. The normalization, f, of the MC1621 keV sample is determined from the requirement $r_x = f \cdot N_{\text{1621,simu}}/N_{x,\text{simu}}$. The normalization was done separately for all segments and the core for every x. It was first averaged over all segments and the core for the individual x and then averaged over all x to obtain the final $f = 0.82 \pm 0.11$. This results in $C = (3.8 \pm 0.5)\%$, which is in agreement with the value determined from the branching ratios. This shows that the data is understood well.

From Th_{simu}, a data sample corresponding to DEP_{data} was selected by requiring $|E_{seg} - 1593\,\text{keV}| < \sigma_{seg}$, where σ_{seg} was determined from Th_{simu}. The sample is referred to as DEP_{simu}. It contains $1.04 \cdot 10^5$ events. In Appendix D, p, p/b, and the FWHM at $E_p = 1593\,\text{keV}$ are listed for the core and all segments.

The data set DEP_{simu} was further reduced to ignore events with

- the left or the right mirror pulse in segment 16. These are events in which the energy was deposited in segments 3 or 17. The reduced data set is referred to as $\text{DEP}_{\text{simu},\phi}$ and contains $8.40 \cdot 10^4$ events.

- the upper mirror pulse in segment 16. These are events in which energy was deposited in segment 13. The reduced data set is referred to as $\text{DEP}_{\text{simu},z}$ and contains $1.86 \cdot 10^4$ events.

6.4 Pulse shape simulation

For all events of the $\mathrm{DEP_{simu}}$ sample, the barycenter of the energy deposition was calculated using Equation (5.1). The sum runs over all hits. For each event, the pulse shapes corresponding to a single energy deposition at $\boldsymbol{x}_{\mathrm{bc}}$ were simulated. The input parameters to the pulse shape simulation were the ones deduced from the data in Chapter 5: $\rho_{\mathrm{imp}} = 0.7 \cdot 10^{10}\,\mathrm{cm}^{-3}$, the segment boundaries of segment 14 at $\phi = 180°$ and $\phi = 240°$, and $z = -11.7\,\mathrm{mm}$ and $z = 11.7\,\mathrm{mm}$ and all other segment boundaries following from this, the crystal axes <110> at $\phi = 32°$, and a noise level of 0.25%. The bandwidth-cutoff was set to 10 MHz and the decay constant to $\tau = 50\,\mu\mathrm{s}$.

6.5 True spatial distribution

Figure 6.2 shows the distributions in r, ϕ, and z of the barycenter of the energy depositions for $\mathrm{DEP_{simu}}$.

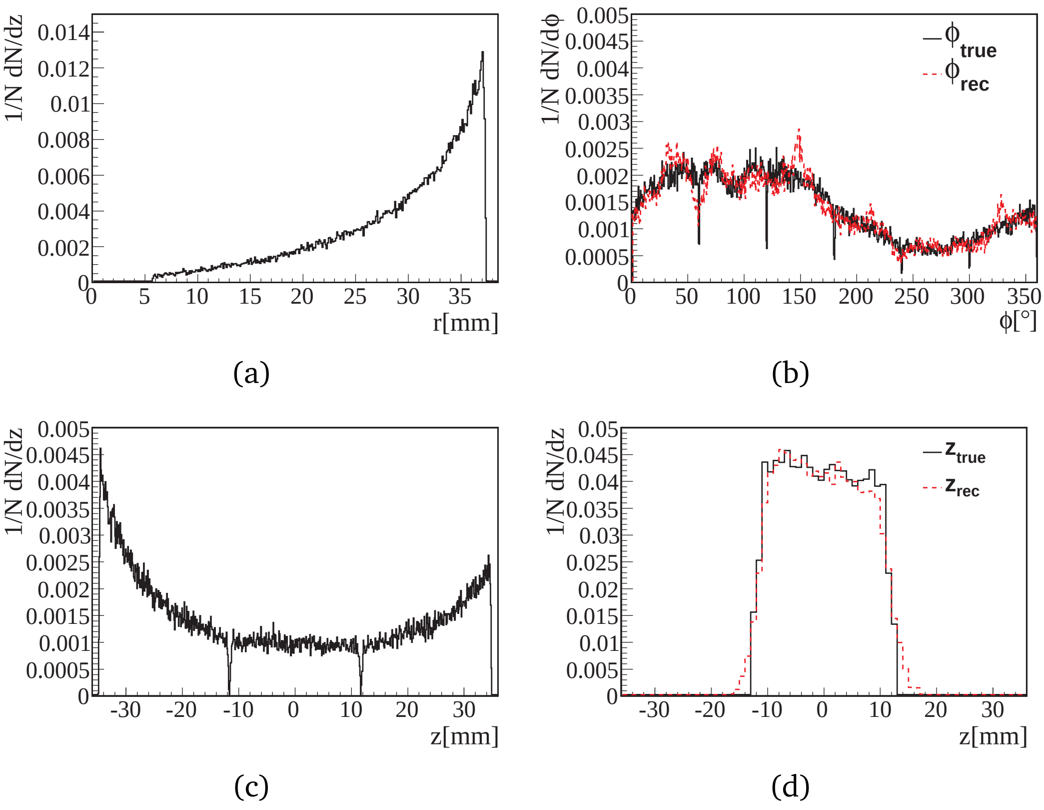

Figure 6.2: Distribution of the barycenter of the energy depositions for $\mathrm{DEP_{simu}}$ in (a) r, (b) ϕ, (c) z, and (d) z for the middle layer of the detector. In (b) and (d), also the distribution of the reconstructed positions are shown. The distributions are normalized to the number of events.

The distribution rises with r. This is due to the fact that the probability of both photons from the annihilation of the positron to escape is higher close to the surface.

This also explains the increase in the number of events with $|z|$. The asymmetry in the distribution in z is explained by the fact that the source was located below the detector, resulting in a larger fraction of events in the bottom layer of the detector. The source was located at $\phi = 90°$. This is resembled in the distribution in ϕ. The dip in the number of events at $\phi \approx 90°$ can be accounted for by the presence of a stainless steel gas tube between the source and the detector. At the segment boundaries, the number of events decreases, because close to a boundary hits are likely to be in both segments, even for single-site events, leading to significant energy depositions in both segments. Events close to the boundaries are thus extremely rare in $\mathrm{DEP_{simu}}$.

6.6 Test of position reconstruction

The method to reconstruct the position of single energy depositions developed in Chapter 4 was tested with the $\mathrm{DEP_{simu}}$ sample. The position in ϕ and z was reconstructed for all events and the deviations from the true position as defined in Equations (4.2) and (4.4) were calculated.

The reconstruction in ϕ was possible for $(99.60 \pm 0.44)\%$ of the events contained in $\mathrm{DEP_{simu}}$. For $(0.39 \pm 0.02)\%$, the reconstruction was not possible due to an amplitude of one of the mirror pulses that was smaller than two times the noise level. In $(0.01 \pm 0.01)\%$ of all cases, the event did not fit in any of the categories of $\hat{\tau}_{lr}$.

The reconstruction in z was possible for $(98.02 \pm 0.90)\%$ of all events in the middle layer of the detector or $(22.83 \pm 0.16)\%$ of all events. For $(1.82 \pm 0.09)\%$ of the events in the middle layer, the reconstruction failed due to a too small amplitude of one of the mirror pulses. For $(0.16 \pm 0.03)\%$ of the events in the middle layer, the event did not fit in any of the categories of $\hat{\tau}_{ud}$.

The distribution of the reconstruced ϕ, ϕ_{rec}, is shown together with the distribution of the true ϕ, ϕ_{true}, in Fig. 6.2(b). The distributions of ϕ_{true} and ϕ_{rec} agree well. A fraction of the events is reconstructed too close to the segment center. This was expected from the results obtained in Sec. 4.4.2. The effect is largest for events with $120° < \phi_{\mathrm{true}} < 180°$ and $300° < \phi_{\mathrm{true}} < 360°$, that is in segments 16, 13, 10, and 1, 4, 7, while it is almost absent for events with $60° < \phi_{\mathrm{true}} < 120°$ and $240° < \phi_{\mathrm{true}} < 300°$, that is in segments 3, 6, 9, and 18, 15, 12. This is explained by the relative position of the segment boundaries to the crystal axes.

The distributions of the reconstructed z, z_{rec}, and the true z, z_{true} for the middle layer are depicted in Fig. 6.2(d). Again, the agreement is good. A small percentage of the events is reconstructed outside the segment. This can be accounted for by the shift to higher $|z|$ for a fraction of the events in category I_z, as discussed in Sec. 4.4.3. The effect is small, though, since events in category I_z are located at small r and the number of DEP events is small in this region.

Figures 6.3 and 6.4 show the distributions of $\Delta\phi = (\phi_{\mathrm{true}} - \phi_{\mathrm{rec}}) \cdot r$ for events in categories I_ϕ, II_ϕ, IIIa_ϕ, IIIb_ϕ, and IV_ϕ and of $\Delta z = z_{\mathrm{true}} - z_{\mathrm{rec}}$ for events in categories I_z, II_z, IIIa_z, IIIb_z, and IV_z, respectively.

All distributions but those for categories IIIa_ϕ and IIIb_ϕ and for categories IIIa_z and

$IIIb_z$ were fitted with a Gaussian function to determine the resolution, σ_ϕ and σ_z. The results are listed in Tables 6.1 and 6.2. For all cases, the results are similar to those obtained in Chapter 4.

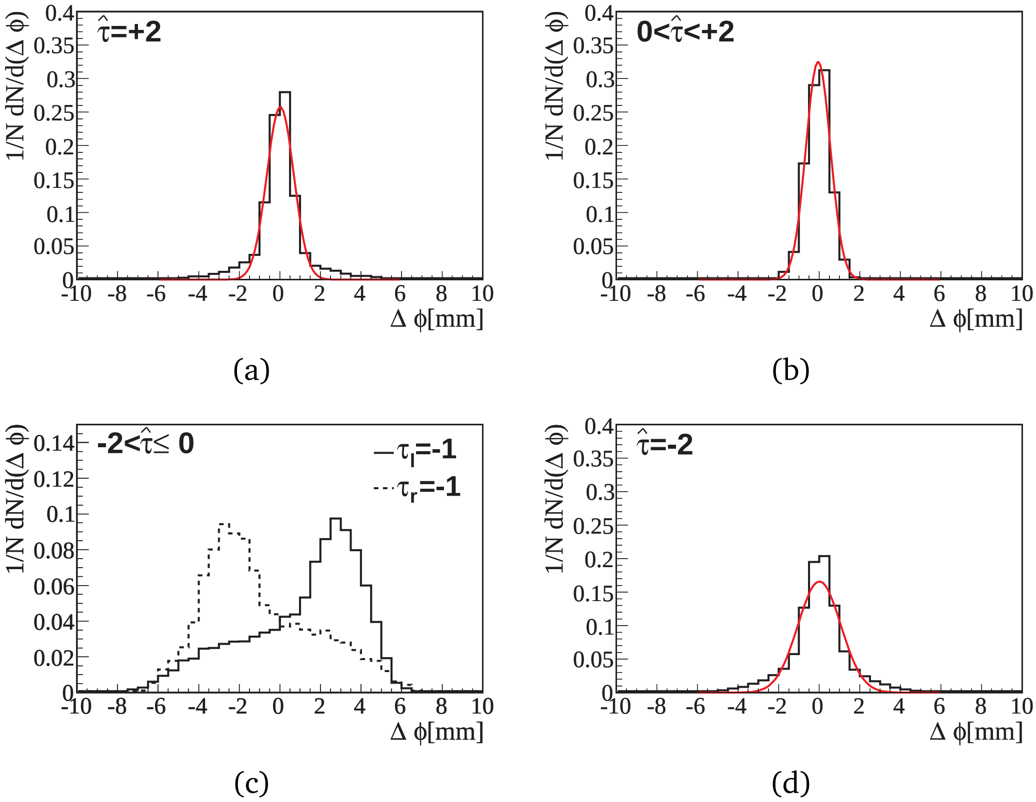

Figure 6.3: Distribution of $\Delta\phi$ for events in category (a) I_ϕ ($\hat{\tau}_{lr} = +2$), (b) II_ϕ ($0 < \hat{\tau}_{lr} < +2$), (c) $IIIa_\phi$ and $IIIb_\phi$ ($-2 < \hat{\tau}_{lr} \leq 0$), (d) IV_ϕ ($\hat{\tau}_{lr} = -2$) for DEP_{simu}. The distributions are normalized to the total number of events in each case. In (a), (b), (d), fits to a Gaussian function are also shown.

category	σ_ϕ [mm]
I_ϕ	0.67 ± 0.01
II_ϕ	0.60 ± 0.02
IV_ϕ	1.06 ± 0.01

Table 6.1: Results of fitting a Gaussian function to the $\Delta\phi$-distribution for DEP_{simu}. The fit was done separately for category I_ϕ ($\hat{\tau}_{lr} = +2$), II_ϕ ($0 < \hat{\tau}_{lr} < +2$), and IV_ϕ ($\hat{\tau}_{lr} = -2$).

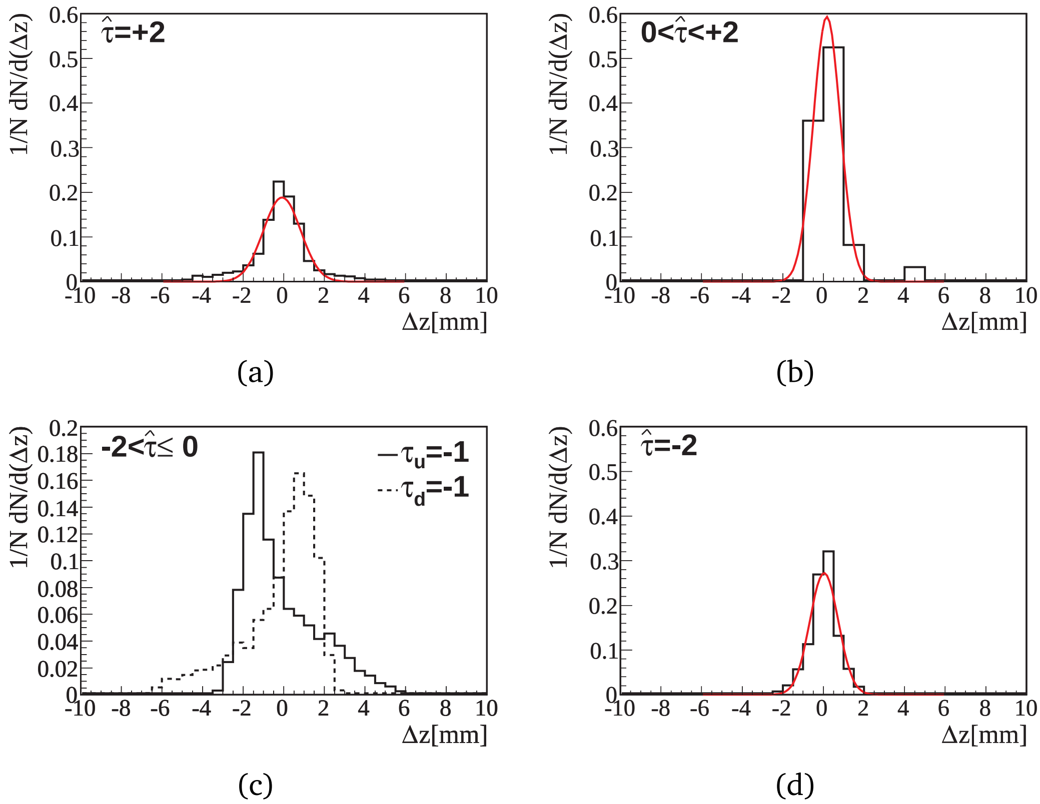

Figure 6.4: Distribution of Δz for events in category (a) I_z ($\hat{\tau}_{ud} = +2$), (b) II_z ($0 < \hat{\tau}_{ud} < +2$), (c) IIIa_z and IIIb_z ($-2 < \hat{\tau}_{ud} \leq 0$), (d) IV_z ($\hat{\tau}_{ud} = -2$) for $\mathrm{DEP}_{\mathrm{simu}}$. The distributions are normalized to the total number of events in each case. In (a), (b), (d), fits to a gaussian function are also shown.

category	σ_z [mm]
I_z	0.92 ± 0.02
II_z	0.67 ± 0.09
IV_z	0.70 ± 0.01

Table 6.2: Results of fitting a Gaussian function to the Δz-distribution for $\mathrm{DEP}_{\mathrm{simu}}$. The fit was done separately for category I_z ($\hat{\tau}_{ud} = +2$), II_z ($0 < \hat{\tau}_{ud} < +2$), and IV_z ($\hat{\tau}_{ud} = -2$).

Chapter 7

Comparison between simulation and data

To validate the simulation of mirror pulses, the distributions of mirror pulse parameters were compared between simulation and data. The method to reconstruct the position of single energy depositions in ϕ and z was applied to data. The resulting position distributions were compared to reconstructed and true Monte Carlo distributions.

7.1 Limitations of the Monte Carlo

The simulation described in Chapter 6 contains two fundamental simplifications, leading to some a priori differences between simulation and data:

- The energy depositions, hits, as created by MaGe are used to select events with energy depositions in only one segment. The selection in the simulation is thus based on the geometrical segment boundaries, since the drift of the charge carriers is not taken into account. In the data, the effective boundaries are reflected. Therefore, some simulated events are erroneously classified to have energy depositions in only one segment and some events that would have fallen into this category are lost.

- The pulse shapes are calculated for the barycenter of the hits. Only one pair of pointlike charge carriers is simulated. In reality, a superposition of the pulse shapes of the various components of a charge cloud with an extension of $\mathcal{O}$(mm) takes place.

These simplifications are justified for a first comparison in order to actually see whether they have an effect. This is necessary to determine the detail needed in the simulation. It should also be noted that the number of hits generated by MaGe is of $\mathcal{O}(10)$ for energy depositions around 1.5 MeV, while in reality $\mathcal{O}(500\,000)$ electron-hole pairs are created. It is a priori not clear whether this level of detail is sufficient to correctly describe the selection of events with energy depositions in only one segment based on a cut that allows only one segment with an energy above 20 keV.

7.2 Left and right mirror pulses

The method described in Sec. 4.2 was used to reconstruct the amplitudes of the left and right mirror pulses, A_l and A_r, for every event in the $\mathrm{DEP}_{\mathrm{simu},\phi}$, the $\mathrm{DEP}_{\mathrm{data},\phi}$, and the $\mathrm{DEP}_{\mathrm{BG},\phi}$ sample. The normalization of the amplitudes was such that the amplitude of the real pulse in the core of the DEP event was 1 and the mirror pulses were normalized to the core pulse. An amplitude, A, was considered reconstructable if it exceeded two times the noise level. The noise level was 0.0025, see Sec. 5.3.5. For every event, there were two possible amplitudes A, A_l and A_r. If one mirror pulse had a positive as well as a negative amplitude exceeding two times the noise level, A was defined as the one with the larger absolute value. The fraction of reconstructable A is denoted with a_ϕ. Subsequently, τ, with $\tau = \tau_l$ or τ_r, respectively, as defined in Chapter 4, was calculated for every reconstructable amplitude. For every event in which A_l and A_r could both be reconstructed, $\hat{\tau}_{lr}$ and α_{lr} were calculated according to their definition in Chapter 4. The fraction of these events is denoted with b_ϕ. With α_{lr}, the position in ϕ of the energy deposition, $\phi_{\mathrm{simu,rec}}$ and $\phi_{\mathrm{data,rec}}$ for $\mathrm{DEP}_{\mathrm{simu},\phi}$ and $\mathrm{DEP}_{\mathrm{data},\phi}$, respectively, was calculated using the method presented in Sec. 4.4.2. The method is only applicable if the event falls into one of the following categories:

I$_\phi$: $\hat{\tau}_{lr} = +2$,

II$_\phi$: $0 < \hat{\tau}_{lr} < +2$,

IIIa$_\phi$: $-2 < \hat{\tau}_{lr} \leq 0$ with $\tau_l = -1$, $-1 < \tau_r \leq +1$

IIIb$_\phi$: $-2 < \hat{\tau}_{lr} \leq 0$ with $\tau_r = -1$, $-1 < \tau_l \leq +1$

IV$_\phi$: $\hat{\tau}_{lr} = -2$

The fraction of events falling into one of the categories is denoted with c_ϕ. The values of a_ϕ, b_ϕ, and c_ϕ are listed in Table 7.1 for $\mathrm{DEP}_{\mathrm{simu},\phi}$, $\mathrm{DEP}_{\mathrm{data},\phi}$, and $\mathrm{DEP}_{\mathrm{BG},\phi}$.

	$\mathrm{DEP}_{\mathrm{simu},\phi}$	$\mathrm{DEP}_{\mathrm{data},\phi}$	$\mathrm{DEP}_{\mathrm{BG},\phi}$
a_ϕ	0.998 ± 0.003	0.933 ± 0.005	0.845 ± 0.083
b_ϕ	0.996 ± 0.005	0.869 ± 0.007	0.735 ± 0.106
c_ϕ	0.996 ± 0.005	0.868 ± 0.007	0.735 ± 0.106

Table 7.1: Values of a_ϕ, b_ϕ, and c_ϕ for $\mathrm{DEP}_{\mathrm{simu},\phi}$, $\mathrm{DEP}_{\mathrm{data},\phi}$, and $\mathrm{DEP}_{\mathrm{BG},\phi}$.

The efficiency a_ϕ is higher in the simulation than in the data. This is to be expected, because $\mathrm{DEP}_{\mathrm{data},\phi}$ also contains background events. The efficiency b_ϕ is consistent with a_ϕ^2 for $\mathrm{DEP}_{\mathrm{simu},\phi}$ and $\mathrm{DEP}_{\mathrm{data},\phi}$, indicating a random, independent loss of amplitudes.

The values of a_ϕ and b_ϕ are significantly smaller for $\mathrm{DEP}_{\mathrm{BG},\phi}$ than for $\mathrm{DEP}_{\mathrm{data},\phi}$. This can be attributed to the fact that these events are mainly multi-site events and the corresponding mirror pulse amplitudes differ in shape compared to those of single-site events, since they are the superposition of the individual mirror pulses. The efficiency b_ϕ is larger than a_ϕ^2 in this case, hinting at correlations.

In the simulation, the fraction of events with reconstructed α_{lr} that did not fall into one of the categories of $\hat{\tau}_{lr}$ was less than 0.1%. In the data, about 0.1% of the events with reconstructed α_{lr} could not be categorized. This is a very small fraction of events and thus it demonstrates that the categories in $\hat{\tau}_{lr}$ identified for simulated mirror pulses can also be used to categorize the measured mirror pulses.

The distributions of the parameters and reconstructed positions for $\mathrm{DEP}_{\mathrm{BG},\phi}$ were multiplied with the normalization factor, $R = 31$, determined in Sec. 5.3.6, and subtracted from those of $\mathrm{DEP}_{\mathrm{data},\phi}$ to account for the environmental background in the measurements.

The histograms of the distributions of A, τ, $\hat{\tau}_{lr}$, α_{lr}, and ϕ_{rec} were normalized to the respective number of entries. Those of A and τ can have two entries for every event. To account for the differences in the reconstruction efficiencies when comparing simulation and data, each distribution was multiplied with the respective efficiency factor from Table 7.1: the distribution of A and τ with a_ϕ, the distribution of $\hat{\tau}_{lr}$ and α_{lr} with b_ϕ, and the distribution of ϕ_{rec} with c_ϕ.

In Fig. 7.1, the distributions for (a) A, (b) τ, (c) $\hat{\tau}_{lr}$, (d) α_{lr}, and (e) ϕ_{rec} are shown for $\mathrm{DEP}_{\mathrm{simu},\phi}$, denoted by *simulation*, and the background subtracted $\mathrm{DEP}_{\mathrm{data},\phi}$ sample, referred to as *data*. The distribution of $\phi_{\mathrm{simu,true}}$ for $\mathrm{DEP}_{\mathrm{simu},\phi}$ is also depicted in Fig. 7.1(e).

In Fig. 7.1(a), the most striking difference between the distribution of A for the simulated and the measured mirror pulses is that the fraction of mirror pulses with $A > 0$ is much smaller in the simulation than in the data. There are also differences in the magnitude of A: the peak in the distribution with $A < 0$ in the simulation is shifted by ≈ 0.025 to larger $|A|$ compared to the data. While the shapes of the distributions for $A < 0$ look alike close to the peak area, the one of the simulated mirror pulses shows a too large tail. It reaches $A \approx -0.4$, while the distribution of the measured mirror pulses stops at $A \approx -0.25$. For events with $A > 0$, the peak in the distribution is at $A \approx 0.015$ in both cases. The tail of the distribution reaches $A \approx 0.35$ in the data and $A \approx 0.45$ in the simulation.

The lack of simulated mirror pulses with $A > 0$ is reflected in Fig. 7.1(b). The number of mirror pulses with $\tau = +1$ and the number of mirror pulses with $\tau = -1$ are approximately equal for the data, while in the simulation the mirror pulses with $\tau = -1$ outweigh the mirror pulses with $\tau = +1$ by a factor of 4. The entries per bin (width $= 0.02$) for $-1 < \tau < +1$ vary between 10^{-4} and 10^{-3} for the simulation as well as for the data. There are too many mirror pulses with τ close to $|\tau| = 1$ in the simulation.

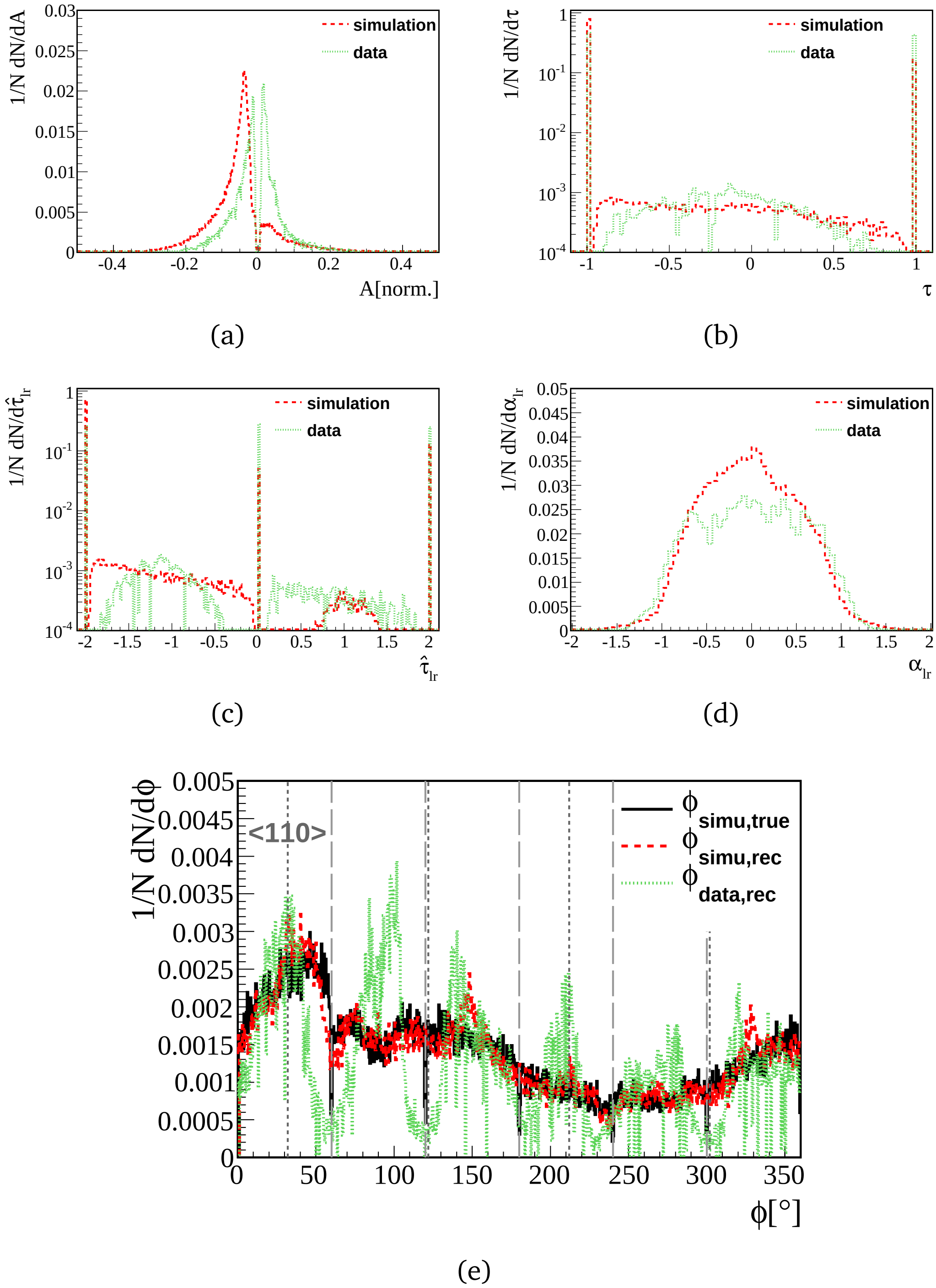

Figure 7.1: Distribution of (a) A, (b) τ, (c) $\hat{\tau}_{lr}$, (d) α_{lr}, and (e) ϕ_{rec} for simulation and data. The true position of the simulated events is also shown in (e). The positions of the segment boundaries and the crystal axes <110> are indicated in (e) with dashed and dotted lines, respectively.

As a consequence of the smaller fraction of mirror pulses with $\tau = +1$ in the simulation, also the fraction of events with $\hat{\tau}_{lr} = +2$ is smaller, see Fig. 7.1(c). Another noticeable difference is the fraction of events with $\hat{\tau}_{lr} = 0$, which is lower by almost one order of magnitude in the simulation. The distributions differ significantly for events with $|\hat{\tau}_{lr}| < 2$. It looks like the shapes were exchanged between positive and negative $\hat{\tau}_{lr}$.

The distributions of α_{lr} are depicted in Fig. 7.1(d). They agree well for events with $0.6 < |\alpha_{lr}| < 1.4$. The distributuion of the simulated events extends to $|\alpha_{lr}| \approx 1.6$, while in the data it ends at $|\alpha_{lr}| \approx 1.4$. The simulation produces a peak-like shape of the distribution, while the data have a plateau, i.e. there are too many events with small $|\alpha_{lr}|$ in the simulation.

In Fig. 7.1(e), the distributions of $\phi_{\mathrm{data,rec}}$ and $\phi_{\mathrm{simu,rec}}$ are plotted together with the true position in the simulation, $\phi_{\mathrm{simu,true}}$. The distributions of the simulated events are different from those depicted in Fig. 6.2(b), since events with real pulses in segments 3, 16, or 17 were not taken into account. Events for both simulation and data are reconstructed predominantly close to the segment center. In the simulation, this was discussed in Chapter 4. The effect is less pronounced in the simulation, reflecting the presence of events with large α_{lr}.

The areas around the segment boundaries that are depleted of events are much too narrow in the simulation. This could be due to the limitations of MaGe in truly representing the extension of an event; $\mathcal{O}(10)$ hits might not be enough.

Varying the simulated bandwidth within reasonable limits, i.e. between 8 MHz and 12 MHz, did not alter the distributions.

To further study the origin of the differences between simulated and measured mirror pulses, the categories of $\hat{\tau}_{lr}$, I_ϕ, II_ϕ, IIIa_ϕ, IIIb_ϕ, and IV_ϕ, were examined separately.

All distributions were normalized to the total number of entries in each histogram. No correction to account for the differences in efficiency was applied, since a_ϕ, b_ϕ, and c_ϕ can only be determined for the overall distributions. In all cases, *simulation* refers to the events of $\mathrm{DEP}_{\mathrm{simu},\phi}$, while the background subtracted distributions of $\mathrm{DEP}_{\mathrm{data},\phi}$ are denoted with *data*.

7.2.1 Category I_ϕ, $\hat{\tau}_{lr} = +2$

The fraction of all categorizable events in category I_ϕ is (29.0 ± 0.4)% in the data and (13.2 ± 0.1)% in the simulation. Events in category I_ϕ are located at small r, where the distance to the neighboring segment is small. The effect of the imperfect selection criteria and the influence of the charge cloud in the data therefore play an important role.

Figure 7.2 shows the distributions of A, α_{lr}, and $\phi_{\mathrm{simu,rec}}$, $\phi_{\mathrm{data,rec}}$, and $\phi_{\mathrm{simu,true}}$ for events in category I_ϕ for simulation and data.

The peak in A is found at $A \approx 0.045$ for the measured and at $A \approx 0.025$ for the simulated mirror pulses. The tail reaches $A \approx 0.3$ in the data and $A \approx 0.4$ in the

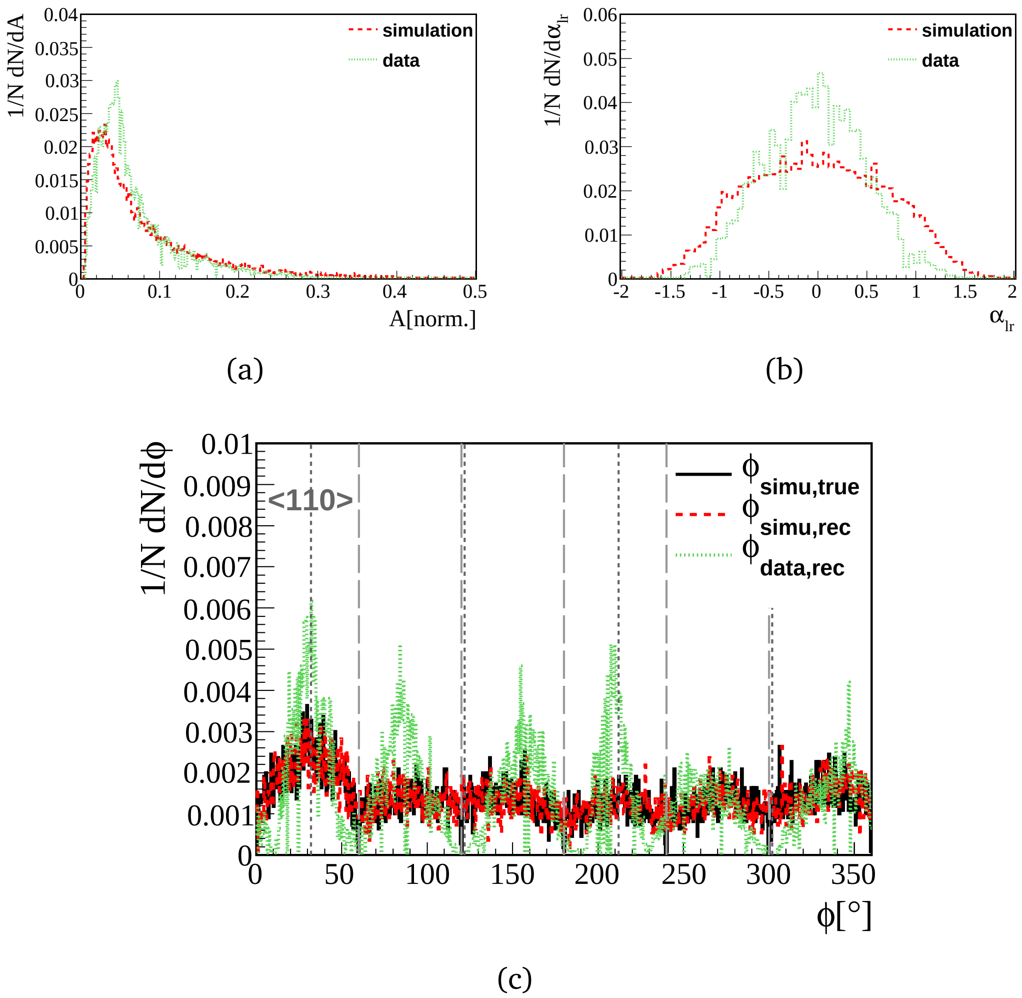

Figure 7.2: Distribution of (a) A, (b) α_{lr}, and (c) ϕ_{rec} for events in category I_{ϕ} ($\hat{\tau}_{lr} = +2$) for simulation and data. The true position of the simulated events is also shown in (c). The positions of the segment boundaries and the crystal axes <110> are indicated in (c) with dashed and dotted lines, respectively.

simulation.

The simulated charge carriers are pointlike. In reality, however, the pulses are caused by a charge cloud with a diameter of $\mathcal{O}$(mm). Close to a segment border, it is very likely that holes are collected by both segment electrodes. Therefore, the center of the charge cloud has to be at a certain distance from the border to result in a single-segment event. The pulses are superpositions of the contributions from the single charge carriers. Simulated events close to the segment borders cause the smallest and largest A. Such events with a single pair of charge carriers close to the boundary do not exist in the data. This explains why A takes on smaller as well as larger values in the simulation.

As a result, α_{lr} takes on values up to $|\alpha_{lr}| \approx 1.8$ in the simulation, while it is limited to $|\alpha_{lr}| \leq 1.5$ for the measured mirror pulses.

The agreement between $\phi_{\text{simu,rec}}$ and $\phi_{\text{simu,true}}$ is very good. However, the measured distribution has a much broader zone around the segment boundaries with almost no events reconstructed. As mentioned before, this is most probably due to the underlying simulated events being too localized and to the neglected influence of the charge cloud. At the core ($r = 5.5$ mm), the distance between the segment boundaries is ≈ 5.8 mm. If the center of the charge cloud is required to be at a distance of ≥ 1 mm from the left and right boundary, respectively, events can only cover $\approx 66\%$ of the range in ϕ and are thus concentrated in the segment center. At the outer surface ($r = 37.5$ mm), the distance between the segment boundaries is ≈ 39.3 mm. The allowed region extends over $\approx 95\%$ of the range in ϕ. Therefore, the effect should be much less evident for the events in category IV_ϕ, which are located close to the mantle.

In the data, the areas with no reconstructed events do not always coincide with the geometrical segment boundaries: the minima around 60° and 240° are shifted to the left, while those around 180° and 360° are shifted to the right. These shifts coincide with the results regarding the effective volumes of the segments deduced in Chapter 4. The simulation does not reproduce the shifts, because the events in the simulation were selected before the drift of the charge carriers.

Another observation is that the peaks in the distributions of $\phi_{\mathrm{data,rec}}$ are not exactly at the segment centers. Instead, they are shifted away from the crystal axes <110>. That is best seen around $\phi = 80°$ and $\phi = 160°$. The simulation reproduces the effect, but less pronounced. The crystal axes cause the bending of the drift trajectories of the charge carriers. In the data, the trajectories in a charge cloud can be different. Therefore, the charge cloud expands or shrinks, depending on the relative position to the crystal axes. The influence of the crystal axes is therefore expected to be more evident in the data.

All the effects described so far cannot explain why the simulation produces less than half of the events seen in the data in category I_ϕ. Taking into account the distribution of DEP events in r as depicted in Fig. 6.2(a), this indicates that the volume covered by this category extends to $r \approx 26$ mm in the data and to $r \approx 20$ mm in the simulation. The value for the simulation is in rough agreement with the limit of $r \approx 22$ mm from Chapter 4. The volume effect can be explained, if the drift velocities of the electrons and holes in the simulation are incorrect. This could be due to imperfect information used in the simulation concerning the impurity distribution or the mobilities of holes and electrons. If the electrons are simulated too slow or the holes are simulated too fast, the region with events in category I_ϕ shrinks in r, because the electrons are collected slower or the holes faster and the domination of the holes is limited to smaller r.

7.2.2 Category II_ϕ, $0 < \hat{\tau}_{lr} < +2$

The fractions of events in category II_ϕ are $(3.2 \pm 0.1)\%$ in the data and $(1.1 \pm 0.1)\%$ in the simulation. The three times larger fraction in the data can be due to the differences arising from the charge cloud. The small zone where this kind of events are located is

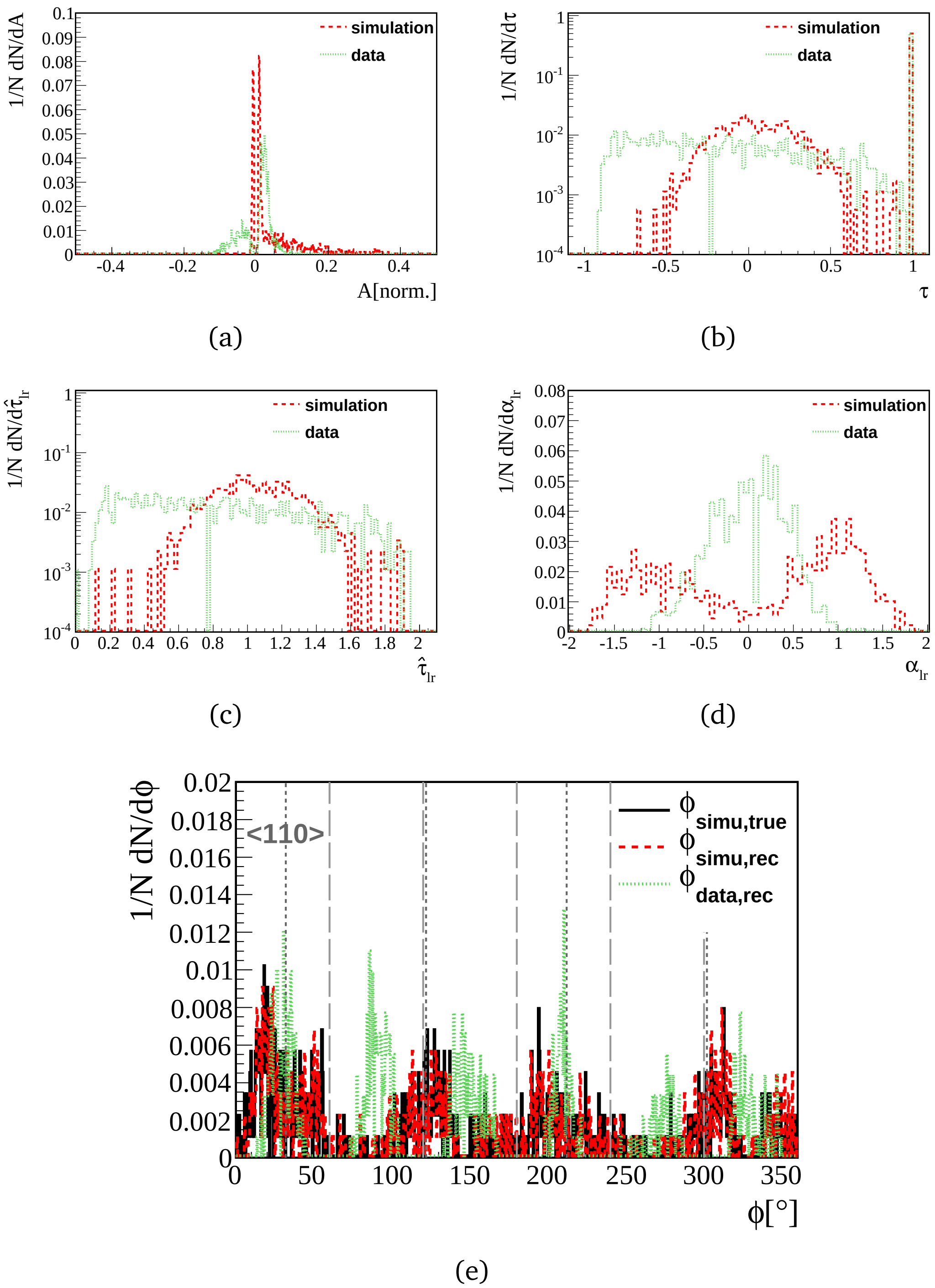

Figure 7.3: Distribution of (a) A, (b) τ, (c) $\hat{\tau}_{lr}$, (d) α_{lr}, and (e) ϕ_{rec} for events in category II$_\phi$ ($0 < \hat{\tau}_{lr} < +2$) for simulation and data. The true position of the simulated events is also shown in (e). The positions of the segment boundaries and the crystal axes <110> are indicated in (e) with dashed and dotted lines, respectively.

broadened by the size of the cloud. In addition, the zone has to be at larger r in the data, if the zone with events in category I$_\phi$ extends to larger r. This increases the size of the zone II_ϕ.

The simulation fails completely to predict the measured A distribution depicted in Fig. 7.3(a). In the data, there is only one peak at $A \approx 0.02$, while in the simulation two peaks can be disinguished: one at $A \approx -0.01$ and one at $A \approx 0.01$. The distribution of measured A with $A < 0$ extends down to $A \approx -0.12$, while the fraction of A with $A > 0.15$ is negligible. No A with $A < -0.03$ occured in the simulation. Instead, positive amplitudes up to $A \approx 0.4$ appeared.

The simulation correctly reproduces the fraction of mirror pulses with $\tau = +1$. For mirror pulses with $\tau < +1$, the measured mirror pulses reach down to $\tau = -1$ and the distribution increases with decreasing τ, while the distribution for the simulated pulses has a peak-like shape and is centered at $\tau \approx 0.1$.

Consequently, also the distributions of $\hat{\tau}_{lr}$ differ. The measured events reach over the entire range possible with the distribution increasing for decreasing $\hat{\tau}_{lr}$. The simulated distribution has a peak-like shape and is centered around $\hat{\tau}_{lr} \approx 1$.

The simulation completely fails to properly reproduce the distribution in α_{lr}. In the data, the distribution is centered around 0 and the range of α_{lr} is much smaller. In the simulation, two peaks at $\alpha_{lr} \approx -1.2$ and $\alpha_{lr} \approx 1.0$ exist.

Accordingly, $\phi_{\mathrm{simu,rec}}$ is mainly close to the segment boundaries, in accordance with $\phi_{\mathrm{simu,true}}$, while $\phi_{\mathrm{data,rec}}$ peaks close to the segment centers.

Two possibilities exist: The first one is that the volume where the events in category II_ϕ are located is different for simulation and data. In this case, the parameters deduced from the simulation are not applicable to reconstruct the position in the data. The second possibility is that the position reconstruction fails completely for events in category II_ϕ. Considering the limitations of the simulation, the first option is more likely.

7.2.3 Categories $\mathbf{IIIa}_\phi$ and $\mathbf{IIIb}_\phi$, $-2 < \hat{\tau}_{lr} \leq 0$

The fraction of events in category IIIa_ϕ is $(20.4 \pm 0.3)\%$ in the data and $(6.9 \pm 0.1)\%$ in the simulation, while the fraction of events in category IIIb_ϕ is $(18.6 \pm 0.3)\%$ in the data and $(6.3 \pm 0.1)\%$ in the simulation. According to the simulation, the events in these categories are located close to the segment boundaries, where the effects from the different selection criteria and the charge cloud are expected to be largest.

Figures 7.4 and 7.5 show the distributions of the mirror charge parameters for events in categories IIIa_ϕ and IIIb_ϕ for simulation and data.

For both categories, the simulated distribution of A does not describe the measurement at all. For the measured mirror pulses, most A are found around $A \approx 0.015$ and the distribution ranges from $A \approx -0.25$ to $A \approx 0.1$. For the simulated mirror pulses, the distributions peak at $A \approx -0.025$ and mirror pulses with $-0.3 < A < 0.4$ can be found, which is a wider range than in the data.

The number of mirror pulses with $\tau = +1$ is smaller in the simulation than in the data and deviations of the simulation from the data are also observed in the distributions of mirror pulses with $-1 < \tau < +1$.

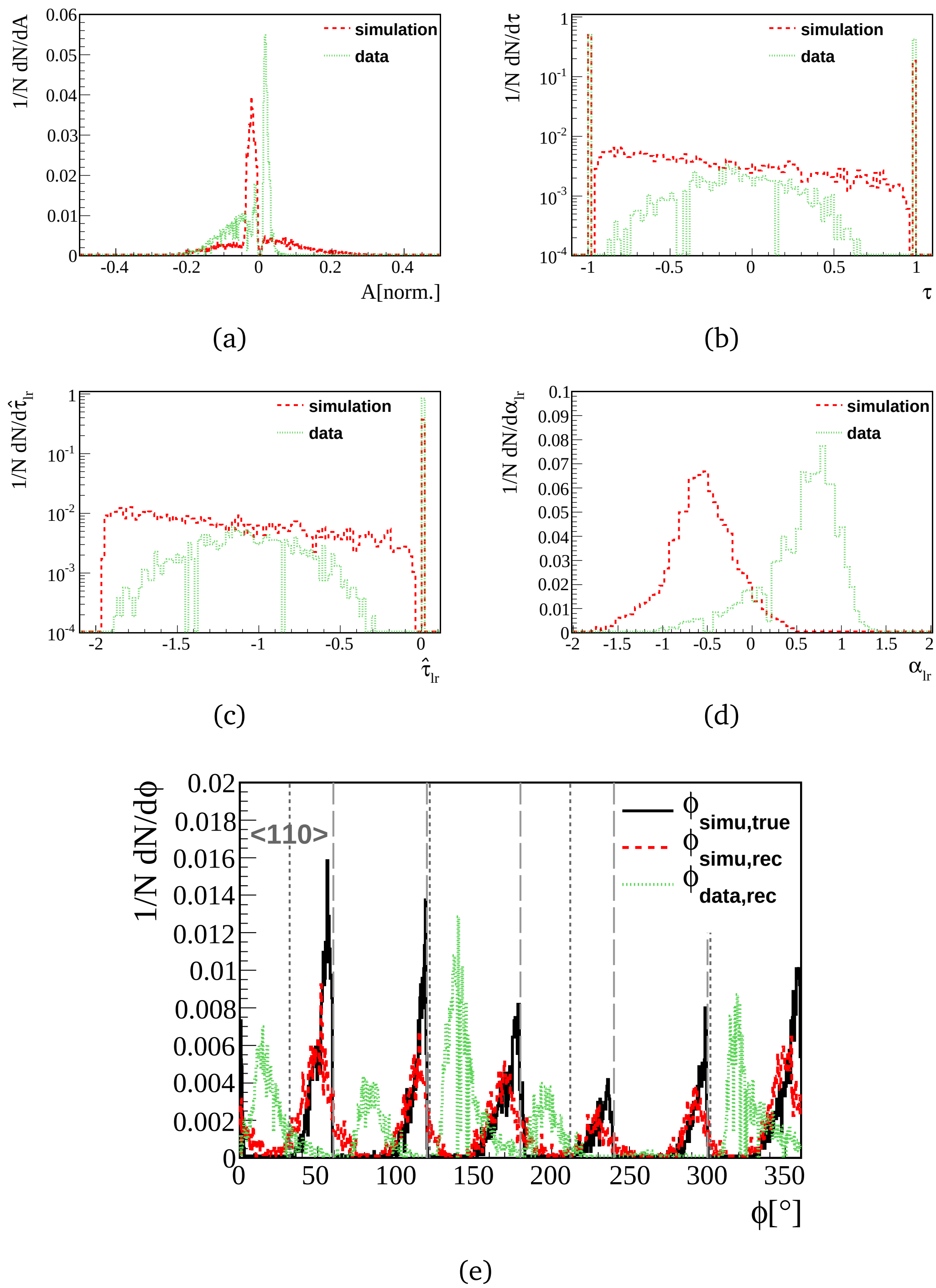

Figure 7.4: Distribution of (a) A, (b) τ, (c) $\hat{\tau}_{lr}$, (d) α_{lr}, and (e) ϕ_{rec} for events in category IIIa$_{\phi}$ ($-2 < \hat{\tau}_{lr} \leq 0$ and $\tau_l = -1$) for simulation and data. The true position of the simulated events is also shown in (e). The positions of the segment boundaries and the crystal axes <110> are indicated in (e) with dashed and dotted lines, respectively.

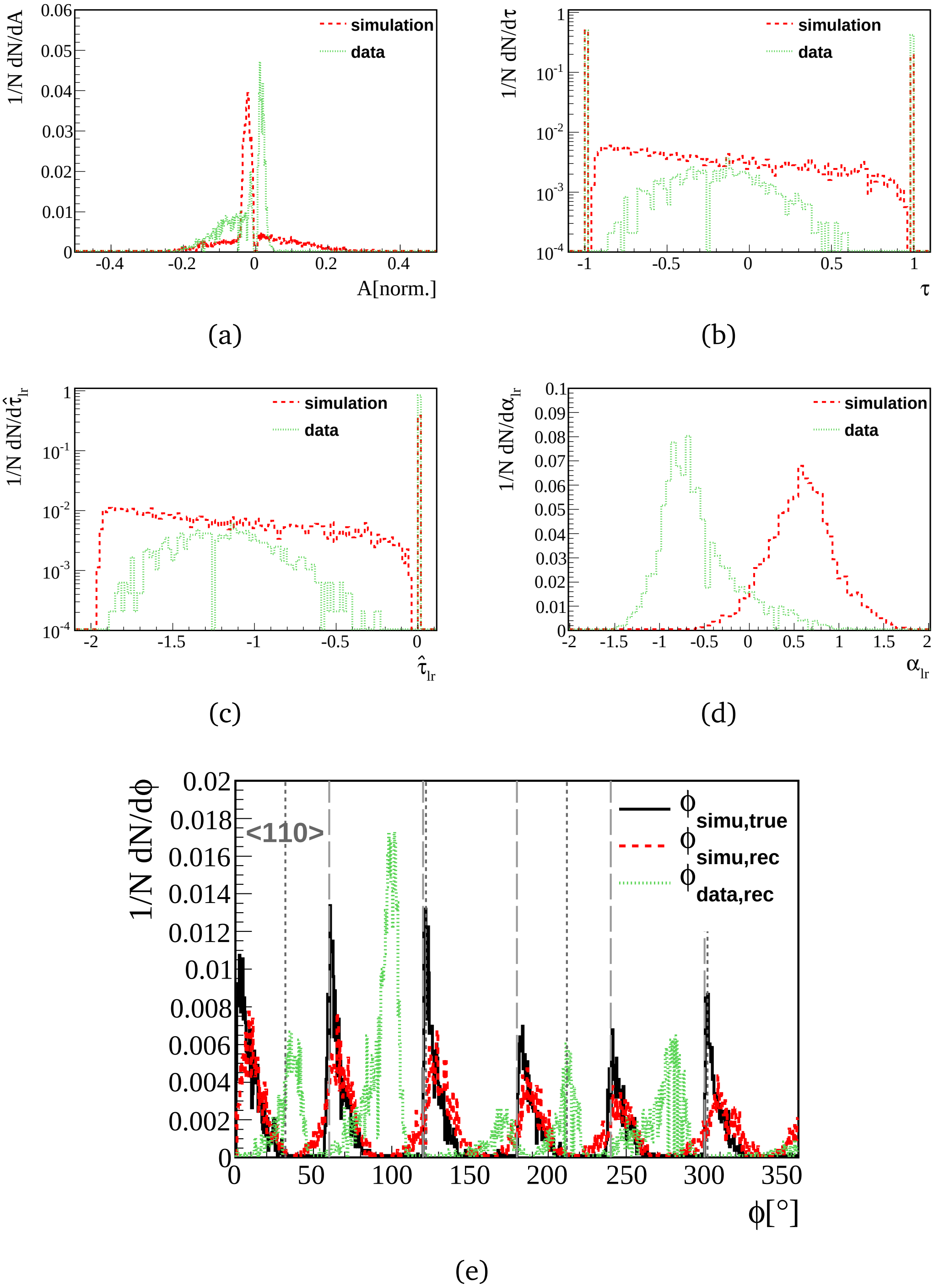

Figure 7.5: Distribution of (a) A, (b) τ, (c) $\hat{\tau}_{lr}$, (d) α_{lr}, and (e) ϕ_{rec} for events in category IIIb$_\phi$ ($-2 < \hat{\tau}_{lr} \leq 0$ and $\tau_r = -1$) for simulation and data. The true position of the simulated events is also shown in (e). The positions of the segment boundaries and the crystal axes <110> are indicated in (e) with dashed and dotted lines, respectively.

As a consequence, also the distributions in $\hat{\tau}_{lr}$ differ. The fraction of events with $\hat{\tau}_{lr} = 0$ is smaller in the simulation than in the data and the shape as well as the range of $\hat{\tau}_{lr}$ differ for $\hat{\tau}_{lr} < 0$.

The simulation of the α_{lr} distribution fails predictably. For measured events in category IIIa$_\phi$, the distribution is centered around $\alpha_{lr} \approx 0.7$, while it peaks at $\alpha_{lr} \approx -0.6$ in the simulation. For events in category IIIb$_\phi$, the distribution of the data peaks at $\alpha_{lr} \approx -0.75$ and the distribution of the simulation peaks at $\alpha_{lr} \approx 0.6$. It looks as if the simulated events were exchanged between category IIIa$_\phi$ and IIIb$_\phi$.

This is reflected in the $\phi_{\text{data,rec}}$ and $\phi_{\text{simu,rec}}$ distributions. The agreement between $\phi_{\text{simu,rec}}$ and $\phi_{\text{simu,true}}$ is, apart from deviations very close to the segment boundaries, good. The measured events are reconstructed in the segment center with a tendency to the left segment boundary for events in category IIIa$_\phi$ and a tendency to the right for events in category IIIb$_\phi$.

A comparison of the simulation to the data is not meaningful for these categories, as the selected events are different in the simulation and the data. As for category II$_\phi$, the simulation is not adequate to judge on the position reconstruction.

7.2.4 Category IV$_\phi$, $\hat{\tau}_{lr} = -2$

The fraction of all categorizable events in category IV$_\phi$ is (28.7 ± 0.4)% in the data and (72.6 ± 0.4)% in the simulation. The events are located at "large" r, where "large" obviously starts at much smaller r in the simulation than in reality.

The distribution of A, α_{lr}, and $\phi_{\text{simu,rec}}$, $\phi_{\text{data,rec}}$, and $\phi_{\text{simu,true}}$ for events in category IV$_\phi$ are shown in Fig. 7.6.

The shapes of the distributions of A in Fig. 7.6(a) look similar. However, the simulated distribution is shifted to larger $|A|$ and somewhat streched compared to the data. In the data, there is a maximum at $A \approx -0.015$ and no events with $A < -0.25$ are observed. In the simulation, the peak is located at $A \approx -0.04$ and the distribution reaches down to $A \approx -0.4$.

The distributions of α_{lr} agree well. The simulation shows a tendency to smaller $|\alpha_{lr}|$ compared to the data, making the distribution slightly narrower.

Also the agreement between $\phi_{\text{simu,rec}}$, $\phi_{\text{data,rec}}$, and $\phi_{\text{simu,true}}$ is good. All distributions follow the same pattern. The reason for the deviations of the distribution of $\phi_{\text{simu,rec}}$ from $\phi_{\text{simu,true}}$ is discussed in Sec. 4.4.2.

The simulated large $|A|$ have two possible explanations: The drift of a point charge instead of a charge cloud, as explained for category I$_\phi$, and the usage of wrong drift velocities. The mirror pulses are a superposition of the negative contribution from the electrons and the positive contribution from the holes. If the holes were simulated too fast or the electrons too slow, the influence of the holes was underestimated. This lead to too large simulated $|A|$ for the events in category IV$_\phi$. This could also explain the deviations for the distributions of α_{lr}. If the increase in $|A|$ with different drift velocities

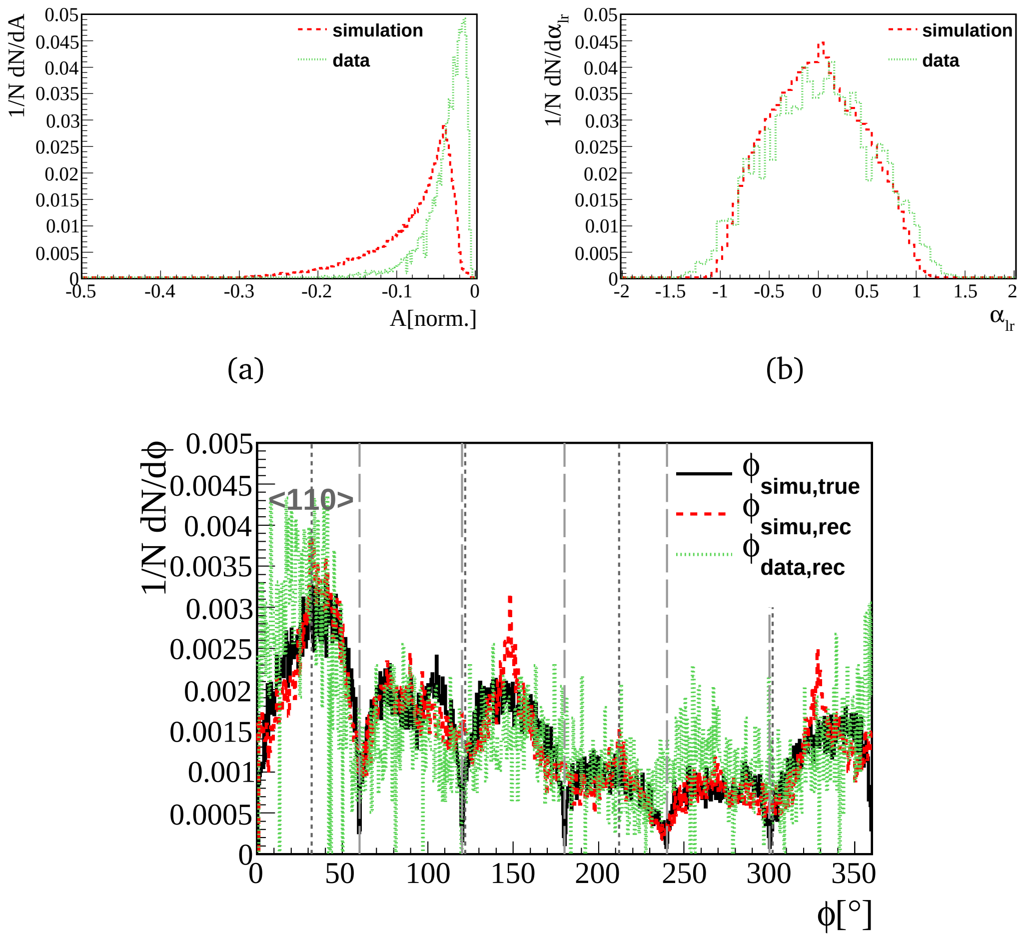

(c)

Figure 7.6: Distribution of (a) A, (b) α_{lr}, and (c) ϕ_{rec} for events in category IV$_\phi$ ($\hat{\tau}_{lr} = -2$) for simulation and data. The true position of the simulated events is also shown in (c). The positions of the segment boundaries and the crystal axes <110> are indicated in (c) with dashed and dotted lines, respectively.

is relatively smaller for the large mirror pulse in the closer neighboring segment than for the smaller mirror pulse in the distant neighboring segment, the resulting $|\alpha_{lr}|$ is too small.

The effect due to differences in the selection criteria for simulation and data is expected to be less pronounced for category IV$_\phi$. The events are located at large r, where the distance to the neighboring segment is in average larger than for small r. The fraction of events close to the boundaries, where the largest deviations of the simulation from the data are expected, is therefore small. This is evident in the better agreement between simulation and data compared to the other categories.

No peaks at the segment centers are observed in the data. This was anticipated in the discussion of category I$_\phi$. No shift away from the crystal axes <110> is evident, as this was the case for events from category I$_\phi$. This is again due to the fact that the events are located at large r, where the effect of the transversal anisotropy is smaller.

7.3 Up and down mirror pulses

The amplitudes were reconstructed for the up and down mirror pulses for all events in the $\mathrm{DEP}_{\mathrm{simu},z}$, the $\mathrm{DEP}_{\mathrm{data},z}$, and the $\mathrm{DEP}_{\mathrm{BG},z}$ sample. Again, the pulses were normalized to the amplitude corresponding to the charge of a DEP event. An amplitude, A, was considered reconstructable if it exceeded two times the noise level, with the noise level being 0.0025. For every event, there were two possible amplitudes A, A_u and A_d, for the up and down mirror pulse, respectively. If one mirror pulse had a positive as well as a negative amplitude exceeding two times the noise level, A was defined as the one with the larger absolute value. The fraction of reconstructable A is denoted with a_z. Subsequently, τ, with $\tau = \tau_u$ or τ_d, respectively, as defined in Chapter 4, was calculated for every reconstructable amplitude. For every event in which A_u and A_d could both be reconstructed, $\hat{\tau}_{ud}$ and α_{ud} were calculated according to their definition in Chapter 4. The fraction of these events is denoted with b_z. The position in z of the energy deposition, $z_{\mathrm{simu,rec}}$ and $z_{\mathrm{data,rec}}$, for $\mathrm{DEP}_{\mathrm{simu},z}$ and $\mathrm{DEP}_{\mathrm{data},z}$, respectively, was calculated using α_{ud} and the method presented in Sec. 4.4.3. To apply the method, the event had to fall into one of the following categories:

I$_z$: $\hat{\tau}_{ud} = +2$,

II$_z$: $0 < \hat{\tau}_{ud} < +2$,

IIIa$_z$: $-2 < \hat{\tau}_{ud} \leq 0$ with $\tau_u = -1$, $-1 < \tau_d \leq +1$

IIIb$_z$: $-2 < \hat{\tau}_{ud} \leq 0$ with $\tau_d = -1$, $-1 < \tau_u \leq +1$

IV$_z$: $\hat{\tau}_{ud} = -2$

The fraction of events falling into one of the categories is denoted with c_z. The values of a_z, b_z, and c_z for $\mathrm{DEP}_{\mathrm{simu},z}$, $\mathrm{DEP}_{\mathrm{data},z}$, and $\mathrm{DEP}_{\mathrm{BG},z}$ are listed in Table 7.2.

	$\mathrm{DEP}_{\mathrm{simu},z}$	$\mathrm{DEP}_{\mathrm{data},z}$	$\mathrm{DEP}_{\mathrm{BG},z}$
a_z	0.991 ± 0.007	0.932 ± 0.011	0.719 ± 0.139
b_z	0.982 ± 0.010	0.866 ± 0.014	0.438 ± 0.140
c_z	0.980 ± 0.010	0.866 ± 0.014	0.438 ± 0.140

Table 7.2: Values of a_z, b_z, and c_z for $\mathrm{DEP}_{\mathrm{simu},z}$, $\mathrm{DEP}_{\mathrm{data},z}$, and $\mathrm{DEP}_{\mathrm{BG},z}$.

The efficiency a_z is higher in the simulation than in the data. This was expected due to the background events that are contained in $\mathrm{DEP}_{\mathrm{data},z}$. The efficiency b_z is consistent with a_z^2 for $\mathrm{DEP}_{\mathrm{simu},z}$ and $\mathrm{DEP}_{\mathrm{data},z}$, indicating a random, independent loss of amplitudes. The values of a_z and b_z are much smaller for $\mathrm{DEP}_{\mathrm{BG},z}$. This is not surprising, since the event topologies of the background events are different.

The fraction of events with reconstructed α_{ud} that did not fall into one of the categories of $\hat{\tau}_{ud}$ was 0.2% in the simulation and smaller than 0.1% in the data, demonstrating the adequacy of the classification according to $\hat{\tau}_{ud}$ also in the data.

The distributions of the parameters and reconstructed positions for $\mathrm{DEP}_{\mathrm{BG},z}$ were multiplied with the normalization factor, $R = 31$, defined in Sec. 5.3.6, and subtracted from those of $\mathrm{DEP}_{\mathrm{data},z}$ to account for the environmental background in the measurements.

The histograms of the distributions of A, τ, $\hat{\tau}_{ud}$, α_{ud}, and z_{rec} were normalized to the respective number of entries. Those of A and τ can have two entries for every event. The differences in the reconstruction efficiencies were taken into account by multiplying each distribution with the respective efficiency factor from Table 7.2: the distribution of A and τ with a_z, the distribution of $\hat{\tau}_{ud}$ and α_{ud} with b_z, and the distribution of z_{rec} with c_z.

In Fig. 7.7, the distributions for (a) A, (b) τ, (c) $\hat{\tau}_{ud}$, (d) α_{ud}, and (e) z_{rec} are shown. *Simulation* denotes the distributions for $\mathrm{DEP}_{\mathrm{simu},z}$, and *data* those for $\mathrm{DEP}_{\mathrm{data},z}$ after the subtraction of background. In Fig. 7.7(e), also the distribution of the true position in the simulation, $z_{\mathrm{simu,true}}$, is shown.

The shape of the distributions in A, depicted in Fig. 7.7(a), is similar to the one observed for the left and right mirror pulses. Again, there are not enough pulses with $A > 0$ in the simulation and for $A < 0$ the peak position is shifted by ≈ 0.015 towards larger $|A|$. The shift is smaller than in the case of the left and right mirror pulses. For events with $A > 0$, only one broad peak at $A \approx 0.025$ is observed in the data. The simulated distribution, however, shows a narrow peak at $A \approx 0.01$ and a smaller, broader one at $A \approx 0.03$. A reaches values up to $A \approx 0.65$ in the simulation, but only up to $A \approx 0.3$ in the data.

Also the situation for τ, shown in Fig. 7.7(b), is compatible to the one for the left and right mirror pulses. There are too many mirror pulses with $\tau = +1$ in the simulation. The entries per bin (width $= 0.02$) with $-1 < \tau < +1$ vary between 10^{-4} and 10^{-3} for the data as well as for the simulation. The number of mirror pulses with τ close to $|\tau| = 1$ is larger in the simulation than in the data.

Consequently, also the fraction of events with $\hat{\tau}_{ud} = +2$ is smaller in the simulation than in the data. The distributions are shown in Fig. 7.7(c). The event density at $\hat{\tau}_{ud} = 0$ in the simulation is smaller by almost one order of magnitude compared to the data. There are almost no events with $0 < \hat{\tau}_{ud} < +2$ in the simulation, while they appear in the data.

The distributions of α_{ud} are depicted in Fig. 7.7(d). The simulation describes the measured distribution well. The simulated distribution is slightly shifted towards larger α_{ud}. While the measured α_{ud} take on values up to $|\alpha_{ud}| \approx 1.6$, the simulated α_{ud} have values up to $|\alpha_{ud}| \approx 2$. There are slightly too many events with small $|\alpha_{ud}|$ in the simulation.

The distributions of $z_{\mathrm{data,rec}}$, $z_{\mathrm{simu,rec}}$, and $z_{\mathrm{simu,true}}$ are shown in Fig. 7.7(e). The agreement between $z_{\mathrm{simu,rec}}$ and $z_{\mathrm{simu,true}}$ is good. The areas close to the segment boundaries where no events can be found are much too narrow in the simulation. This could be accounted for by too small charge clouds generated by MaGe.

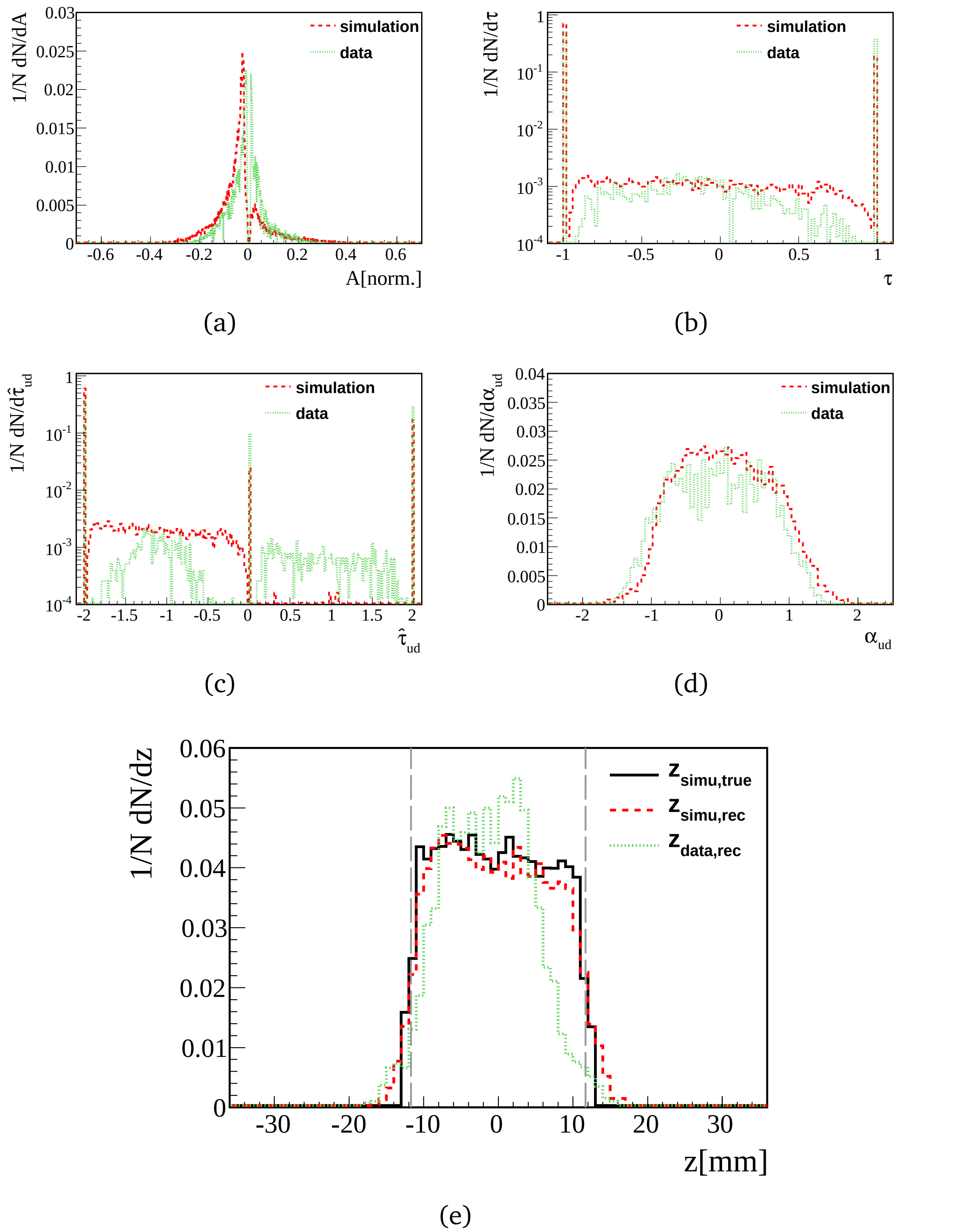

Figure 7.7: Distribution of (a) A, (b) τ, (c) $\hat{\tau}_{ud}$, (d) α_{ud}, and (e) z_{rec} for simulation and data. The true position of the simulated events is also shown in (e). The positions of the segment boundaries are indicated in (e).

A change in the simulated bandwidth within reasonable limits, i.e. between 8 MHz and 12 MHz, did not show an effect on the distributions.

To further analyze the deviations of the simulation from the data, the events belonging to the categories I_z, II_z, IIIa_z, IIIb_z, and IV_z were examined separately.

All distributions were normalized to the total number of entries in each histogram. Since a_z, b_z, and c_z cannot be determined for the single categories, no correction was applied to account for the differences in efficiency. *Simulation* describes the events of $\mathrm{DEP}_{\mathrm{simu},z}$, while *data* refers to the background subtracted distributions of $\mathrm{DEP}_{\mathrm{data},z}$.

7.3.1 Category I_z, $\hat{\tau}_{ud} = +2$

The fraction of events in category I_z of all categorized events is $(33.8 \pm 0.8)\%$ in the data and $(17.1 \pm 0.3)\%$ in the simulation.

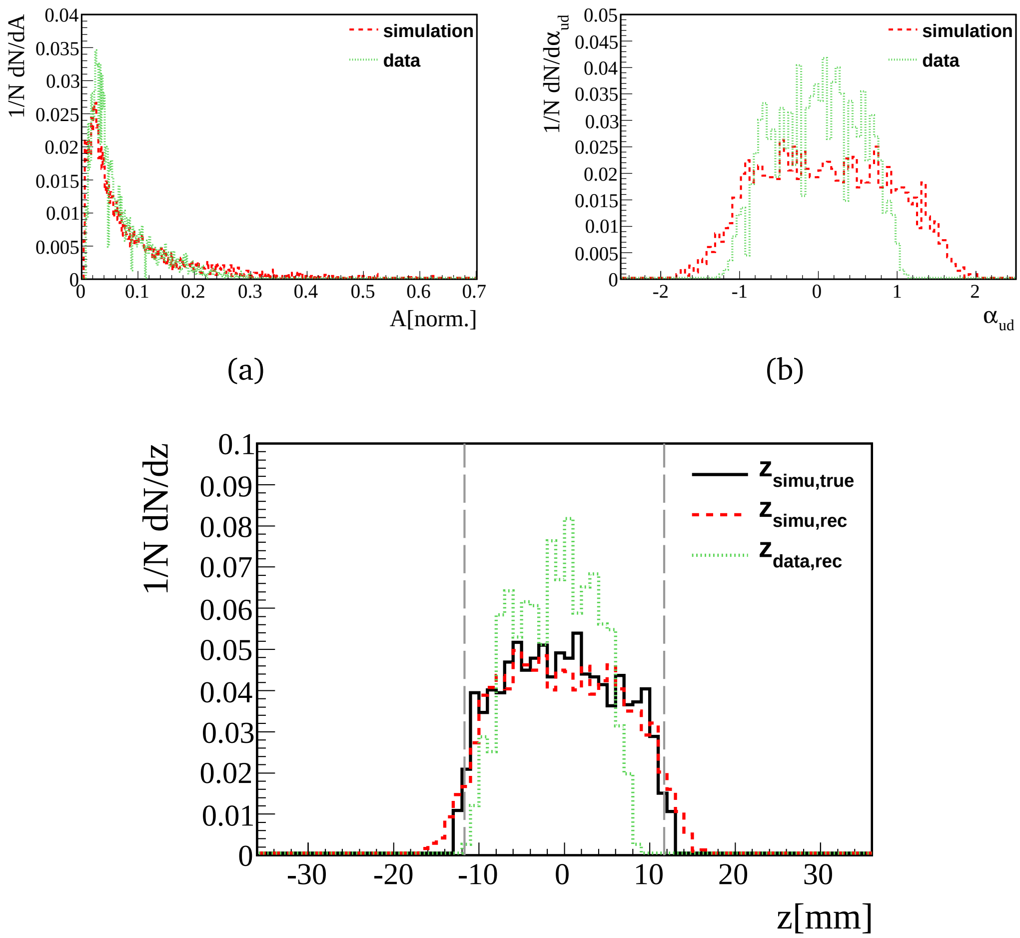

(a) (b) (c)

Figure 7.8: Distribution of (a) A, (b) α_{ud}, and (c) z_{rec} for events in category I_z ($\hat{\tau}_{ud} = +2$) for simulation and data. The true position of the simulated events is also shown in (c). The positions of the segment boundaries are indicated in (c).

In Fig. 7.8, the distributions of A and α_{ud} for simulation and data and $z_{\mathrm{simu,rec}}$, $z_{\mathrm{data,rec}}$, and $z_{\mathrm{simu,true}}$ are shown for events in category I_z.

Both distributions of A have a peak at $A \approx 0.025$. The range of A reaches from $A \approx 0.008$ to $A \approx 0.3$ in the data, while it reaches from $A \approx 0.005$ to $A \approx 0.7$ in the simulation. The range is thus too large in the simulation. This can be accounted for by the lack of the effects due to the charge cloud in the simulation, as explained for category I_ϕ.

Again, too large $|\alpha_{ud}|$ occur in the simulation. The measured α_{ud} fall into $-1.3 \leq \alpha_{ud} \leq 1.1$, while the simulated α_{ud} cover the range $-2 < \alpha_{ud} < 2$.

The simulated events cover the full range in z, while the measured events are only reconstructed away from the boundaries. The reconstructed positions of the measured events display a broader empty zone close to the upper segment boundary than close to the lower one. This effect is not present in the simulation. The fact that a fraction of the simulated events is reconstructed with too large $|z|$ was anticipated in Sec. 4.4.3.

The simulation assumes a homogeneous impurity density, ρ_{imp}. It is known from the manufacturer's specifications that this is not true in reality. The impurity densities at the top, $\rho_{\mathrm{imp,top}}$, and the bottom, $\rho_{\mathrm{imp,bottom}}$, of the detector are specified to be $\rho_{\mathrm{imp,top}} \approx 2.2 \cdot \rho_{\mathrm{imp,bottom}}$. If this is also reflected in the local densities, $\rho_{\mathrm{imp,up}} > \rho_{\mathrm{imp,down}}$, the electrons and holes are deflected to the bottom and top, respectively. Therefore, the data contain events where energy was geometrically deposited in the bottom layer, but the holes were collected by one of the electrodes in the middle layer. Thus the effective boundaries of the segments are shifted and the distribution of $z_{\mathrm{data,rec}}$ just reflects this.

Wrong assumptions on the drift velocities in the simulation can explain why the simulation produces only half of the events seen in category I_z. The argument is analog to the one for category I_ϕ.

7.3.2 Category II_z, $0 < \hat{\tau}_{ud} < +2$

The fraction of events in category II_z is $(5.7 \pm 0.3)\%$ in the data and $(0.2 \pm 0.1)\%$ in the simulation. The difference can be accounted for by the fact that the transition zone from category I_z to IV_z, where these events appear, is broadened by the size of the charge cloud. In addition, the size of the zone II_z is increased, since it has to be at larger r in the data, if the zone of category I_z extends to larger r.

Only 45 events fall into this category in the simulation. Therefore, the statistical significance of the simulation is limited.

The simulation seems to reproduce the trends of the measured A distribution as depicted in Fig. 7.9(a), but favors too small $|A|$.

The simulated τ distribution, shown in Fig. 7.9(b), lacks entries with $\tau < -0.5$.

However, the simulated $\hat{\tau}_{ud}$ distribution, see Fig. 7.9(c), agrees reasonably well with the one for the data.

Figure 7.9(d) shows the distributions of α_{ud}. The distribution of α_{ud} in the data exhibits two peaks, one at $\alpha_{ud} \approx -0.6$, the other one at $\alpha_{ud} \approx 0.6$. No distinct shape

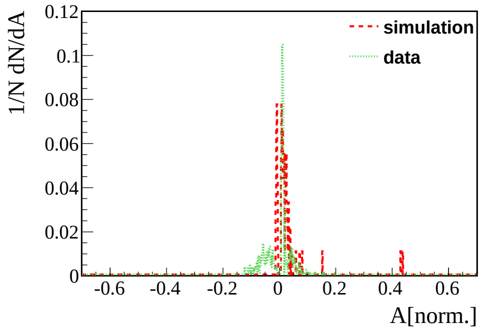

(a)

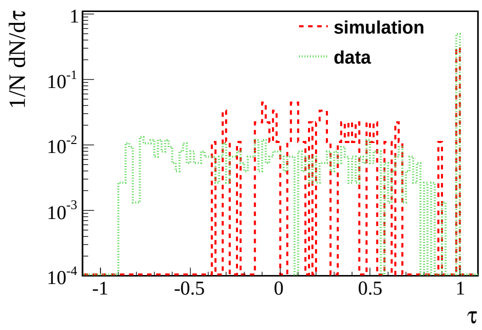

(b)

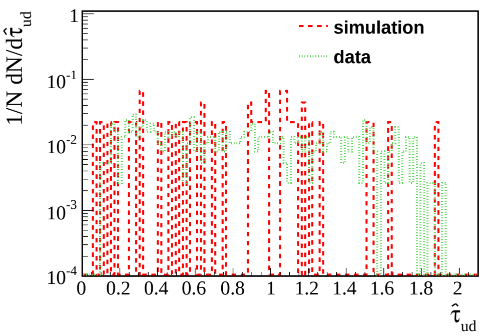

(c)

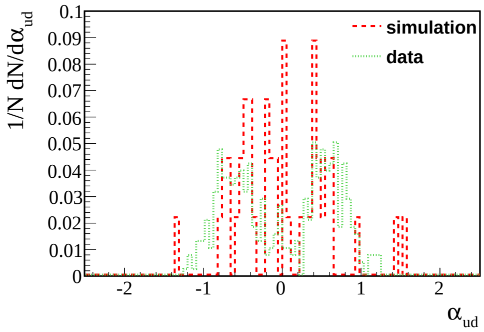

(d)

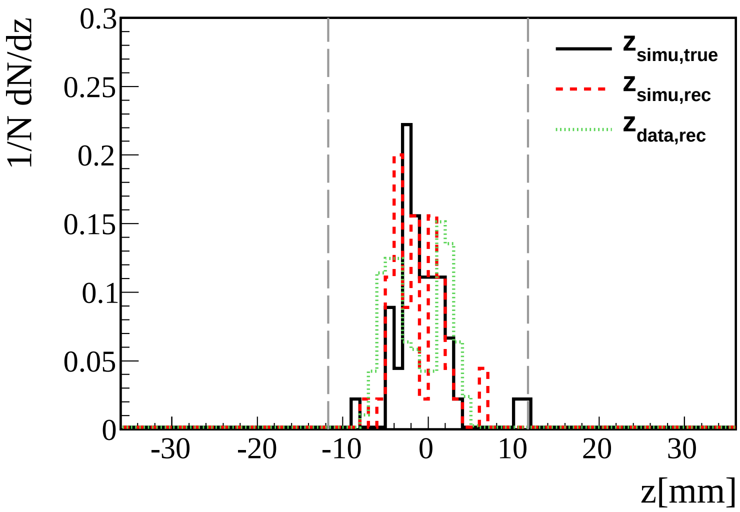

(e)

Figure 7.9: Distribution of (a) A, (b) τ, (c) $\hat{\tau}_{ud}$, (d) α_{ud}, and (e) z_{rec} for events in category II_z ($0 < \hat{\tau}_{ud} < +2$) for simulation and data. The true position of the simulated events is also shown in (e). The positions of the segment boundaries are indicated in (e).

can be identified for the simulation due to the limited statistics.

In Fig. 7.9(e), the distribution of $z_{\text{data,rec}}$ shows two peaks at $z \approx -4$ mm and $z \approx$

2 mm. This seems to be reflected in $z_{\text{simu,rec}}$, even though it is not true for $z_{\text{simu,true}}$.

Due to the limited statistics in the simulation, no further conclusion can be drawn.

7.3.3 Categories IIIa$_z$ and IIIb$_z$, $-2 < \hat{\tau}_{ud} \leq 0$

The fraction of events in category IIIa$_z$ is (8.2 ± 0.4)% in the data and (8.4 ± 0.2)% in the simulation, while the fraction of events in category IIIb$_z$ is (8.3 ± 0.4)% in the data and (13.1 ± 0.3)% in the simulation. According to the simulation, the events are located in the vicinity of the segment boundaries. Therefore, the neglect of the size of the charge cloud plays a role. Also the differences in the event selection are expected to have large effects, if indeed the effect discussed in Sec. 7.3.1 is sizeable, i.e. events migrate across the segment boundaries due to the gradient in ρ_{imp}. In this case, the events falling into the categories IIIa$_z$ and IIIb$_z$ could be at different positions in the simulation and the data, like for categories IIIa$_\phi$ and IIIb$_\phi$.

Figures 7.10 and 7.11 compare the distributions of the mirror charge parameters for events in category IIIa$_z$ and IIIb$_z$, respectively.

In both cases, the simulation does not at all reproduce the distribution in A. The deviations resemble the ones observed for categories IIIa$_\phi$ and IIIb$_\phi$. In the data, the distributions show large peaks at $A \approx 0.01$ and small peaks at $A \approx -0.01$ and extend from $A \approx -0.25$ to $A \approx 0.02$. The distributions of the simulated mirror pulses peak at $A \approx -0.02$ and range from $A \approx -0.35$ to $A \approx 0.35$ for the case of category IIIa$_z$ and $A \approx -0.4$ to $A \approx 0.4$ for the case of category IIIb$_z$, covering too large a range.

The event density at $\tau = +1$ is smaller by almost one order of magnitude in the simulation. The simulation predicts a flat density distribution for $-1 < \tau < +1$, which is not observed in the data.

The deviations of the simulation are also reflected in the distribution of $\hat{\tau}_{ud}$. The density of events at $\hat{\tau}_{ud} = 0$ is smaller by almost one order of magnitude in the simulation and the shape as well as the range in $\hat{\tau}_{ud}$ differ significantly.

The distributions in α_{ud} and z for IIIa$_z$ and IIIb$_z$ show the same phenomenon as for IIIa$_\phi$ and IIIb$_\phi$. The shapes seem exchanged. This is consistent with an event migration across the geometrical boundary as discussed for category I$_z$. The migrated events are then treated with the wrong set of parameters. No conclusion can thus be drawn on the position reconstruction.

The simulation predicts different fractions of events in category IIIa$_z$ and category IIIb$_z$. This is due to the fact that events in category IIIb$_z$ are located close to the lower boundary, where the fraction of total events is larger due to the position of the source. The fact that the difference vanishes in the data again points towards the fact that the events in the data are not located in the same region as in the simulation.

7.3.4 Category IV, $\hat{\tau}_{ud} = -2$

The fraction of categorizable events that fall into category IV$_z$ is (44.0 ± 0.9)% in the data and (61.1 ± 0.7)% in the simulation. The events are localized at “large” r, where

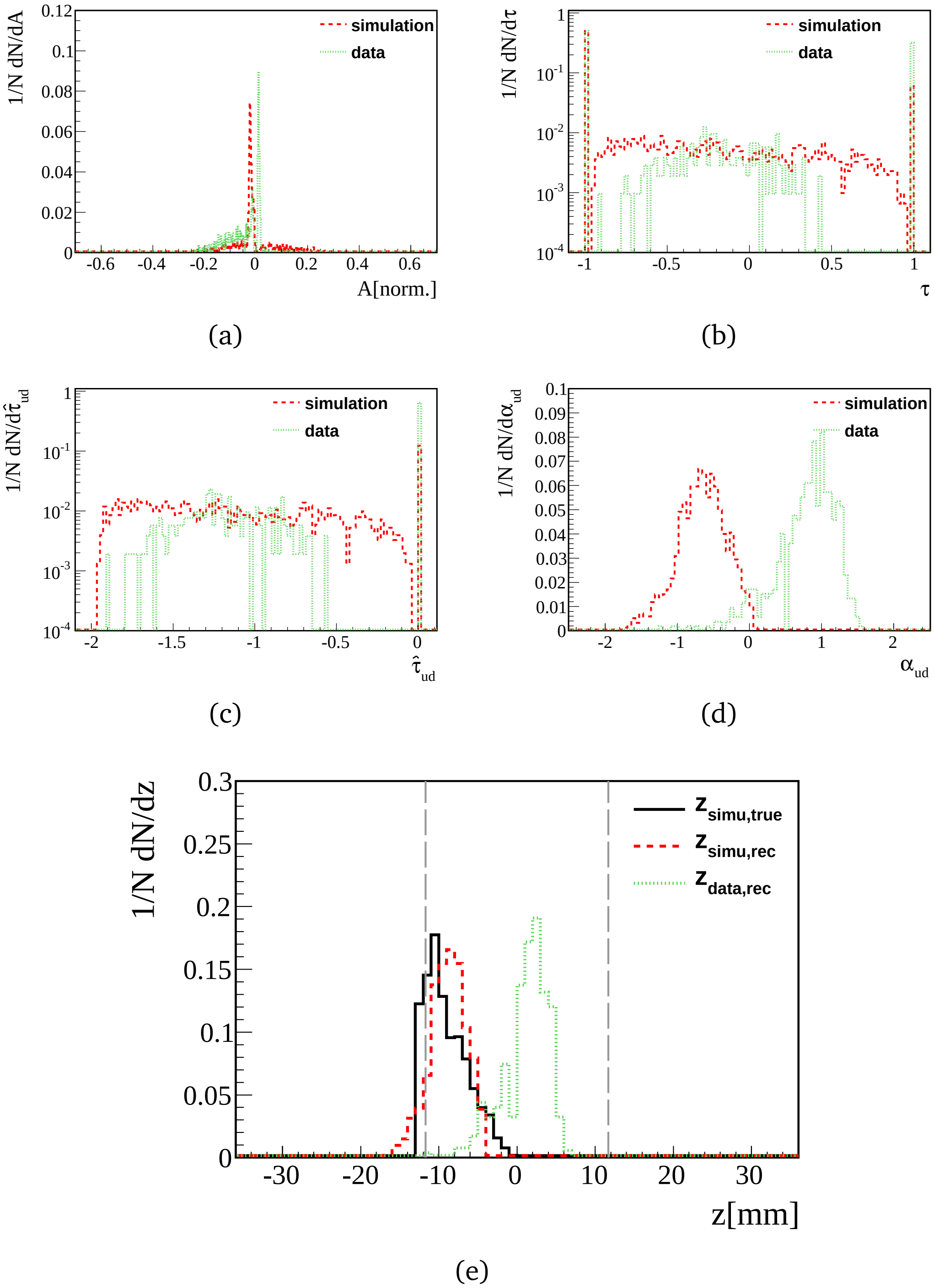

Figure 7.10: Distribution of (a) A, (b) τ, (c) $\hat{\tau}_{ud}$, (d) α_{ud}, and (e) z_{rec} for events in category IIIa_z ($-2 < \hat{\tau}_{ud} \leq 0$ and $\tau_u = -1$) for simulation and data. The true position of the simulated events is also shown in (e). The positions of the segment boundaries are indicated in (e).

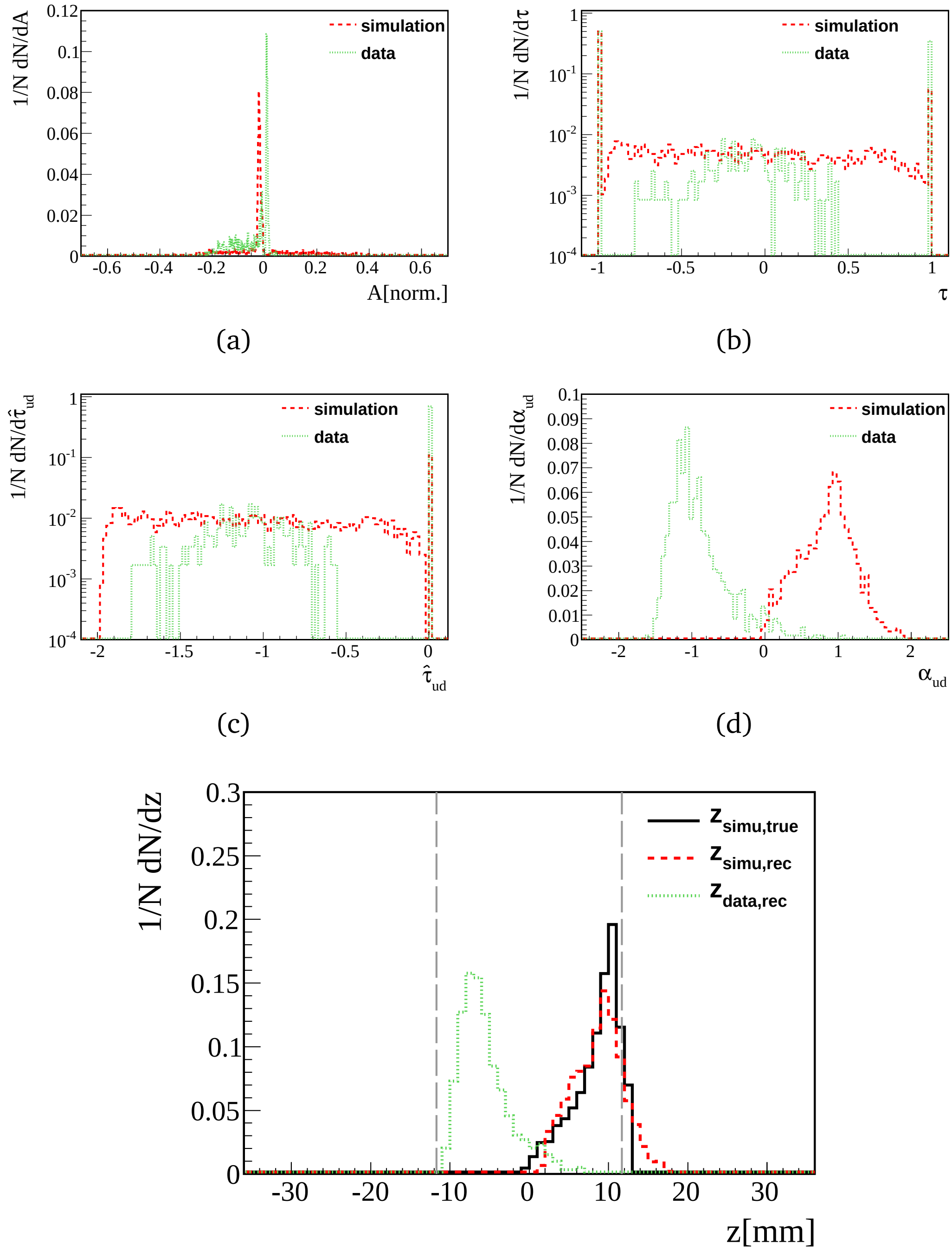

(e)

Figure 7.11: Distribution of (a) A, (b) τ, (c) $\hat{\tau}_{ud}$, (d) α_{ud}, and (e) z_{rec} for events in category IIIb$_z$ ($-2 < \hat{\tau}_{ud} \leq 0$ and $\tau_d = -1$) for simulation and data. The true position of the simulated events is also shown in (e). The positions of the segment boundaries are indicated in (e).

"large" is smaller in the simulation than in reality, as was explained previously.

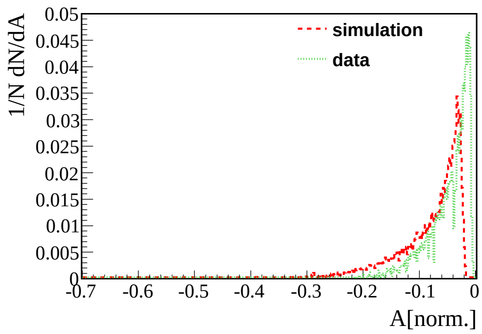

(a)

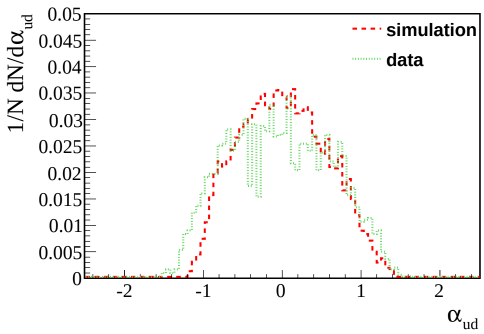

(b)

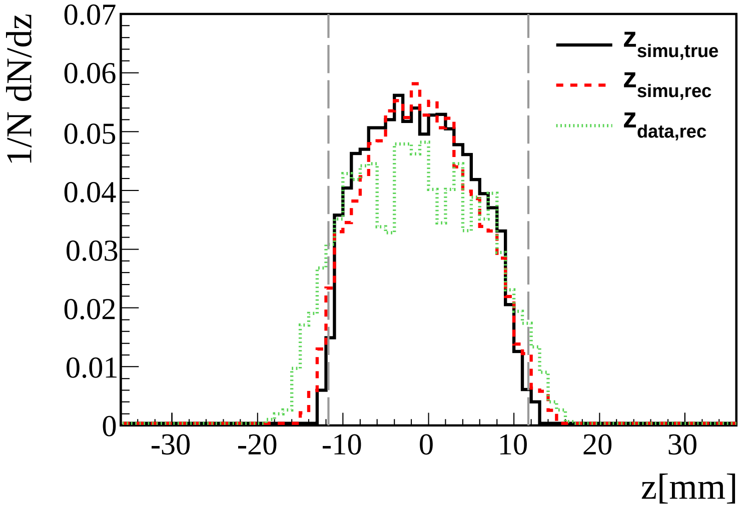

(c)

Figure 7.12: Distribution of (a) A, (b) α_{ud}, and (c) z_{rec} for events in category IV$_z$ ($\hat{\tau}_{ud} = -2$) for simulation and data. The true position of the simulated events is also shown in (c). The positions of the segment boundaries are indicated in (c).

The distributions of A, α_{ud}, and $z_{\text{simu,rec}}$, $z_{\text{data,rec}}$, and $z_{\text{simu,true}}$ for events in category IV$_z$ are shown in Fig. 7.12.

In the data, the distribution peaks at $A \approx -0.015$, and ranges down to $A \approx -0.25$. Even though the shape of the distribution looks similar in the simulation, it is stretched and shifted towards larger $|A|$ compared to the one in the data. The peak is at $A \approx -0.03$ and the smallest values reached are $A \approx -0.5$. This is as observed for category IV$_\phi$.

The simulated α_{ud} distribution describes the data well. A small deviation is observed at $\alpha_{ud} < -1$.

The lack of small values of α_{ud} is reflected in a lack of events reconstructed with $z < -10\,\text{mm}$ in the simulation. This is compatible with the shift of the effective segment boundaries as discussed for category I$_z$.

The distributions of $z_{\mathrm{simu,rec}}$ and $z_{\mathrm{simu,true}}$ are slightly narrower than the distribution of $z_{\mathrm{data,rec}}$. As mentioned in the case of category IV_ϕ, the simulated large $|A|$ can be caused by two effects: The drift of a point charge instead of a charge cloud and the usage of wrong drift velocities. The latter effect can also account for the fact that the simulated distribution of α_{ud}, and consequently also the distribution of $z_{\mathrm{simu,rec}}$, is too narrow: If in the simulation the increase in $|A|$ with different drift velocities is relatively smaller for the large mirror pulse in the closer neighboring segment than for the smaller mirror pulse in the distant neighboring segment, the resulting $|\alpha_{ud}|$ is too small.

7.4 Summary on the comparison between data and simulation

The simulation reproduces the main feature of the mirror pulses: that they are positive at small r close to the core (categories I_ϕ and I_z) and negative at large r close to the mantle (categories IV_ϕ and IV_z). The simulation also correctly predicts a complicated transition region at medium r (categories II_ϕ and II_z) and complications close to the segment boundaries (categories IIIa_ϕ, IIIb_ϕ and IIIa_z, IIIb_z).

The agreement between data and simulation is good for events in categories I_ϕ (I_z) and IV_ϕ (IV_z). However, the fraction of events falling into category I_ϕ (I_z) is with $(13.2 \pm 0.1)\%$ ($(17.1 \pm 0.3)\%$) significantly smaller in the simulation than in the data, where the fraction is $(29.0 \pm 0.4)\%$ ($(33.8 \pm 0.8)\%$). This indicates that the inner volume where mirror pulses are positive is too small in the simulation. As a result, the transition zone is at too small r in the simulation and the zone with negative mirror pulses is too large. This is reflected in the fraction of events in category IV_ϕ (IV_z), which is $(72.6 \pm 0.4)\%$ ($(61.1 \pm 0.7)\%$) in the simulation and $(28.7 \pm 0.4)\%$ ($(44.0 \pm 0.9)\%$) in the data.

The fraction of events in categories I_ϕ, II_ϕ, IIIa_ϕ, IIIb_ϕ, and IV_ϕ for simulation and data are summarized in Table 7.3. Also listed are the corresponding fractions of the volume covered by each category. The values were estimated taking into account the distribution of DEP events in r, depicted in Fig. 6.2(a), and assuming a geometrical distribution of the events of the different categories as in the simulation, see Fig. 4.6.

The fact that the transition zone is simulated at the wrong r causes the parameters determined for the position reconstruction for this category to be invalid for the data. The simplifications in the simulation around the segment boundaries also cause the parameters determined for this region to be invalid. However, events falling into these categories can clearly be identified and the position reconstruction can be used for the events in categories I_ϕ, I_z, IV_ϕ, and IV_z.

The overall agreement between data and simulation is better for the case of the up and down mirror pulses than for the case of the left and right mirror pulses, since there are no effects due to the transversal anisotropy.

The discrepancies between simulated and measured mirror pulses may be due to

	fraction of events		fraction of volume	
category	data	simulation	data	simulation
I_ϕ	$(29.0 \pm 0.4)\%$	$(13.2 \pm 0.1)\%$	47%	26%
II_ϕ	$(3.2 \pm 0.1)\%$	$(1.1 \pm 0.1)\%$	3.5%	1.7%
IIIa_ϕ	$(20.4 \pm 0.3)\%$	$(6.9 \pm 0.1)\%$	15%	5.9%
IIIb_ϕ	$(18.6 \pm 0.3)\%$	$(6.3 \pm 0.1)\%$	14%	5.3%
IV_ϕ	$(28.7 \pm 0.4)\%$	$(72.6 \pm 0.4)\%$	21%	61%

Table 7.3: Fraction of events and fraction of covered volume for category I_ϕ ($\hat{\tau}_{lr} = +2$), II_ϕ ($0 < \hat{\tau}_{lr} < +2$), IIIa_ϕ ($-2 < \hat{\tau}_{lr} \leq 0$ and $\tau_l = -1$), IIIb_ϕ ($-2 < \hat{\tau}_{lr} \leq 0$ and $\tau_r = -1$), and IV_ϕ ($\hat{\tau}_{lr} = -2$) for simulation and data.

various causes:

- The extension of the volume in which hits are generated might be underestimated in the simulation. This would affect especially the transition and the boundary zone.

- Differences exist in the selection of events with an energy deposition in only one segment. In the data, this happens after the drift of the charge carriers, resulting in effective segment boundaries. In the simulation, the selection is done before the drift of the charge carriers is simulated. The geometrical segment boundaries are thus applied. The largest effect from these differences is expected for the boundary region.

- Only one electron-hole pair is simulated for every selected event. In reality, many electron-hole pairs are created and the drifting charges would be better described as a set of trajectories filling a volume with a diameter of $\mathcal{O}(\mathrm{mm})$. Also the influence of the crystal axes is different for a cloud. The individual charge carriers in the cloud are influenced differently, depending on their relative position to the crystal axes, and thus the volume of the cluster can change. This affects the amplitudes in all zones, but has the largest effects in the transition and boundary zones.

- In the simulation, ρ_{imp} is assumed to be homogeneous throughout the detector. This might not be the case in reality. According to the manufacturer, $\rho_{\mathrm{imp,top}} > \rho_{\mathrm{imp,bottom}}$ for SIII. This affects especially the boundary zones in z. In addition, there is a relatively large uncertainty on the absolute value of ρ_{imp}. A different value could move the location of the transition zone.

- The simulated drift velocities might be incorrect either because of an unrealistic ρ_{imp} distribution or because of incorrect electron and hole mobilities. In the first case, the drift velocities of the electrons as well as of the holes would be altered. In the second case, the velocities of electrons and holes could vary independently. In both cases, specific changes in the behavior in the transition and boundary zones would occur. In addition, the zones could move.

The origin of the discrepancies between data and simulation is certainly a combination of several of these reasons. However, it looks as if the position reconstruction works quite well for events relatively close to the core or the mantle.

Chapter 8

Conclusion and outlook

Segmented HPGe detectors are developed for a variety of applications. One goal is to reduce the background level in experiments like GERDA, searching for $0\nu\beta\beta$ decay. The reduction of background due to environmental radioactivity is crucial for the success of such experiments. Position reconstruction serves as a tool to identify background sources.

In this thesis, a method was presented to reconstruct the position of single energy depositions using mirror pulses. Mirror pulses are a phenomenon intrinsic to segmented detectors. Their shape and amplitude is highly dependent on the position of the energy deposition. Mirror pulses simulated with a pulse shape simulation package were used to find parameters that quantify this dependence for single energy depositions. A method was developed to reconstruct the position in ϕ and z for simulated events. The resolution achieved was $\mathcal{O}$(mm) in the ϕ- as well as in the z-direction.

Data was recorded in order to verify the mirror pulse simulation and to test the method to reconstruct the position on data. Events in the DEP of ^{208}Tl were identified as an appropriate data sample. Data from a ^{228}Th source was recorded using the 18–fold segmented n-type HPGe detector Siegfried III. To characterize the detector, pulses from the 344 keV line of ^{152}Eu were also recorded. They were used to determine the position of the segment boundaries and crystal axes needed as input to the simulation.

The GEANT4 based simulation package MaGe was used to simulate the interactions of the relevant photons from peaks of a ^{228}Th source in the detector. Pulse shapes were simulated for single-segment events that were attributed to the DEP.

The characteristics of the mirror pulses, such as amplitude, polarity, and the parameters quantifying the position dependence were determined for each simulated as well as measured event. The position in ϕ and z was reconstructed.

The simulation describes the data reasonably well for the volumes close to the core and close to the mantle. In these regions, the main characteristics of the mirror pulses are well reproduced by the simulation. The distribution of the reconstructed positions in the data is also predicted reasonably well. This is true in spite of the fact that the volume boundaries do not agree between simulation and data. The volume classified as close to the core by the polarity of the mirror pulses is too small in the simulation.

The transition region between inner and outer volume is consequently also located too close to the core in the simulation. The parameters determined from the simulation to reconstruct positions cannot be used safely for the data.

The region close to the segment boundaries is also not well described by the simulation. In this case, the details neglected so far in the simulation seem to be important.

The classification of events developed from the simulation holds for the data. Therefore, the measured events can be categorized and the volume they belong to can be identified. Events in the "safe" volumes can be reconstructed, accounting for the majority of the events.

Several limitations of the simulation are known: $\mathcal{O}(10)$ hits describe a cloud of $\mathcal{O}(500\,000)$ charge carrier pairs, the effective segment boundaries are disregarded when DEP events are selected, the finite size of the charge carrier cloud is neglected, and uncertainties in the active impurity density and in the drift velocities of the charge carriers are ignored.

Future studies should investigate whether the currently used settings for MaGe produce a detailed enough hit list to describe the localization of an event. They should make selection cuts that take the influence of the transversal anisotropy on the drift of the charge cloud into account and they should simulate the mirror pulses for the set of charges composing the cloud instead for the single pair of charge carriers at the barycenter of the energy deposition. In addition, the influence of the distribution of impurities and of electron and hole mobilities should be studied. Impurities change the velocities of both types of charge carriers, while the simulated mobilities could be off quite differently for electrons and holes. A careful analysis of simulated as well as measured mirror pulses after taking into account the effective segment boundaries and the charge cloud might therefore provide insight regarding the distribution of the impurity density in the detector and the electron and hole mobilities.

Appendix A

Correlation between ϕ and α_{lr}

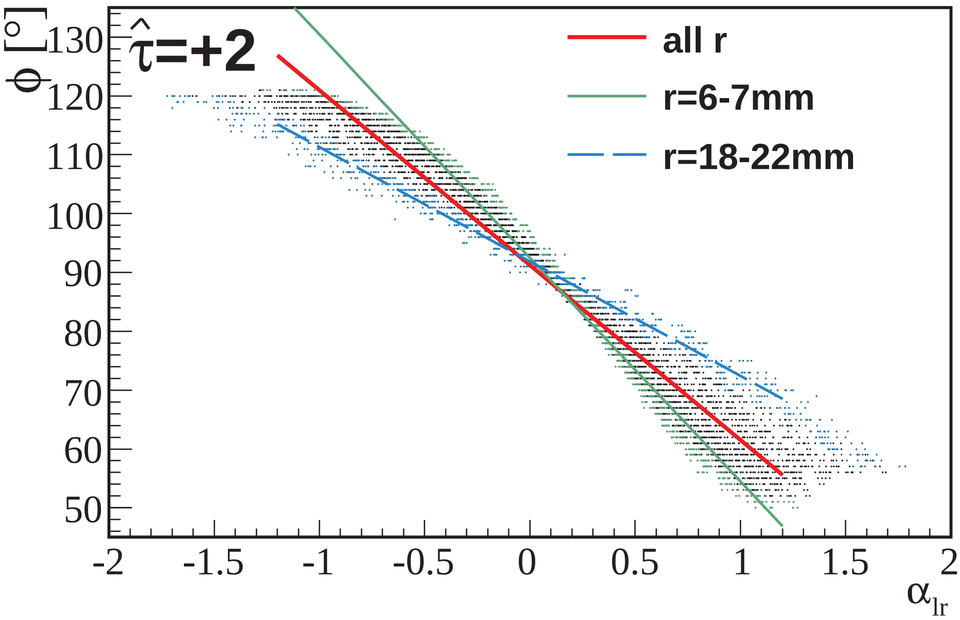

(a)

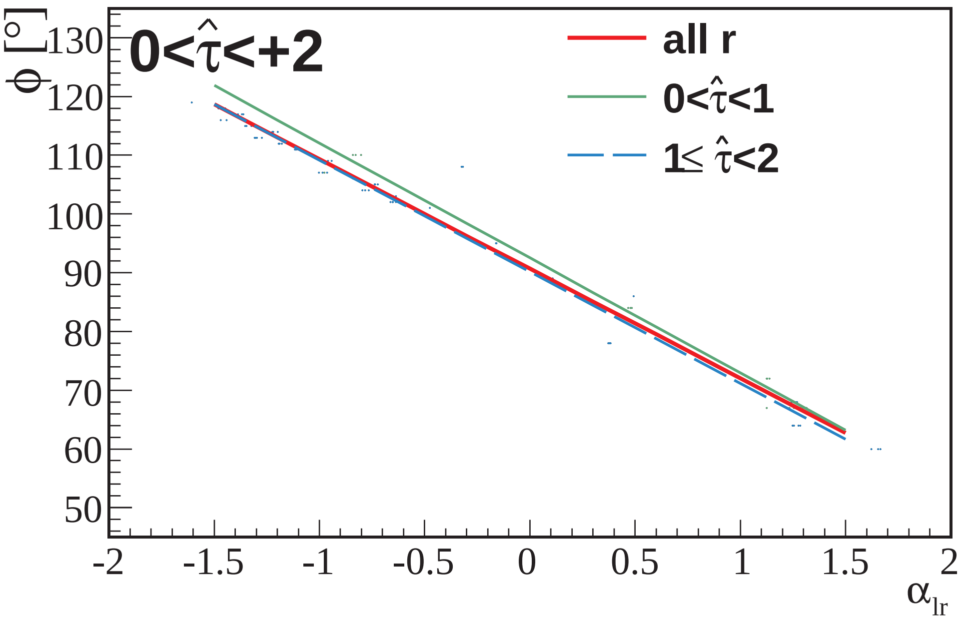

(b)

Figure A.1: Correlation between ϕ and α_{lr} for events in category (a) I_ϕ ($\hat{\tau}_{lr} = +2$) and (b) II_ϕ ($0 < \hat{\tau}_{lr} < +2$). Each symbol represents one event. Events were simulated at $z = 0$ mm, 6 mm, 10 mm, 14 mm, 20 mm, 26 mm, and 32 mm and selected to fall into segments 3 or 6. Also shown are linear fits to (a) the whole distribution and to events with $r = 6 - 7$ mm and with $r = 18 - 22$ mm separately (b) the whole distribution and to events with $0 < \hat{\tau}_{lr} < 1$ and with $1 \leq \hat{\tau}_{lr} < 2$ separately. The fit results are listed in Tables 4.2 and 4.3.

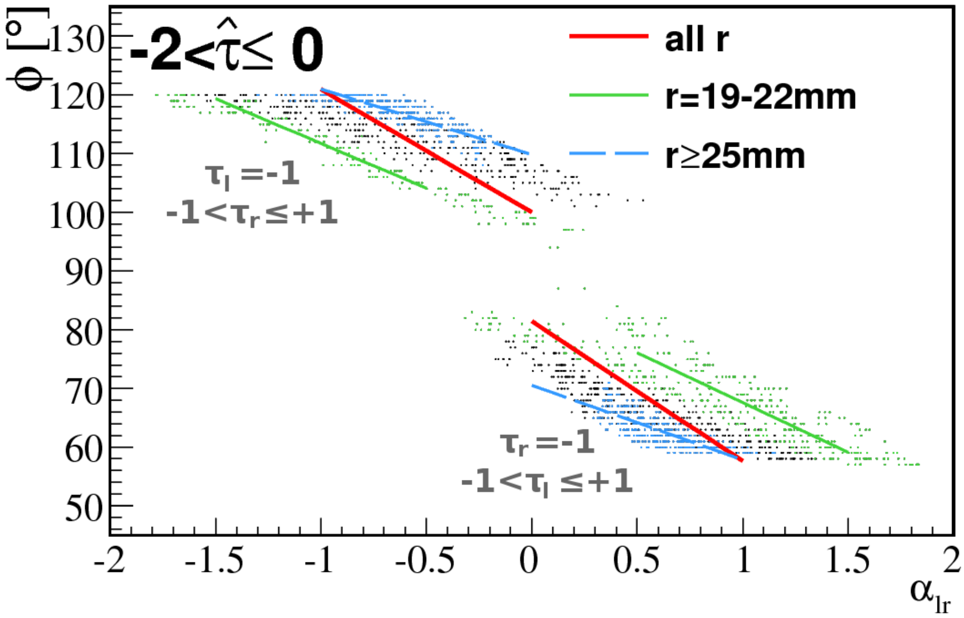

(a)

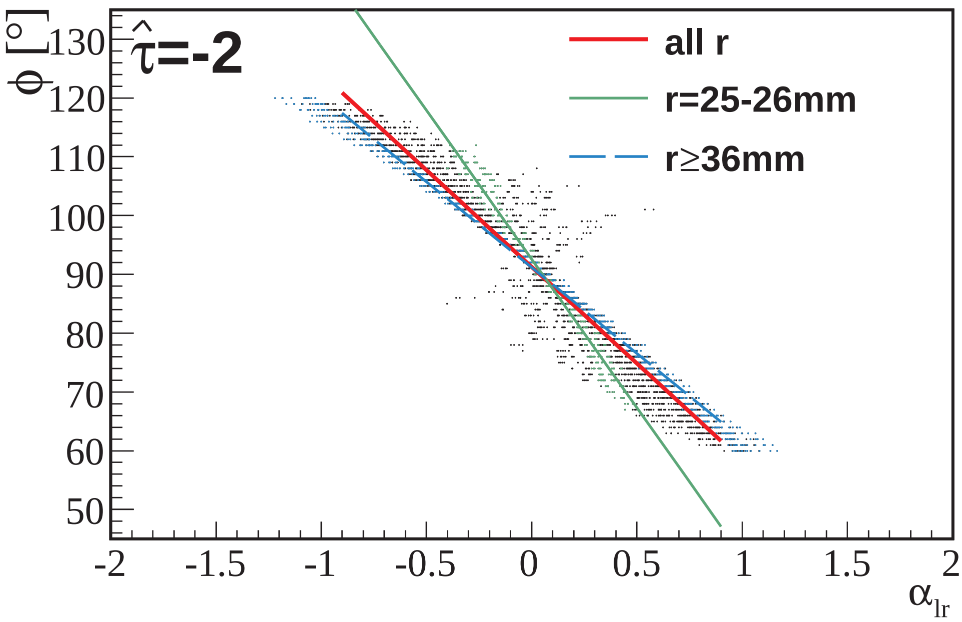

(b)

Figure A.2: Correlation between ϕ and α_{lr} for events in category (a) IIIa$_\phi$ and IIIb$_\phi$ ($-2 < \hat{\tau}_{lr} \leq 0$), and (b) IV$_\phi$ ($\hat{\tau}_{lr} = -2$). Each symbol represents one event. Events were simulated at $z = 0$ mm, 6 mm, 10 mm, 14 mm, 20 mm, 26 mm, and 32 mm and selected to fall into segments 3 or 6. Also shown are linear fits to (a) the whole distribution and to events with $r = 19 - 22$ mm and with $r \geq 25$ mm separately (b) the whole distribution and to events with $r = 25 - 26$ mm and with $r \geq 36$ mm separately. The fit results are listed in Tables 4.2 and 4.3.

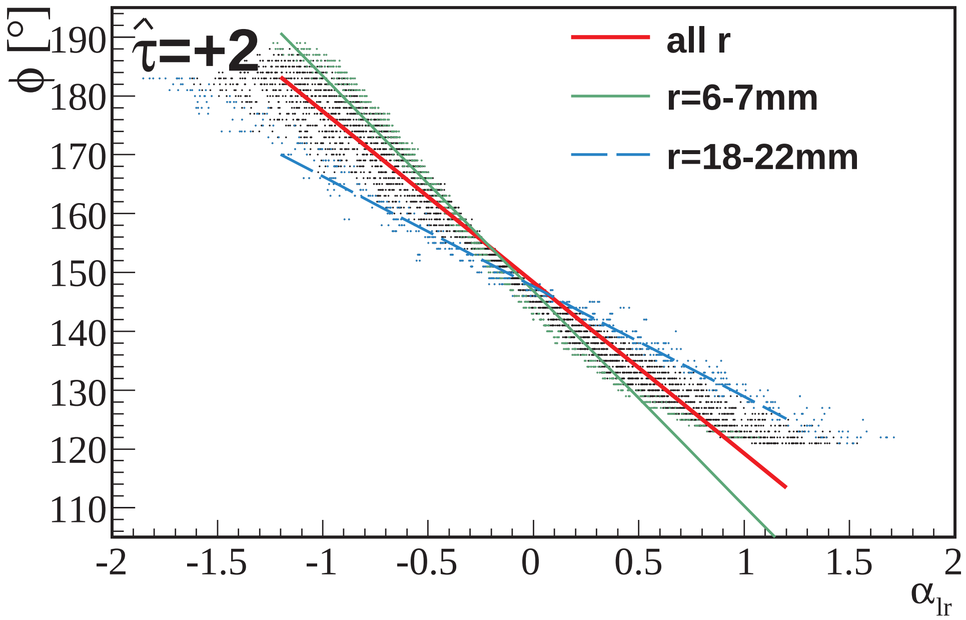

(a)

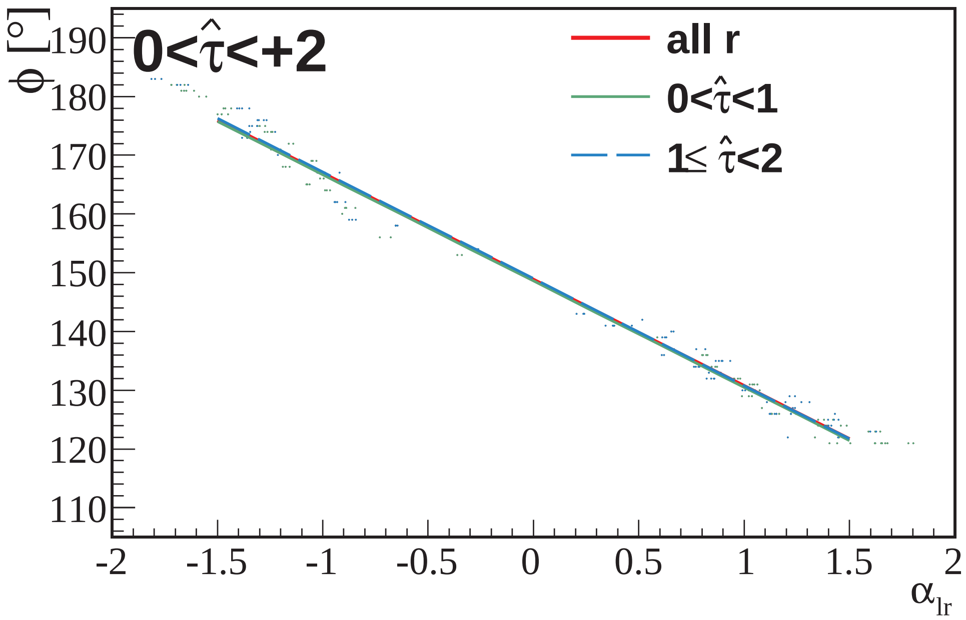

(b)

Figure A.3: Correlation between ϕ and α_{lr} for events in category (a) I_ϕ ($\hat{\tau}_{lr} = +2$) and (b) II_ϕ ($0 < \hat{\tau}_{lr} < +2$). Each symbol represents one event. Events were simulated at $z = 0$ mm, 6 mm, 10 mm, 14 mm, 20 mm, 26 mm, and 32 mm and selected to fall into segments 16 or 13. Also shown are linear fits to (a) the whole distribution and to events with $r = 6 - 7$ mm and with $r = 18 - 22$ mm separately (b) the whole distribution and to events with $0 < \hat{\tau}_{lr} < 1$ and with $1 \leq \hat{\tau}_{lr} < 2$ separately. The fit results are listed in Tables 4.2 and 4.3.

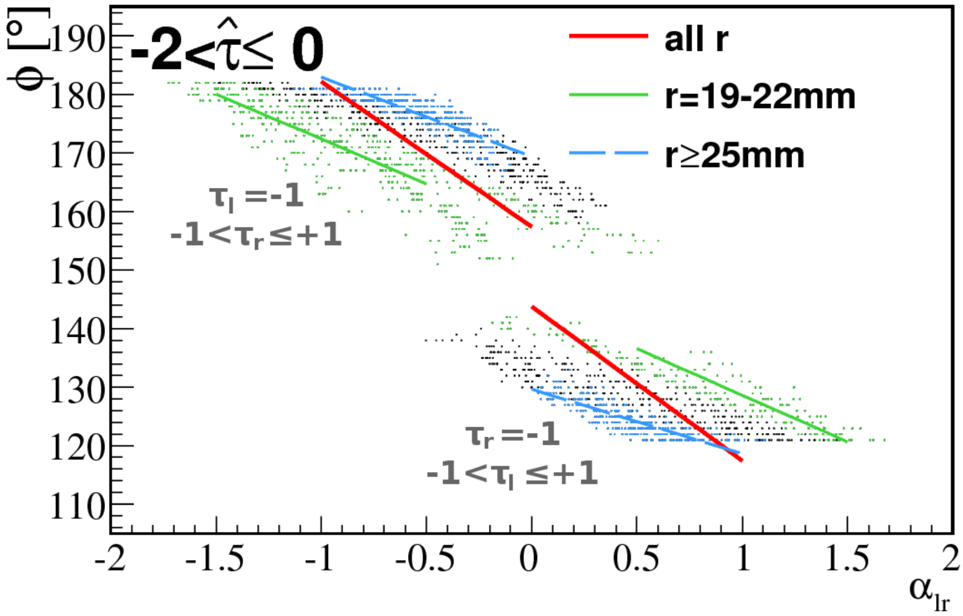

(a)

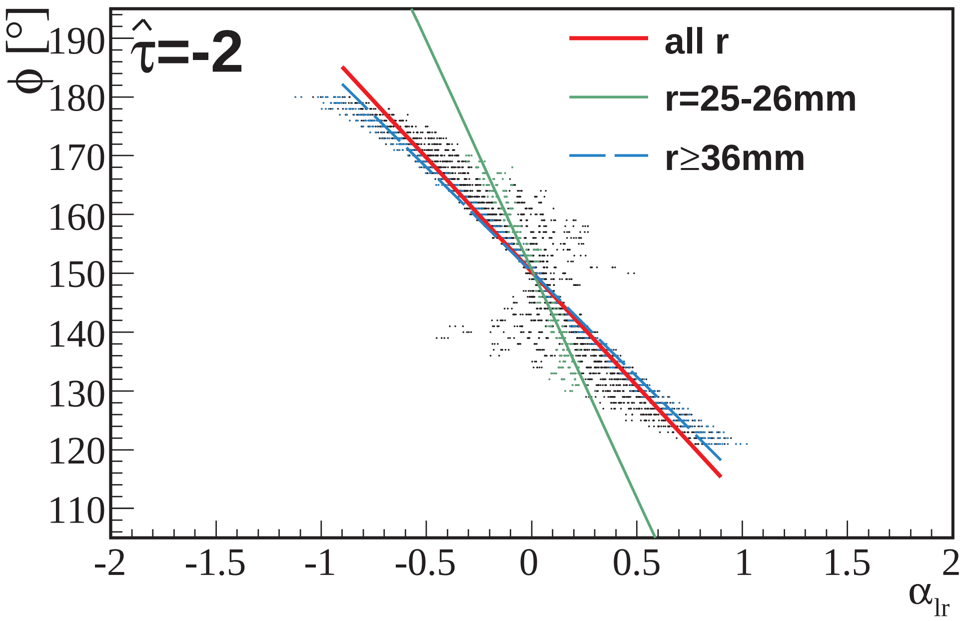

(b)

Figure A.4: Correlation between ϕ and α_{lr} for events in category (a) IIIa$_\phi$ and IIIb$_\phi$ ($-2 < \hat{\tau}_{lr} \leq 0$), and (b) IV$_\phi$ ($\hat{\tau}_{lr} = -2$). Each symbol represents one event. Events were simulated at $z = 0$ mm, 6 mm, 10 mm, 14 mm, 20 mm, 26 mm, and 32 mm and selected to fall into segments 16 or 13. Also shown are linear fits to (a) the whole distribution and to events with $r = 19 - 22$ mm and with $r \geq 25$ mm separately (b) the whole distribution and to events with $r = 25 - 26$ mm and with $r \geq 36$ mm separately. The fit results are listed in Tables 4.2 and 4.3.

Appendix B

Resolutions and peak-to-background ratios at $E = 1593\,\mathrm{keV}$

segment	$p\,(1\sigma)$	$p/b\,(1\sigma)$	FWHM [keV]
core	31289 ± 177	3.1 ± 0.1	5.4 ± 0.1
1	1099 ± 33	2.9 ± 0.2	4.7 ± 0.2
2	2074 ± 46	4.2 ± 0.2	4.3 ± 0.1
3	2989 ± 55	4.5 ± 0.2	4.3 ± 0.1
4	805 ± 28	2.5 ± 0.2	4.4 ± 0.2
5	1512 ± 39	3.3 ± 0.2	4.5 ± 0.1
6	2150 ± 46	3.8 ± 0.2	4.5 ± 0.1
7	1936 ± 44	4.3 ± 0.2	4.3 ± 0.1
8	2674 ± 52	5.0 ± 0.2	4.4 ± 0.1
9	3578 ± 60	5.7 ± 0.2	4.3 ± 0.1
10	3285 ± 57	4.9 ± 0.2	4.4 ± 0.1
11	1734 ± 42	3.6 ± 0.2	4.4 ± 0.1
12	1443 ± 38	3.2 ± 0.1	4.3 ± 0.1
13	1803 ± 42	2.8 ± 0.1	4.9 ± 0.1
14	1030 ± 32	2.2 ± 0.1	5.3 ± 0.2
15	658 ± 26	2.1 ± 0.1	4.3 ± 0.2
16	–	–	–
17	1302 ± 36	2.9 ± 0.2	4.8 ± 0.2
18	944 ± 31	2.7 ± 0.2	4.5 ± 0.2

Table B.1: Results from fitting $S(E)$ to the 1593 keV peak of $\mathrm{Th}_{\mathrm{data}}$. The uncertainties listed are statistical only.

Appendix C

Resolutions and peak-to-background ratios at $E = 344\,\mathrm{keV}$

ϕ [°]	t_{life} [s]	p/t_{life} [1/s]	$p/b\,(1\sigma)$	FWHM [keV]
168	2454	0.51 ± 0.01	2.5 ± 0.1	4.3 ± 0.2
170	2495	0.47 ± 0.01	2.4 ± 0.1	4.3 ± 0.1
172	2516	0.43 ± 0.01	2.2 ± 0.1	4.2 ± 0.2
174	2532	0.39 ± 0.01	2.0 ± 0.1	4.3 ± 0.2
176	2514	0.36 ± 0.01	1.9 ± 0.1	4.5 ± 0.2
178	2466	0.29 ± 0.01	1.5 ± 0.1	4.4 ± 0.2
180	2443	0.20 ± 0.01	1.1 ± 0.1	4.3 ± 0.3
182	2441	0.11 ± 0.01	0.6 ± 0.1	4.3 ± 0.5
184	2456	0.05 ± 0.01	0.3 ± 0.1	3.6 ± 0.7
186	2462	0.02 ± 0.01	0.2 ± 0.1	2.4 ± 0.8
188	2467	no peak		
190	2470	no peak		
192	2477	no peak		
194	2481	no peak		
196	2483	no peak		
198	2488	no peak		
200	2476	no peak		
202	2469	no peak		
204	2476	no peak		
206	2486	no peak		
208	2495	no peak		
210	2504	no peak		
212	2537	no peak		
214	2545	no peak		
216	2557	no peak		
218	2560	no peak		
220	2571	no peak		
222	2581	no peak		
224	2587	no peak		
226	2598	no peak		
228	2607	no peak		
230	2613	no peak		
232	2623	no peak		
234	2620	no peak		
236	2630	no peak		
238	2633	no peak		
240	2639	no peak		
242	2655	no peak		
244	2664	no peak		

Table C.1: Results from fitting $S(E)$ to the 344 keV peak of Eu344$_{13}$. A normalization to the lifetime was applied to p. The uncertainties listed are statistical only.

ϕ [°]	t_{life} [s]	p/t_{life} [1/s]	$p/b\,(1\sigma)$	FWHM [keV]
168	2454	no peak		
170	2495	no peak		
172	2516	no peak		
174	2532	0.04 ± 0.01	0.3 ± 0.1	3.8 ± 0.8
176	2514	0.04 ± 0.01	0.5 ± 0.1	2.7 ± 0.7
178	2466	0.11 ± 0.01	0.7 ± 0.1	4.3 ± 0.6
180	2443	0.19 ± 0.01	1.3 ± 0.1	3.6 ± 0.3
182	2441	0.29 ± 0.01	2.0 ± 0.1	3.6 ± 0.2
184	2456	0.38 ± 0.01	2.7 ± 0.2	3.6 ± 0.1
186	2462	0.42 ± 0.01	2.6 ± 0.2	3.8 ± 0.1
188	2467	0.50 ± 0.01	3.2 ± 0.2	3.6 ± 0.1
190	2470	0.54 ± 0.01	3.4 ± 0.2	3.6 ± 0.1
192	2477	0.54 ± 0.01	3.5 ± 0.2	3.5 ± 0.1
194	2481	0.53 ± 0.01	3.3 ± 0.2	3.6 ± 0.1
196	2483	0.52 ± 0.01	3.3 ± 0.2	3.6 ± 0.1
198	2488	0.59 ± 0.02	3.7 ± 0.2	3.5 ± 0.1
200	2476	0.56 ± 0.02	3.3 ± 0.2	3.7 ± 0.1
202	2469	0.56 ± 0.02	3.4 ± 0.2	3.4 ± 0.1
204	2476	0.55 ± 0.01	3.2 ± 0.2	3.6 ± 0.1
206	2486	0.55 ± 0.01	3.3 ± 0.2	3.5 ± 0.1
208	2495	0.50 ± 0.01	3.2 ± 0.2	3.4 ± 0.1
210	2504	0.49 ± 0.01	3.0 ± 0.2	3.6 ± 0.1
212	2537	0.57 ± 0.01	3.7 ± 0.2	3.4 ± 0.1
214	2545	0.48 ± 0.01	2.7 ± 0.2	4.0 ± 0.1
216	2557	0.48 ± 0.01	2.8 ± 0.2	3.8 ± 0.1
218	2560	0.48 ± 0.01	2.8 ± 0.2	4.1 ± 0.1
220	2571	0.44 ± 0.01	2.5 ± 0.1	3.9 ± 0.1
222	2581	0.40 ± 0.01	2.3 ± 0.1	3.9 ± 0.2
224	2587	0.40 ± 0.01	2.4 ± 0.1	3.8 ± 0.1
226	2598	0.35 ± 0.01	2.3 ± 0.1	3.6 ± 0.2
228	2607	0.32 ± 0.01	2.1 ± 0.1	3.7 ± 0.2
230	2613	0.24 ± 0.01	1.5 ± 0.1	3.9 ± 0.2
232	2623	0.19 ± 0.01	1.2 ± 0.1	4.0 ± 0.3
234	2620	0.16 ± 0.01	1.1 ± 0.1	3.6 ± 0.3
236	2630	0.14 ± 0.01	1.0 ± 0.1	3.7 ± 0.3
238	2633	0.05 ± 0.01	0.4 ± 0.1	3.8 ± 0.7
240	2639	no peak		
242	2655	no peak		
244	2664	no peak		

Table C.2: Results from fitting $S(E)$ to the 344 keV peak of Eu344_{14}. A normalization to the lifetime was applied to p. The uncertainties listed are statistical only.

ϕ [°]	t_{life} [s]	p/t_{life} [1/s]	$p/b\,(1\sigma)$	FWHM [keV]
168	2454	no peak		
170	2495	no peak		
172	2516	no peak		
174	2532	no peak		
176	2514	no peak		
178	2466	no peak		
180	2443	no peak		
182	2441	no peak		
184	2456	no peak		
186	2462	no peak		
188	2467	no peak		
190	2470	no peak		
192	2477	no peak		
194	2481	no peak		
196	2483	no peak		
198	2488	no peak		
200	2476	no peak		
202	2469	no peak		
204	2476	no peak		
206	2486	no peak		
208	2495	no peak		
210	2504	no peak		
212	2537	no peak		
214	2545	no peak		
216	2557	no peak		
218	2560	0.04 ± 0.01	0.4 ± 0.1	3.9 ± 0.9
220	2571	0.05 ± 0.01	0.4 ± 0.1	3.9 ± 0.8
222	2581	0.03 ± 0.01	0.3 ± 0.1	3.2 ± 0.8
224	2587	0.07 ± 0.01	0.6 ± 0.1	3.9 ± 0.5
226	2598	0.08 ± 0.01	0.7 ± 0.1	3.5 ± 0.4
228	2607	0.11 ± 0.01	0.7 ± 0.1	4.5 ± 0.5
230	2613	0.13 ± 0.01	0.9 ± 0.1	4.2 ± 0.4
232	2623	0.20 ± 0.01	1.4 ± 0.1	3.7 ± 0.3
234	2620	0.16 ± 0.01	1.2 ± 0.1	3.2 ± 0.3
236	2630	0.20 ± 0.01	1.3 ± 0.1	3.9 ± 0.2
238	2633	0.36 ± 0.01	2.4 ± 0.1	3.6 ± 0.1
240	2639	0.52 ± 0.01	3.4 ± 0.2	3.6 ± 0.1
242	2655	0.53 ± 0.01	3.1 ± 0.2	3.9 ± 0.1
244	2664	0.50 ± 0.01	3.0 ± 0.2	3.8 ± 0.1

Table C.3: Results from fitting $S(E)$ to the 344 keV peak of $\mathrm{Eu344}_{15}$. A normalization to the lifetime was applied to p. The uncertainties listed are statistical only.

z [mm]	t_{life} [s]	p/t_{life} [1/s]	$p/b\,(1\sigma)$	FWHM [keV]
-16	2552	0.40 ± 0.01	2.1 ± 0.1	3.5 ± 0.1
-14	2547	0.28 ± 0.01	1.5 ± 0.1	3.6 ± 0.2
-12	2534	0.05 ± 0.01	0.3 ± 0.1	3.5 ± 0.8
-10	2535	no peak		
-8	2527	no peak		
-6	2523	no peak		
-4	2511	no peak		
-2	2507	no peak		
0	2469	no peak		
2	2494	no peak		
4	2481	no peak		
6	2477	0.07 ± 0.01	0.2 ± 0.1	5.0 ± 1.3
8	2472	0.10 ± 0.01	0.3 ± 0.1	4.3 ± 0.6
10	2469	0.10 ± 0.01	0.4 ± 0.1	3.2 ± 0.5
12	2462	0.11 ± 0.01	0.5 ± 0.1	3.2 ± 0.4
14	2454	0.14 ± 0.01	0.6 ± 0.1	3.6 ± 0.5
16	2448	0.18 ± 0.01	0.7 ± 0.1	3.6 ± 0.3

Table C.4: Results from fitting $S(E)$ to the 344 keV peak of Eu344$_{11}$. A normalization to the lifetime was applied to p. The uncertainties listed are statistical only.

z [mm]	t_{life} [s]	p/t_{life} [1/s]	$p/b\,(1\sigma)$	FWHM [keV]
-16	2552	no peak		
-14	2547	0.04 ± 0.01	0.2 ± 0.1	4.0 ± 1.2
-12	2534	0.25 ± 0.01	1.4 ± 0.1	3.6 ± 0.2
-10	2535	0.42 ± 0.01	2.3 ± 0.1	3.9 ± 0.2
-8	2527	0.48 ± 0.01	2.5 ± 0.1	4.0 ± 0.1
-6	2523	0.51 ± 0.01	2.8 ± 0.2	3.7 ± 0.1
-4	2511	0.55 ± 0.01	3.1 ± 0.2	3.7 ± 0.1
-2	2507	0.49 ± 0.01	2.7 ± 0.1	3.7 ± 0.1
0	2469	0.50 ± 0.01	3.0 ± 0.2	3.6 ± 0.1
2	2494	0.48 ± 0.01	2.6 ± 0.1	4.2 ± 0.1
4	2481	0.49 ± 0.01	2.7 ± 0.2	4.1 ± 0.1
6	2477	0.48 ± 0.01	2.7 ± 0.1	4.1 ± 0.1
8	2472	0.47 ± 0.01	2.6 ± 0.1	3.9 ± 0.1
10	2469	0.35 ± 0.01	2.1 ± 0.1	3.8 ± 0.2
12	2462	0.15 ± 0.01	0.8 ± 0.1	4.1 ± 0.3
14	2454	no peak		
16	2448	no peak		

Table C.5: Results from fitting $S(E)$ to the 344 keV peak of Eu344$_{14}$. A normalization to the lifetime was applied to p. The uncertainties listed are statistical only.

z [mm]	t_{life} [s]	p/t_{life} [1/s]	$p/b\,(1\sigma)$	FWHM [keV]
-16	2552	0.09 ± 0.01	0.3 ± 0.02	5.8 ± 0.9
-14	2547	0.07 ± 0.01	0.3 ± 0.02	4.8 ± 1.6
-12	2534	0.07 ± 0.01	0.2 ± 0.02	5.6 ± 2.8
-10	2535	no peak		
-8	2527	no peak		
-6	2523	no peak		
-4	2511	no peak		
-2	2507	no peak		
0	2469	no peak		
2	2494	no peak		
4	2481	no peak		
6	2477	no peak		
8	2472	no peak		
10	2469	no peak		
12	2462	0.12 ± 0.01	0.5 ± 0.1	3.9 ± 0.5
14	2454	0.40 ± 0.01	1.8 ± 0.1	3.9 ± 0.2
16	2448	0.42 ± 0.01	1.8 ± 0.1	4.4 ± 0.2

Table C.6: Results from fitting $S(E)$ to the 344 keV peak of $\mathrm{Eu344}_{17}$. A normalization to the lifetime was applied to p. The uncertainties listed are statistical only.

Appendix D

Resolutions and peak-to-background ratios for Monte Carlo generated events at $E = 1593\,\mathrm{keV}$

segment	$p\,(1\sigma)$	$p/b\,(1\sigma)$	FWHM [keV]
core	87396 ± 296	5.4 ± 0.1	4.5 ± 0.1
1	3088 ± 56	5.0 ± 0.2	4.4 ± 0.1
2	6471 ± 80	5.7 ± 0.2	4.3 ± 0.1
3	7140 ± 84	5.9 ± 0.2	4.4 ± 0.1
4	1999 ± 45	3.8 ± 0.2	4.2 ± 0.1
5	4396 ± 66	4.8 ± 0.2	4.5 ± 0.1
6	4748 ± 69	5.3 ± 0.2	4.4 ± 0.1
7	5685 ± 75	5.7 ± 0.2	4.4 ± 0.1
8	8544 ± 92	6.7 ± 0.2	4.4 ± 0.1
9	9311 ± 96	7.7 ± 0.2	4.4 ± 0.1
10	8449 ± 92	6.7 ± 0.2	4.4 ± 0.1
11	5019 ± 71	5.2 ± 0.2	4.4 ± 0.1
12	3444 ± 59	4.4 ± 0.2	4.4 ± 0.1
13	4373 ± 66	4.8 ± 0.2	4.4 ± 0.1
14	2111 ± 46	3.9 ± 0.2	4.4 ± 0.1
15	1271 ± 36	3.4 ± 0.2	4.3 ± 0.1
16	6528 ± 81	5.7 ± 0.2	4.4 ± 0.1
17	3154 ± 56	5.0 ± 0.2	4.5 ± 0.1
18	1851 ± 43	4.8 ± 0.3	4.3 ± 0.1

Table D.1: Results from fitting $S(E)$ to the $1593\,\mathrm{keV}$ peak of $\mathrm{Th}_{\mathrm{simu}}$. The uncertainties listed are statistical only.

Bibliography

[1] J. Eberth and J. Simpson, *From Ge(Li) detectors to gamma-ray tracking arrays - 50 years of gamma spectroscopy with germanium detectors*, Prog. Part. & Nucl. Phys. **60** (2008), 283 – 337.

[2] I. Abt et al., *A new ^{76}Ge double beta decay experiment at LNGS*, arXiv:hep-ex/0404039 (2004).

[3] K. Zuber, *Neutrino Physics*, 1st ed., IOP, 2004.

[4] U. Dore and D. Orestano, *Experimental results on neutrino oscillations*, Rep. Prog. Phys. **71** (2008), 106201.

[5] M. Steidl, *Experiments for the absolute neutrino mass measurement*, arXiv:nucl-ex/09060454 (2009).

[6] C. Kraus et al., *Final results from phase II of the Mainz neutrino mass search in tritium beta decay*, Eur. Phys. J. C **40** (2005), 447 – 468.

[7] V. Lobashev, *The search for the neutrino mass by direct method in the tritium beta-decay and perspectives of study it in the project KATRIN*, Nucl. Phys. A **719** (2003), 153–160.

[8] J. Schechter and J. Valle, *Neutrinoless double-β decay in SU(2)$\times$U(1) theories*, Phys. Rev. D **25** (1982), 2951–2954.

[9] C. Arnaboldi et al., *Results from a search for the $0\nu\beta\beta$-decay of ^{130}Te*, Phys. Rev. C **78** (2008), 035502.

[10] C. E. Aalseth et al., *IGEX ^{76}Ge neutrinoless double-beta decay experiment: Prospects for next generation experiments*, Phys. Rev. D **65** (2002), 092007.

[11] H. V. Klapdor-Kleingrothaus et al., *Latest results from the HEIDELBERG-MOSCOW double beta decay experiment*, Eur. Phys. J. A **12** (2001), 147–154.

[12] ______, *Search for neutrinoless double beta decay with enriched ^{76}Ge in Gran Sasso 1990-2003*, Phys. Lett. B **586** (2004), 198 – 212.

[13] F. Petry et al., *Background recognition in Ge detectors by pulse shape analysis*, Nucl. Instr. Meth. A **332** (1993), 107 – 112.

[14] I. Abt et al., *Test of pulse shape analysis using single Compton scattering events*, Eur. Phys. J. C **54** (2008), 425 – 433.

[15] ______, *Pulse shapes from electron and photon induced events in segmented high-purity germanium detectors*, Eur. Phys. J. C **52** (2007), 19 – 27.

[16] ______, *Background reduction in neutrinoless double beta decay experiments using segmented detectors – A Monte Carlo study for the GERDA setup*, Nucl. Instr. Meth. A **570** (2007), 479 – 486.

[17] ______, *Identification of photons in double beta decay experiments using segmented germanium detectors – studies with a GERDA Phase II prototype detector*, Nucl. Instr. Meth. A **583** (2007), 332 – 340.

[18] ______, *Neutron interactions as seen by a segmented germanium detector*, Eur. Phys. J. A **36** (2008), 139 – 149.

[19] ______, *Characterization of the first true coaxial 18-fold segmented n-type prototype HPGe detector for the GERDA project*, Nucl. Instr. Meth. A **577** (2007), 574 – 584.

[20] ______, *Pulse shape simulation for segmented true-coaxial HPGe detectors*, Eur. Phys. J. C **68** (2010), 609–618.

[21] G. F. Knoll, *Radiation Detection and Measurement*, 3rd ed., John Wiley & Sons,Inc., 2000.

[22] M. J. Berger et al., *XCOM: Photon Cross Section Database (version 1.4). http://physics.nist.gov/xcom*, National Institute of Standards and Techonology, Gaithersburg, MD (2009).

[23] C. Grupen and B. Shwartz, *Particle Detectors*, 2nd ed., Cambridge University Press, 2008.

[24] K. Kleinknecht, *Detektoren für Teilchenstrahlung*, 4th ed., Teubner, 2005.

[25] T. Mukoyama, *Range of electrons and positrons*, Nucl. Instr. Meth. A **134** (1976), 125 – 127.

[26] I. Abt et al., *Operation of an 18-fold segmented n-type HPGe detector in liquid nitrogen*, J. Instrum. **4** (2009), P11008.

[27] J. Gerl and W. Korten (eds.), *Technical Proposal for the AGATA project*, 2001.

[28] M. A. Deleplanque et al., *GRETA: utilizing new concepts in γ-ray detection*, Nucl. Instr. Meth. A **430** (1999), 292 – 310.

[29] Z. He, *Review of the Shockley-Ramo theorem and its application in semiconductor gamma-ray detectors*, Nucl. Instr. Meth. A **463** (2001), 250 – 267.

[30] S. Agostinelli et al., *GEANT4: A simulation toolkit*, Nucl. Instr. Meth. A **506** (2003), 250 – 303.

[31] M. Bauer et al., *MaGe: a Monte Carlo framework for the Gerda and Majorana double beta decay experiments*, J. Phys.: Conf. Ser **39** (2006), 362.

[32] D. Lenz, *Pulse Shapes and Surface Effects in Segmented Germanium Detectors*, Ph.D. thesis, Technische Universität München, 2010.

[33] W. Sasaki et al., *Anisotropy of hot electrons in germanium*, J. Phys. Chem. Sol. **8** (1959), 250 – 256.

[34] H. G. Reik and H. Risken, *Drift Velocity and Anisotropy of Hot Electrons in n Germanium*, Phys. Rev. **126** (1962), 1737–1746.

[35] J. Liu, *Development of Segmented Germanium Detectors for Neutrinoless Double Beta Decay Experiments*, Ph.D. thesis, Technische Universität München, 2009.

[36] J. J. Valiente-Dobón et al., *Performance of a 6×6 segmented germanium detector for γ-ray tracking*, Nucl. Instr. Meth. A **505** (2003), 174 – 177.

[37] M. Descovich et al., *The position response of a large-volume segmented germanium detector*, Nucl. Instr. Meth. A **553** (2005), 512 – 521.

[38] A.J. Boston et al., *Gamma-ray tracking: Characterisation of the AGATA symmetric prototype detectors*, Nucl. Instr. Meth. B **261** (2007), 1098 – 1102.

[39] K. Vetter et al., *Three-dimensional position sensitivity in two-dimensionally segmented HP-Ge detectors*, Nucl. Instr. Meth. A **452** (2000), 223 – 238.

[40] X Ray Instrumentation Associates, *Digital Gamma Finder (DGF) PIXIE4, User's manual*.

Danksagung

An dieser Stelle möchte ich mich bei allen Personen bedanken, die mich bei der Erstellung dieser Arbeit unterstützt haben.

Dank gebührt Herrn Prof. Christian Kiesling, dessen Betreuung es mir ermöglichte, meine Arbeit am Max-Planck-Institut für Physik anzufertigen.

Mein besonderer Dank gilt Herrn Dr. Béla Majorovits für die Entwicklung der Themenstellung meiner Diplomarbeit, anregende und inspirierende Gespräche und seine stete Unterstützung sowie Frau Dr. Iris Abt für die inhaltliche Umsetzung, ihren unermüdlichen Einsatz, ihre Geduld und ihr jederzeit offenes Ohr.

Bedanken möchte ich mich auch bei allen Mitgliedern der GeDet- und GERDA-Gruppe für die angenehme Arbeitsatmosphäre und den Beistand über die gesamte Zeit hinweg. Insbesondere danken möchte ich Annika Vauth für ihre unendliche Hilfsbereitschaft, Daniel Lenz, der mir nicht nur bei wissenschaftlichen Fragen mit freundschaftlicher Unterstützung zur Seite stand, Xiang Liu, der mich an seinem Erfahrungsschatz teilhaben ließ, Oleksandr Volynets für seine kompetente Hilfe bei Computerproblemen sowie Fabiana Cossavella und Dan Greenwald für viele konstruktive und motivierende Gespräche auch jenseits der Physik.

Ich möchte mich bei meinem Lehrer Herrn Friedrich bedanken, dessen Unterricht meine Faszination für die Physik weckte.

Sehr dankbar bin ich auch für die Unterstützung von Vroni und Martin, die dafür sorgen, dass ich mich nicht in der Welt der Teilchen verliere.

Mein großer Dank gilt Gianluca, dem es stets gelingt, mich zu motivieren, und der mich wissen lässt, dass er immer an meiner Seite ist.

Unendlicher Dank gebührt meinen Eltern und meinem Bruder für ihre bedingungslose Unterstützung und den Rückhalt, den sie mir in allen Lebenslagen bieten. Ohne sie wäre ich nie so weit gekommen.

Erklärung

Hiermit versichere ich, dass ich die vorliegende Arbeit selbstständig verfasst habe und keine anderen als die angegebenen Quellen und Hilfsmittel benutzt habe.

München, den 17. September 2010

Sabine Hemmer